# FORMATION OF ORIENTED PRECURSORS IN FLOW-INDUCED POLYMER CRYSTALLIZATION: EXPERIMENTAL METHODS AND MODEL MATERIALS

Thesis by

Lucía Fernández-Ballester

In Partial Fulfillment of the Requirements for the

degree of

Doctor of Philosophy

CALIFORNIA INSTITUTE OF TECHNOLOGY

Pasadena, California

2007

(Defended April 20, 2007)

# ACKNOWLEDGEMENTS

I am truly indebted to my advisor Julie Kornfield for her continued support and guidance during my stay in Caltech. Her insight and enthusiasm have been essential throughout these years, and I greatly appreciate the scientific and educational opportunities she encouraged me to take.

I am also grateful to past and present members of my group with whom I have worked closely and that have helped me during my graduate studies. When I started working on flow-induced crystallization, I learned a great deal from Derek Thurman, a senior graduate student, with whom I've spent many hours performing synchrotron experiments and who is always willing to have useful discussions. Diana Smirnova is the graduate student taking on the flow-induced crystallization project, she has provided me with an excellent opportunity to teach, and contributed to my experiments in a valuable and enjoyable way. I am thankful to Shuichi Kimata, a visitor from Sumitomo Co., for useful conversations and assistance, and to Guruswamy Kumaraswamy, who built the instrument I utilized during my studies and was always keen to aid with inquiries. I would also like to thank all members of the Kornfield group for occasional scientific help and for making the lab a supportive and fun environment, including Mike Mackel, Neal Scruggs, Rafael Verduzco, Matt Mattson, Eric Pape, Jim Oberhauser, Maria Lujan Auad, Wei Shen, Mike Kempe, Zuli Kurji, Yan Xia, Ryan Turner, Charles Nickerson, Ameri David, Rob Lammertink, Fred Tessier, Dr. Park and Adam Olsen.

During my work, I have benefited from interacting with exceptional scientists that have provided me with valuable insight and have made many of my experiments possible. I am gratefully indebted to Rajendra Krishnaswamy, Wim Bras, Tim Gough, Francisco Balta-Calleja, Araceli Flores, and Fernando Ania.

I am appreciative to all staff from the X27C beamline at the NSLS and the DUBBLE beamline at ESRF who helped me during my experiments, including Igors Sics, Lixia Rong and Florian Meneau. I also would like to acknowledge Mike Roy, John Van Deusen, and Rodney Rojas at the mechanical shops at Caltech, Tom Dunn at the electrical shop, and

Suresh Gupta for his aid with computer systems. I am indebted to Anne Hormann for precious administrative assistance, but also for providing comfort and helping me maintain a positive attitude.

I acknowledge “la Caixa” for their financial support during my first two graduate at Caltech, and for the opportunity to pursue studies outside Spain and to come to a special place as Caltech.

I am very happy that I got to meet a lot of outstanding people in Caltech, and that I can call many of them my friends. I will greatly miss Paul, Julie, Dan, Anne-Laure, Jernej, and Debrah, and thank them for the fun times we had together during the completion of our doctorates. I am sure we will keep our friendships as we all take our different paths in science.

Caltech is the place where I met my husband Martin, on the very first day. I feel very fortunate that I have had his continued love during all these years. He has always been by my side, during both good and difficult times, and his encouragement has been essential in this process. I also want to thank my family, particularly my parents who have loved me and supported me throughout my life, and have helped me get to where I am today.

I dedicate this thesis to my parents.

# ABSTRACT

This thesis presents new insights into the early events of formation of oriented precursors in flow-induced crystallization of polymers, specifically isotactic polypropylene. Experimental approaches are developed to follow the creation of thread-like precursors during flow. The use of model bimodal polymers provides insight on the role of long chains in the mechanism of formation of oriented precursors. The addition of very long chains ($3.5\times10^6$ g/mol) at low concentration (< 1% wt) dramatically reduced the stress required to trigger formation of thread-like precursors, which opened a wide range of conditions in which to discover how oriented precursors form. The combination of powerful new methods and model materials exposed a kinetic and mechanistic step prior to propagation of oriented precursors that had not been addressed in prior literature. Furthermore, the present model systems provide a bridge to the flow-induced crystallization phenomena that occur in commercial resins, making it very likely that these well-defined polymers will reveal the underlying physics that governs the effects of flow on morphology and final properties of polymers, and providing a rational basis for molecular design of polyolefins to expand the envelope of accessible properties.

The phenomenological effects of flow on polymer crystallization have been known for decades, manifested dramatically in most processing techniques due to the high stresses imposed onto the polymer melt. Processing flows can accelerate the kinetics of crystallization by orders of magnitude, and can induce the formation of highly oriented crystallites that, in turn, impact the final material properties in the solid state. The formation of oriented thread-like precursors is at the heart of these effects of flow on polymer crystallization; however, the fundamental mechanisms underlying their development remain elusive. This lack of understanding frustrates the formulation of a predictive model that relates the polymer molecular characteristics and the imposed processing conditions to the ensuing crystallization kinetics, the final morphology, and hence, the ultimate material properties. Here, we develop experimental approaches that provide insight into the physics of formation of the oriented precursors, which identify the essential elements required in a truly predictive model of flow-induced crystallization.

In this work, we build on experimental capabilities of imposing well-defined flow and thermal histories onto a polymer melt, and of utilizing small quantities of material so that model polymers can be investigated, which allows us to isolate the effect of specific molecular characteristics and flow conditions. Our apparatus provides us with real-time measurements that probe a range of shear stresses throughout a slit flow channel; thus, we develop a "depth sectioning method" as a strategy to isolate the contribution to the real-time signal that arises from a specific level of shear stress. This method is of utmost importance since the formation of thread-like precursors depends strongly on stress. To separate the development of oriented precursors during flow from the growth of oriented crystallites on them, we develop an experimental approach, the "temperature-jump," inspired by classical nucleation studies.

We use a small concentration of ultra-high molecular weight isotactic polypropylene in a matrix of shorter chains to examine the role of long chains in the creation of thread-like precursors. The use of such high molecular weight chains has revealed a richer behavior than could be observed in earlier studies, indicating that there are two stages in thread formation, kick-off and propagation, and that the stress requirement for the first step is more stringent than for the second. The data are consistent with the hypothesis that the interaction of long chains with the tip of a shish creates a local orientation that is not found elsewhere in the flowing melt.

Finally, we combine the two experimental approaches to perform measurements that capture the development of the threads during flow. For intermediate shearing times, our results are well described by the most promising model currently available, the "recoverable strain model," and lay the groundwork for determining the velocity of propagation of threads at different shearing stresses. Also, it suggests that some modifications to the recoverable strain model should be included to correctly capture kick-off and saturation of the formation of threads. The experimental tools described here can be extended to other model materials, for example, to expose the effects of long chain

length > $3.5\times10^6$ g/mol and of the stereo-regularity of the long chains. A larger parameter space can be surveyed in the future to provide additional data to test predictive models that connect molecular characteristics of a resin to structure formation under processing conditions.

# TABLE OF CONTENTS

# LIST OF TABLES

# LIST OF FIGURES

## *Chapter I*

# *Introduction*

## 1.1 Motivation

The effects of flow on polymer crystallization have been known for many years, since these phenomena provide the key to producing strong sheets by film blowing and strong fibers by spinning (PE can reach almost the Young's modulus of steel). On the other hand, highly anisotropic crystallites can also be the source of undesired characteristics such as warping in the final product. Most processing techniques of semicrystalline polymers impose high stresses on the melt, which can accelerate the crystallization kinetics by orders of magnitude and substantially alter the orientation distribution of the crystallites. In spite of decades of research on flow-induced crystallization, the molecular level processes that arise with flow, and the kinetics and anisotropy of nucleation from a distorted melt remain elusive. Due to this lack of fundamental understanding, there is no model yet available that is capable of connecting the molecular characteristics of a polymer melt with the structure development and kinetics when subjected to flow, and with the ultimate material properties.

## 1.2 Background

### 1.2.1 Quiescent crystallization in polymers

A polymer melt consists of coiled, mutually interpenetrating macromolecules, so achieving an ideal crystalline state is frustrated for kinetic reasons: Complete disentangling of the chains and arrangement into an array of elongated conformation has a very high entropic activation barrier. Thus, structure formation in polymers is kinetically controlled, so the final morphology developed is the one with the maximum growth rate at a certain temperature rather than the one with the lowest free energy. Thermodynamics still play a central role describing the driving forces for crystallization: The first-order transition is a relaxation of the metastable undercooled melt towards the equilibrium state, which requires overcoming a free energy barrier (dependent of the depth of undercooling) to introduce new interfaces (nucleation process). Quiescent homogeneous nucleation has traditionally been explained using classical nucleation theory; however, the debate on this topic continues as other possible mechanisms have been suggested [1-4].

Due to the kinetic frustration arising from chain connectivity, semicrystalline polymers usually organize into platelet-like crystallites by chain folding [5]. These crystalline lamellae are separated by non-crystalline regions. During crystallization from the melt in the absence of flow, typically lamellae undergo non-crystallographic branching and continue to splay and to grow, forming three dimensional morphologies that are called spherulites [6] (Figure 1-1).

### 1.2.2 Flow-induced crystallization in polymers

When flow is imposed, the morphology of crystallization can significantly change (Figure 1-2). Early studies in stirred polymer solutions [7] showed that the polymer crystallized onto a central core (shish) from which platelet-like crystals grew (kebabs). These type of structures were also deduced to occur in the bulk when cross-linked polyethelene was subjected to stress (row structures) [8]. The formation of oriented precursors (denominated shish, row-structures, and thread-like precursors in literature) is well established under the influence of both extensional [9-11] and shear flows [12-15]. These oriented entities are at the heart of the large effects produced by flow: They nucleate highly oriented crystallites and provide a large surface for nucleation (thus accelerating the overall kinetics of crystallization). There is no consensus about their nature or about the mechanism by which they are formed. It is generally accepted that the longest chains in a melt play a major role in the formation of oriented precursors [16-18], and that the stress has a strongly non-linear influence on their creation.

In the past, studies on flow-enhanced crystallization encountered obstacles due to experimental and material limitations. Recently, new experimental approaches that separate the effects of flow and thermal histories have been developed, so it is possible to probe with certainty the influence of processing conditions. Also, the advent of single-site catalysts has opened up the way for synthesis of model materials with high levels of control over molecular structure. The combination of the new experimental and synthetic capabilities has already triggered important findings: Evidence for a “non-classical” kinetic pathway to oriented nucleation in which molecular dynamics play the main role has been observed (as opposed to the subcooling for the quiescent case) [19], and flow-enhanced crystallization has been quantitatively proved to be strongly influenced by the distribution of chain lengths (specifically by the longest chains in the melt) [17].

The main motivation to discover the fundamental physics behind this phenomenon is to enable predictive models that relate molecular characteristics and processing conditions to final morphology. Without mechanistic understanding, it is not possible to develop comprehensive mathematical models for predicting the influence of resin characteristics and structure development in polymer processing. A number of empirical models have been formulated for flow-induced crystallization [20-22], but they are suitable only for a particular type of processing or limited experimental data, rely on a variety of adjustable parameters that do not account for the importance of crystalline morphology, and usually calculate only one pertinent value (such as an induction time or the degree of crystallinity). Capturing morphology development is essential not only because of its impact on ultimate material properties, but because anisotropic nucleation is at the heart of the remarkable effects of flow on polymer crystallization. A model developed by Janeschitz-Kriegl and coworkers [15] stands out because it takes into account the effect of morphology on structure evolution. Their model provides the basis for current state-of-the-art work in the group of Meijer at the Technical University at Eindhoven, which incorporates the effect of polymer dynamics and includes the physics of oriented precursor formation [23]. Experiments to test model assumptions and predictions are needed to ensure that relevant mechanistic steps are included and the values of pertinent rate constants are correctly related to molecular attributes and processing conditions. This is not a simple problem to overcome: Experimental protocols are needed that create precursors in a controlled way, under well-defined conditions that isolate the physics of their creation separately from the formation of crystallites onto them; model materials are needed to clarify the effect of molecular parameters; and finally, a strategy has to be developed to detect the precursors in a quantifiable way.

## 1.3 Cross-hatching in isotactic polypropylene

The most common crystal structure formed in isotactic polypropylene (iPP) is a monoclinic α-phase. This phase exhibits a type of lamellar branching (cross-hatching) that is unique in polymer crystallography, and that consists of a second population of lamellae (called "daughters") growing off epitaxially from the initial "parent" lamellae [24, 25]. The daughter lamellae grow at a nearly perpendicular direction to their parent lamellae. This cross-reinforcement in the nanostructure of the material gives excellent resilience to iPP. Consequently, iPP is used in enormous volumes for diverse applications.

## 1.4 Thesis organization

We begin by examining the role of ultra-long chains in flow-induced crystallization of a model polypropylene, and proposing a model of formation of thread-like precursors that differentiates two stages in their development. Our experimental capabilities provide us with real-time measurements that probe a range of shear stresses throughout a slit flow channel. Thus, in Chapter III we develop the "depth sectioning method" as a strategy to isolate the contribution to the real-time signal that arises from a specific level of shear stress, and we follow the development of thread-like precursors during shear at 137˚C. In Chapter IV we present a strategy to create and quantify thread-like precursors separately from the crystallites that grow on them, and we identify experimental conditions suitable to apply this approach within the heat transfer constrains of our apparatus. Finally, in Chapter V we combine these two methods to perform measurements that capture the birth, propagation, and saturation of the bare precursors; we discuss the implications of our findings in light of the state-of-the-art model from the Eindhoven group.

## 1.5 Figures

**Figure 1-1. Polarized optical micrograph of crystallized iPP showing spherulitic morphology**

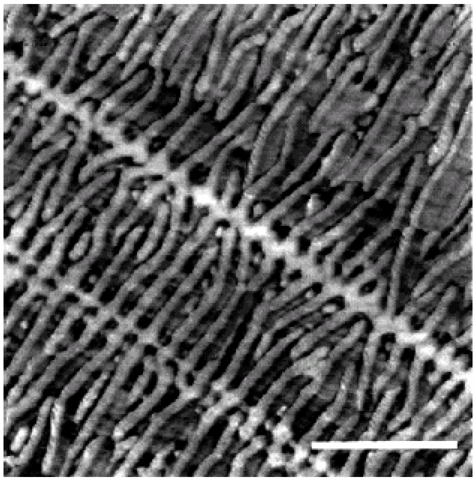

**Figure 1-2. AFM phase image showing shish-kebab structures formed by shearing a polyethylene film with a razor blade (Reprinted with permissiont from [26], Copyright 2001 American Chemical Society)**

## 1.6 References

1. Olmsted, P.D., W.C.K. Poon, T.C.B. McLeish, et al. *Spinodal-assisted crystallization in polymer melts.* Physical Review Letters, 1998. **81**(2): 373-376.
2. Terrill, N.J., P.A. Fairclough, E. Towns-Andrews, et al. *Density fluctuations: the nucleation event in isotactic polypropylene crystallization.* Polymer, 1998. **39**(11): 2381-2385.
3. Strobl, G. *From the melt via mesomorphic and granular crystalline layers to lamellar crystallites: A major route followed in polymer crystallization?* European Physical Journal E, 2000. **3**(2): 165-183.
4. Janeschitz-Kriegl, H., E. Ratajski, and H. Wippel. *The physics of athermal nuclei in polymer crystallization.* Colloid and Polymer Science, 1999. **277**(2-3): 217-226.
5. Keller, A. *A Note on Single Crystals in Polymers - Evidence for a Folded Chain Configuration.* Philosophical Magazine, 1957. **2**(21): 1171ff.
6. Padden, F.J., and H.D. Keith. *Spherulitic Crystallization in Polypropylene.* Journal of Applied Physics, 1959. **30**(10): 1479-1484.
7. Pennings, A.J., and A.M. Kiel. *Fractionation of Polymers by Crystallization from Solution .3. On Morphology of Fibrillar Polyethylene Crystals Grown in Solution.* Kolloid-Zeitschrift and Zeitschrift Fur Polymere, 1965. **205**(2): 160ff.
8. Keller, A.M., and M.J. Machin. *Oriented Crystallization in Polymers.* Journal of Macromolecular Science, Part B, 1967(B1): 41ff.

9. Pope, D.P., and A. Keller. *Study of Chain Extending Effect of Elongational Flow in Polymer-Solutions.* Colloid and Polymer Science, 1978. **256**(8): 751-756.

10. Keller, A. *Unusual Orientation Phenomena in Polyethylene Interpreted in Terms of the Morphology.* Journal of Polymer Science, 1955. **15**(79): 31-49.

11. Hill, M.J., and A. Keller. *Direct Evidence for Distinctive, Stress-Induced Nucleus Crystals in Crystallization of Oriented Polymer Melts.* Journal of Macromolecular Science-Physics, 1969. **B 3**(1): 153ff.

12. Haas, T.W., and B. Maxwell. *Effects of Shear Stress on Crystallization of Linear Polyethylene and Polybutene-1.* Polymer Engineering and Science, 1969. **9**(4): 225ff.

13. Wolkowicz, M.D. *Nucleation and Crystal-Growth in Sheared Poly(1-Butene) Melts.* Journal of Polymer Science Part C-Polymer Symposium, 1977(63): 365-382.

14. Andersen, P.G., and S.H. Carr. *Crystal Nucleation in Sheared Polymer Melts.* Polymer Engineering and Science, 1978. **18**(3): 215-221.

15. Liedauer, S., G. Eder, H. Janeschitzkriegl, et al. *On the Kinetics of Shear-Induced Crystallization in Polypropylene.* International Polymer Processing, 1993. **8**(3): 236-244.

16. Duplay, C., B. Monasse, J.M. Haudin, et al. *Shear-induced crystallization of polypropylene: Influence of molecular weight.* Journal of Materials Science, 2000. **35**(24): 6093-6103.

17. Seki, M., D.W. Thurman, J.P. Oberhauser, et al. *Shear-mediated crystallization of isotactic polypropylene: The role of long chain-long chain overlap.* Macromolecules, 2002. **35**(7): 2583-2594.

18. Vleeshouwers, S., and H.E.H. Meijer. *A rheological study of shear induced crystallization.* Rheologica Acta, 1996. **35**(5): 391-399.

19. Kumaraswamy, G., J.A. Kornfield, F.J. Yeh, et al. *Shear-enhanced crystallization in isotactic polypropylene. 3. Evidence for a kinetic pathway to nucleation.* Macromolecules, 2002. **35**(5): 1762-1769.

20. Isayev, A.I., and C.A. Hieber. *Toward a Viscoelastic Modeling of the Injection-Molding of Polymers.* Rheologica Acta, 1980. **19**(2): 168-182.

21. Guo, X., A.I. Isayev, and L. Guo. *Crystallinity and microstructure in injection moldings of isotactic polypropylenes. Part 1: A new approach to modeling and model parameters.* Polymer Engineering and Science, 1999. **39**(10): 2096-2114.

22. Doufas, A.K., I.S. Dairanieh, and A.J. McHugh. *A continuum model for flow-induced crystallization of polymer melts.* Journal of Rheology, 1999. **43**(1): 85-109.

23. Zuidema, H., G.W.M. Peters, and H.E.H. Meijer. *Development and validation of a recoverable strain-based model for flow-induced crystallization of polymers.* Macromolecular Theory and Simulations, 2001. **10**(5): 447-460.

24. Lotz, B., and J.C. Wittmann. *The Molecular-Origin of Lamellar Branching in the Alpha-(Monoclinic) Form of Isotactic Polypropylene.* Journal of Polymer Science Part B-Polymer Physics, 1986. **24**(7): 1541-1558.

25. Lotz, B., J.C. Wittmann, and A.J. Lovinger. *Structure and morphology of poly(propylenes): A molecular analysis.* Polymer, 1996. **37**(22): 4979-4992.

26. Hobbs, J.K., A.D.L. Humphris, and M.J. Miles. *In-situ atomic force microscopy of polyethylene crystallization. 1. Crystallization from an oriented backbone.* Macromolecules, 2001. **34**(16): 5508-5519.

*Chapter II*

# *The Role of Long Chains in Flow-Induced Crystallization*

## 2.1 Introduction

The effects of flow on polymer crystallization have been known for decades because most processing techniques involve the imposition of high stresses onto a melt. Processing flows can increase the kinetics of crystallization by orders of magnitude, and can induce the formation of highly oriented crystallites that, in turn, impact the final material properties in the solid state. For instance, this is the phenomena behind making ultra high modulus fibers by spinning and strong sheets by film blowing. It can also have undesired effects: The large differences in properties between a highly oriented layer on the surface of an injection molded article and the isotropic core can cause warping and delamination. In spite of decades of research, the fundamental mechanism of flow-induced crystallization remains elusive.

It has been inferred that the creation of some highly oriented shish or threads nucleate oriented crystallites on them, imparting the high orientation and increasing the surface available for nucleation (and thus the kinetics). We build on a basic model for flow induced crystallization developed by Liedauer *et al.* [1] which proposes that flow first induces the formation of point-like nuclei from which, if shear is continued and flow conditions are strong enough, thread-like precursors form and then nucleate oriented growth of crystallites on them (Figure 2-1). This model is similar to that of Keller and Machin [2] which proposes the formation of row-like structures (shish) from which kebabs develop.

Studies have also inferred that flow-induced crystallization is strongly influenced by polydispersity, particularly by the longest chains in the melt [3-6]. This has been an obstacle for investigation until the recent development of metallocene catalysts. Previously, Ziegler-Natta polymers possessing a broad molecular weight distribution were used, but because their longest chains are also the most regular, it was difficult to deduce whether the effect was due to either or both of these factors. In addition, the smooth distribution of the molecular weights makes it difficult to assess how long the chains have to be, how many of them are required, and how they interact within the mechanism of flow-induced crystallization.

The addition of small and known concentrations of well defined long chains into a matrix of relatively low polydispersity and lower molecular weight polymer aims at revealing the fundamental mechanism by which the long chains play a prominent role in flow-induced crystallization. This approach has been used with polypropylene by Seki and coworkers [7], and results suggested that the chains act cooperatively. We follow this approach with the addition of small amounts of ultra-high molecular weight polymer. The use of our experimental apparatus [8] allows us to control the level of stress imposed on the melt. In this way, we can make comparisons at fixed levels of stress, and therefore, similar average levels of segmental orientation.

The fundamental physics of flow-induced crystallization remains elusive in spite of decades of research; without this knowledge, physics-based models of flow-induced crystallization will fail to replace the current ad-hoc models that exist. If predictive models can be developed they will inform the molecular level design of molecules, allowing prediction of the kinetics and morphology of crystallization during processing to achieve the desired rate of production and materials properties.

## 2.2 Experimental

### 2.2.1 Materials

The materials used in this study were bimodal blends of isotactic polypropylene (iPP), designed to investigate the impact on flow-induced crystallization produced by scarce but well-known concentrations of high molecular weight chains mixed with a matrix of shorter chains. For this purpose, various proportions of two types of iPPs with vastly different molecular weights (Table 2-1) were solution blended. Both polymers were provided by Dow Chemical Co., synthesized using metallocene catalysis. The “short chain” component used as the matrix (Base-PP) had a moderate molecular weight ($M_w \sim$

186 kg/mol), narrow polydispersity ($M_w/M_n = 2.3$), and stereoregularity [mmmm] = 96%. The “long chain” polypropylene (3500k) had $M_w \sim 3500$ kg/mol, narrow polydispersity ($M_w/M_n$) = 1.8, and high stereoregularity ([mmmm] > 98%).

We prepared our model bidisperse materials by dissolving desired amounts of 3500k “long chains” (up to 2% in weight) and Base-PP (Table 2-2) in hot xylene under inert atmosphere until a homogeneous mixture was obtained, and then quickly precipitating into cold methanol. The resulting “fluff” was filtered and washed with methanol. Two thousand ppm of antioxidants (Irganox 1010 and Irgafos 168) were added to the polypropylene by dissolving them into acetone and spraying the resulting solution onto the polymer fluff. Finally, the polymer fluff was dried at 80°C under vacuum for several days to ensure removal of all remaining solvent. As a control, a blank material (B0) comprised of Base-PP with no long chains added was subjected to the same solution blending procedure as the bimodal samples.

Long chain concentrations $C_L$ up to approximately 5x$C_L$ were examined (Table 2-2), where $C_L^*$ is the long chains overlap concentration. At the overlap concentration [9, 10] the number of long chain coils per unit volume times the volume pervaded by one single coil $R_g^3$ is roughly unity:

$$c_L^* = \frac{3M_w}{4\pi\left(R_g^2\right)^{3/2} N_a}$$

where $M_w$ is the molecular weight, $R_g$ is the radius of gyration, and $N_a$ is Avogadro’s number. We employ $[(\langle R_g^2\rangle)^{1/2} / (M_w^{1/2})]$ obtained from SANS measurements, which is 0.39 Å/(g/mol)$^{0.5}$ for iPP crystallized at 137°C [11]. For our 3500k long chains, $C_L^* = 0.003572$ g/cm$^3$.

### 2.2.2 Differential scanning calorimetry (DSC)

DSC measurements were performed in a Perkin-Elmer DSC-7 instrument. Between 6-9 mg of samples were tested with heating and cooling rates of 5˚C/min, and under a $N_2$ atmosphere. The recorded values correspond to a second heating and cooling cycle.

### 2.2.3 Flow-induced crystallization instrumentation and protocol

Flow-induced crystallization experiments were performed in an apparatus [8] capable of imposing a strong shear pulse onto a polymer melt for a brief duration of time and under well-known thermal conditions. The experimental protocol (Figure 2-2) was as follows: First the flow cell was filled with the polymer melt at a low wall shear stress and 215˚C. It was held at this temperature ($T_{erase}$) for 5 minutes in order to erase any previous flow history and fully relax the melt [7]. Then, the melt was cooled down to $T_x$ (137˚C), and a brief and intense shear pulse corresponding to a specified wall shear stress ($\sigma_w$) was imposed for a specific shearing time ($t_s$). Subsequently, the polymer was kept isothermally at 137˚C, and the progress of crystallization was monitored with rheo-optical methods for 75 min. At this time, the flow cell was removed from the apparatus and cooled to room temperature over ~ 10 min. The crystallized polymer sample was subsequently extracted for additional ex-situ characterization.

The flow channel consists of a rectangular slit with aspect ratio ≥ 10:1 [8]. The total maximum strain that can be applied to the polymer melt is constrained by the geometry of the channel, as described in the supplemental information of [12]. The shear stress varies linearly from its value at the wall ($\sigma_w$) to 0 at the center of the flow channel in the $\nabla\mathbf{v}$ direction (Figure 2-3). The optical beam utilized for real-time measurements traverses the flow channel in the $\nabla\mathbf{v}$ direction.

### 2.2.4 In-situ rheo-optical characterization (polarimetry and turbidity)

The real-time optical measurements probe the optical anisotropy and degree of turbidity of the polymer sample during and after shear, as described elsewhere [8]. The optical anisotropy of the sample (when there is no significant depolarization due to multiple scattering) is manifested in the $I_\perp/(I_\perp+I_{||})$ signal:

$$\frac{I_\perp}{I_\perp + I_{||}} = \sin^2\left(\frac{\pi\Delta nd}{\lambda}\right) = \sin^2\left(\frac{\delta}{2}\right)$$

where $I_\perp$ is the intensity measured through crossed polars, $I_{||}$ is the intensity transmitted through parallel polars, $\Delta n$ is the birefringence, $d$ is the length of the optical path through the sample, $\lambda$ is the wavelength of the optical source, and $\delta$ is the retardance due to the sample.

The turbidity of the sample is monitored by normalizing the total intensity of the beam transmitted through the sample at a given time by the initial intensity that was transmitted through the melt before shear was imposed:

$$Turbidity = \frac{I_{total}}{(I_{total})_o} = \frac{I_\perp + I_{||}}{(I_\perp + I_{||})_o} \quad .$$

### 2.2.5 Ex-situ polarized optical microscopy (POM)

Sections in the flow-velocity gradient plane (**v**-∇**v**) were obtained from the quenched samples and imaged using polarized optical microscopy (POM). We obtained two sets of ex-situ micrographs for each sample: one with the polarizer (P) and analyzer (A) placed 45° and -45° to the flow direction, and one with the polarizer parallel to flow and the analyzer orthogonal to it.

### 2.2.6 Ex-situ WAXD

The wide angle x-ray diffraction (WAXD) patterns of selected quenched samples were recorded at the X27C beamline of the National Synchrotron Radiation Source (Upton, NY). The x-ray beam traversed the samples in the ∇**v** direction (that is, in the same direction as the laser beam employed for the optical measurements). The wavelength of the x-rays was 1.371 Å. Patterns were recorded with a MARCCD detector placed 17 cm from the sample. The camera length was calibrated with an $Al_2O_3$ standard.

The 2D WAXD patterns were normalized by the beam intensity, and the intensity corresponding to the background was subtracted. The azimuthal dependence of the scattered intensity was computed for the reflections corresponding to the (110) and (040) planes of the α crystal morph of isotactic polypropylene.

## 2.3 Results

### 2.3.1 Quiescent crystallization

The addition of a small concentration (1wt%) of 3500k long chains in the base resin Base-PP does not have a discernable effect on the morphology obtained after crystallizing for 14 hours at 137˚C in the absence of flow (Figure 2-4 top, left, and middle micrographs). Because crystallization was allowed to proceed for a long time at a relatively high $T_x$ for iPP before cooling the samples to ambient temperature, the final structure consisted mostly of very few large spherulites (up to 200 μm in diameter) that grew to a considerable size from the few nucleating sites activated at 137˚C. Hence, the coarse morphologies of B0 and 1p could be easily visualized and compared under the optical microscope.

The progress of quiescent crystallization kinetics (as monitored by the development of turbidity, Figure 2-4 bottom) did not show discernable differences with concentrations of up to 1% weight of long chains present in the sample. Note the two data sets for 1p that show the variation from run to run, which may result from the small number of nucleating events in the sample volume under quiescent conditions. Separate DSC measurements confirmed that the overall kinetics of crystallization and melting were not affected by the concentrations of long chains used for the samples in this study. In general for all samples, turbidity only became appreciable at $t > 3600$ s, and the turbidity half-times ($t_{0.5}$) were reached at $t > 10000$ s at the earliest.

For all subsequent flow-induced crystallization experiments, the samples were quenched after 75 min of isothermal crystallization at 137˚C. Thus, the resulting morphology in these flow experiments must be compared to a quiescent experiment with matched experimental protocol (Figure 2-4 top, right micrograph). When 1p was allowed to crystallize only for 75 min (Figure 2-4 top, right micrograph) instead of for 14 hours (Figure 2-4 top, center micrograph), the resulting morphology was also spherulitic but presented much smaller size scales. The development of turbidity (Figure 2-4, bottom) in real-time indicates that, unlike after 14 hours, at 75 min very little crystallization has occurred; thus, most crystallization must have occurred under non-isothermal conditions when the sample is already cooling. This explains the smaller size of spherulites: Lower temperatures activate a larger number of nucleating sites from which spherulites grow until they impinge with one another.

### 2.3.2 Effect of $C_L$ on types of flow-induced morphology

In contrast to quiescent crystallization, the final morphology obtained when flow is imposed on the melt depends strongly on the concentration of long chains ($C_L$). The ex-situ microstructure observed for identical flow-induced crystallization conditions ($T_x$ = 137˚C, $\sigma_w$ = 0.065 MPa, total mass extruded ~ 100 mg, and cool down after 75 min) shows no oriented skin for the sample with $C_L$ = 0% (B0), while the one with $C_L$ = 0.25wt% (025p) develops a thin birefringent layer near the wall, and the one with $C_L$ = 1wt% (1p) presents a qualitatively different morphology over most of its thickness—including a highly oriented skin ~ 60 μm thick (Figure 2-5, top to bottom).

The B0 sample (Figure 2-5, top row) presents coarse structures ("core-type" region) from the center of the channel (where the shear stress is zero) to the wall of the mold (where $\sigma_w$ = 0.065 MPa). This "core" area mainly consists of macroscopically isotropic [13] spherulitic structures: The images taken when the polarizer P is at 45˚ (left) and parallel (right) to the direction of flow are qualitatively similar. It is noteworthy that these micrographs do not look significantly different from the one corresponding to quiescent crystallization of 1p at 137˚C for 75 min then cooled to 25˚C (Figure 2-4, top far right).

Next, we examine the effect of adding just 0.25wt% of long chains (Figure 2-5, middle row). The region at lower stresses, near the center of the channel, presents the same core morphology as B0 above. However, at distances closer to the wall there is a wide "fine-grained" region consisting of smaller sized structures. This region appears isotropic (similar in the left and right micrographs). Finally, next to the wall (at the highest stresses) there is a thin irregular layer composed of a few oriented structures. These elongated "sausage-like" structures appear bright when P is 45° to flow (left), but not when it is parallel to it (right). The transition between the fine-grained region and the core-type region (indicated by a dashed line) does not appear sharp because the morphologies of these two areas do not look radically different under the optical microscope.

For long chain concentration of 1wt% (bottom row of Figure 2-5), the isotropic region near the center of the channel is quite narrow. At intermediate shear stresses (closer to the wall), there is a birefringent but irregular region with many oriented sausage-like structures. At last, for the highest shear stresses (close to the wall of the mold) we observe a wide and very highly oriented region—the "skin"—as is characteristically found near the surface of injection molded samples [14-17]. It is important to notice that the skin area is much more birefringent than the area densely populated with sausages (image on the left), and that the transition between these two regions (marked with a solid line) is very sharp. This distinction is very easily observed when P is along the flow direction (right image): the skin area appears completely dark, while the sausage area is observed as fairly dark striated structures. Also, note that the boundary between the inhomogeneous sausage area and the core (dashed line) is more irregular than the one with the skin.

### 2.3.3 Effect of shear stress on types of flow-induced morphology

The previous section showed how the addition of small concentration of long chains can have a significant impact on the final flow-induced morphology for fixed conditions ($\sigma_w$ = 0.065 MPa, $T_x$ = 137°C, and fixed total mass extruded). Next, we explored the combined effects of applied stress and $C_L$ by imposing a series of $\sigma_w$ (in the range from 0.03 MPa to 0.13 MPa) for different $C_L$s varying from 0% to 2% weight of long chains.

When we increased the applied wall shear stress to $\sigma_w = 0.11$ MPa for samples in the lower range of $C_L$s, we generated morphologies that were previously only accessible at the lower $\sigma_w = 0.065$ MPa for comparatively greater levels of $C_L$'s. In this fashion, we were able to induce a distinct fine grained layer near the wall in B0 (Figure 2-6 top, compare to previous Figure 2-5 top). Likewise, a highly oriented skin region was formed between the wall and a fine-grained layer for 025p (Figure 2-6 bottom, compare to previous Figure 2-5 middle where only a fine-grained layer was observed). Note that neither sample exhibits a region densely populated with sausage-like structures. However, single isolated sausages can be observed in certain parts of the samples (a small isolated sausage is visible in the top left micrograph of Figure 2-6).

On the other extreme, the samples with the greatest $C_L$s generated oriented morphologies even when a very small wall shear stress was imposed on them. When $\sigma_w = 0.037$ MPa is applied, 1p (Figure 2-7, top row) still shows an area densely populated with oriented sausages (although the highly oriented skin is not present now, as it was in Figure 2-5 bottom with $\sigma_w = 0.065$ MPa). For the sample that contains a $C_L$ of 2% in weight, even this weak level of shear stresses is able to generate both an area with dense sausage structures and a thick highly oriented skin (Figure 2-7, bottom).

Because of our flow geometry, we unambiguously know that the shear stress throughout the channel varies linearly from $\sigma_w$ at the wall to zero at the center (Figure 2-3). Thus, we calculated the shear stress that corresponded to the border between two regions of different morphology from the measured distance from the wall of the mold. As we have just shown in the previous optical micrographs (Figure 2-5 to Figure 2-7), as $\sigma_w$ increased the boundaries between morphological layers for a given $C_L$ shifted farther from the wall. When the stress corresponding to each boundary was computed, however, very small changes were observed: the position of the boundaries was well described by a corresponding threshold stress $\sigma^*_I$, where *i* denotes the type of boundary.

The boundary of the highly oriented skin is very sharp and very uniform across the width and length of the channel. On the other hand, the boundary between the sausage layer and the core is quite variable; similarly, the boundary between the fine-grained layer and the core is somewhat subjective. Therefore, the values of $\sigma^*_{\text{skin}}$ have smaller uncertainty than either $\sigma^*_{\text{fine-gr}}$ or $\sigma^*_{\text{saus}}$. Note that samples that had a thick sausage layer (e.g., Figure 2-5 bottom) only had a small core region, which precluded measurement of a fine-grained to coarse core boundary. The samples containing ≥ 0.5% weight of long chains ($C_L/C_L^* \geq 1.2$) all had thick sausage layers, so only $\sigma^*_{\text{saus}}$ is shown (Figure 2-8, top). At lower $C_L$, negligible “sausages” formed, so only $\sigma^*_{\text{fine-gr}}$ is reported.

The critical shear stress necessary to induce the highly oriented skin morphology ($\sigma^*_{\text{skin}}$) decreases strongly as the concentration of long chains $C_L$ increases to $C_L^*$ (Figure 2-8, top graph). Even the addition of just 0.125wt% of 3500k long chains, which is below the overlap concentration ($0.3 \times C_L^*$), greatly reduces $\sigma^*_{\text{skin}}$. Beyond $C_L^*$, the effect of additional long chains is weak: when the concentration of long chains is doubled from 0.5wt% to 1wt% ($2.4 \times C_L^*$), $\sigma^*_{\text{skin}}$ remains approximately constant, and further doubling to 2wt% long chains ($4.8 \times C_L^*$) only mildly reduces $\sigma^*_{\text{skin}}$.

On the other hand, for the range of low $C_L$s in which the critical shear stress between the fine-grained layer and the core could be measured, we observed that $\sigma^*_{\text{fine-gr}}$ notably diminished as 0.125wt% and 0.25qt% of long chains (up to $0.6 \times C_L^*$) were added to the base resin (Figure 2-8, top). Conversely, the samples that presented sausage regions (0.5% to 2% weight of long chains, corresponding to $1.2 - 4.8 \times C_L^*$) did not reveal any appreciable change in their $\sigma^*_{\text{saus}}$.

Previously, threshold shear stresses for transition to the highly oriented skin have been reported for bimodal blends that used the same base resin as this study (Base-PP) and the same flow-induced crystallization conditions, but using long chains with $M_w = 1\times10^6$ g/mol [7, 18] instead of the present $M_w = 3.5\times10^6$ g/mol. In both cases, addition of long chains reduces the stress required to trigger highly oriented growth. The magnitude of the reduction in $\sigma^*_{\text{skin}}$ for 3.5M long chains is remarkably stronger than that for 1M long chains (Figure 2-8, bottom). For both 1M and 3.5M most of the reduction on $\sigma^*_{\text{skin}}$ occurs at low concentrations of long chains, while the influence of $C_L$ on $\sigma^*_{\text{skin}}$ saturates beyond $C_L^*$ (at

$C_L/C_L^* \sim 0.5$ for 1M and at $C_L/C_L^* \sim 1.2$ for 3.5M). Interestingly, these long chain concentrations correspond to very similar volume fractions (0.4% of 1M and 0.5% of 3.5M long chains). Fine-grained layers were observed in the study with 1M chains [7], but areas densely populated by sausage-like structures were not discerned within the range of 1M concentrations tested.

### 2.3.4 Ex-situ WAXD

Ex-situ wide angle diffraction was used to investigate the degree of orientation of the specimens that had already been examined with polarized optical microscopy. For the lowest wall shear stress imposed ($\sigma_w = 0.037$ MPa), the azimuthal distribution of the (110) intensity (Figure 2-9, top) revealed that both 1p and 2p (corresponding to the micrographs in Figure 2-7, top and bottom rows, respectively) possessed noticeable degrees of orientation. The (110) reflection of the α-iPP crystal morph allows distinction between oriented parent lamellae (which have the polymer chain oriented along the direction of flow and grow perpendicular to it), and the daughter lamellae (which grow epitaxially from the parent lamellae at ± 80˚). From the azimuthal scan, it is evident that the resulting morphology of 2p (which corresponds mainly to oriented skin and to dense sausages, Figure 2-7 bottom) is much more oriented (smaller full width half maximum) than the one for 1p (which displays only a sausage area but no skin, Figure 2-7 top). In addition, the parent-to-daughter ratio is significantly higher for the 2p sample, which has a highly oriented skin.

The azimuthal (110) scans corresponding to the next higher stress ($\sigma_w = 0.065$ MPa, Figure 2-9 center) display large differences between the samples investigated: 1p (the only one of these that has an oriented skin, Figure 2-5 bottom) has very high degree of orientation with a relatively high ratio of parent-to-daughter peaks, while the azimuthal distribution is nearly isotropic for 025p (with a fine-grained layer and very few sausages, Figure 2-5 middle) and B0 (consisting only of a core region, Figure 2-5 top). Note that intensity recorded at azimuthal angles between the oriented parent and daughter peaks for 1p azimuthal scan is lower than that of 025p and B0. This is due to the smaller proportion of isotropic crystallites (which are the only ones that give scatter in those azimuthal sections) in 1p relative to 025p and B0.

The highest stress used ($\sigma_w$ = 0.11 MPa, Figure 2-9 bottom) does induce a significant degree of orientation in 025p (in accord with its oriented skin, Figure 2-6 bottom row), but B0 remains almost completely isotropic (consistent with its fine-grained and core regions, Figure 2-6 top).

### 2.3.5 Effect of $C_L$ and stress on in-situ crystallization kinetics

So far, we have examined the impact of long chain concentration and shear stress on the types of ex-situ morphology and final orientation characteristics. We now present the matching real-time kinetics of crystallization monitored during and after imposition of the shear pulse at fixed $T_x$ (137°C).

#### 2.3.5.1 Low stress ($\sigma_w$ = 0.037 MPa) at high $C_L$: sausages and skin

The real-time kinetics explored here correspond the ex-situ POM of Figure 2-7 and the ex-situ WAXD shown in the top graph of Figure 2-9; the wall shear stress $\sigma_w$ is greater than $\sigma^*_{saus}$ of both 1p and 2p, but only exceeds $\sigma^*_{skin}$ for 2p.

The real-time birefringence measurements clearly revealed that during the shear pulse, only 2p developed a birefringence upturn characteristic of formation of oriented precursors and crystallites on them (Figure 2-10 top, inset). Immediately after cessation of flow, the retardance of the 2p sample hardly relaxed at all and it started growing rapidly, passing over several orders (manifested as “peaks” and “valleys” in the measured $I_\perp/(I_\perp+I_\parallel)$ signal in Figure 2-10 top). In contrast, the retardance of 1p completely relaxed after shear was stopped, and it only increased slightly towards the end of the experiment.

Meanwhile, the development of turbidity (Figure 2-10, bottom) is at least over an order of magnitude faster than it was when no flow was imposed (Figure 2-4, bottom graph). In the quiescent experiments, we could never detect the development of any turbidity within the time scale shown in Figure 2-10 (up to t = 2000 s). It is interesting to note that the 2p transmitted intensity decays in two steps, and undergoes a temporary maximum at intermediate times, while the transmittance for 1p decays monotonically. The comparison of the polarimetry and turbidity curves for 1p indicates that at least part of the rise in $I_{\perp}/(I_{\perp}+I_{\parallel})$ is due to development of birefringent structures (i.e., it begins when turbidity is still so low that depolarization by multiple scattering is unlikely).

#### 2.3.5.2 Intermediate stress ($\sigma_w$ = 0.065 MPa)

Next we examine real-time structure development for conditions corresponding to the ex-situ POM of Figure 2-5 and WAXD of Figure 2-9, middle: the wall shear stress $\sigma_w$ = 0.065 MPa exceeds $\sigma^*_{skin}$ for 1p, but not for B0 and 025p.

The transient birefringence during shear shows that only 1p developed an upturn during the shear pulse (Figure 2-11, top) which did not fully relax after flow was stopped. Significant growth of retardance after cessation of flow only occurred for 1p sample (Figure 2-11, top).

The behavior of the transmitted intensity after the 0.065 MPa shear pulse decayed fastest for the highest concentration of long chains (1p), and it did so in a two-step process: There was an early and rapid drop followed by a plateau, and finally a second final decay of intensity took place (Figure 2-11, bottom). On the other extreme, the slowest turbidity development corresponded to the sample with no long chains added. The intensity decreased monotonically for both 025p and B0 (although it still occurred about an order of magnitude faster than for the quiescent experiments).

#### 2.3.5.3 High stress ($\sigma_w$ = 0.11 MPa) at low $C_L$: fine-grained and skin

The highest stress in this study was sufficient to induce highly oriented crystallization in 025p, but not B0 (optical micrographs of Figure 2-6 and ex-situ WAXD in Figure 2-9, bottom). Both samples develop a fine grained layer ($\sigma_w > \sigma^*_{fine\text{-}gr}$).

During the shear pulse, it is interesting to note that the in-situ birefringence initially rises to the same value for both 025p and B0 (Figure 2-12, top), which corresponds to the flow birefringence for a given level of stress (hence, average segmental orientation). A subsequent upturn above the melt birefringence is observed for 025p but not for B0. After cessation of flow, the birefringence only partially relaxes for 025p, and it starts growing soon with strong orientation (retardance going over orders). In contrast, the birefringence completely decays for B0 after flow is stopped and does not noticeably increase before the end of the experiment.

The time scales for decay of transmittance (Figure 2-12, bottom) are quite similar for both samples, much faster than under quiescent conditions. While the final decay (300-1000 s) is similar for the two samples, an early decrease is evident in 025p (10-40 s).

### 2.3.6 Effect of $C_L$ and $\sigma_w$ on time for upturn ($t_u$)

The time elapsed from the beginning of an imposed shear pulse and the time at which the upturn in birefringence due to oriented crystallization begins ($t_u$) was recorded for the $C_L$s and $\sigma_w$ for which it occurred. For each concentration of long chains, the magnitude of the time for upturn $t_u$ is strongly influenced by the wall shear stress, decreasing as $\sigma_w$ increases (Figure 2-13). For a fixed wall shear stress, the effect of long chain concentration has two regions for 3.5M long chains: At very low concentrations ($C_L/C_L^* \leq 1.2$) $t_u$ decreases with increasing $C_L$. However, for higher concentrations ($C_L/C_L^* \geq 1.2$), the concentration of long chains does not seem to noticeably affect the time at which the upturn occurs. Interestingly, $C_L/C_L^* = 1.2$ is the concentration of 3.5M long chains under which $C_L$ had a large impact on the critical shear stress for the oriented skin ($\sigma^*_{skin}$) while, for the larger concentrations investigated, $\sigma^*_{skin}$ remained approximately constant with increasing $C_L$.

The analogous $t_u$ data for the 1M long chains studied by Seki *et al.* [7, 18] are also included in Figure 2-13. The recorded $t_u$s were observed for three concentrations of long chains at a $\sigma_w = 0.12$ MPa. The times for the upturn remained constant for the three $C_L$s (which all belong to the range of concentrations for which the $\sigma^*_{skin}$ did not vary with the 1M $C_L$).

Our bimodal blend behaved qualitatively similar to the 1M model blend of Seki *et al.* [7] in that an overshoot did not occur upon inception of shear, which facilitated the determination of times for upturn even when they were small in magnitude. Other studies that utilized Ziegler-Natta polypropylenes [8, 19] did present overshoot when flow was started before reaching a plateau value.

## 2.4 Discussion

Data for both 1M and 3.5M indicate the following: 1) That the long chains play a major role in the creation of threadlike precursors, and 2) that the effect of long chains on creation of threads is cooperative. In contrast, the influence of long chains on the formation of point-like precursors is mild. We have found two types of oriented structures formed in our sample: the highly oriented skin, and sausage-like structures that appear fairly inhomogeneously, and whose probability of appearance seems to be related to the concentration of long chains. Although these two types of structures have a common origin, there are sharp differences in their formation. In the following, we discuss the characteristics attributed to the skin and the sausages, pointing out similarities and differences, so that they can be later placed in context when talking about the model for flow-induced crystallization.

### 2.4.1 Differences between highly oriented skin and sausage morphology

In our experiments, we have found two types of oriented structures: the highly oriented skin and the elongated birefringent sausages. Even in the cases where the density of sausages was high near the skin, the boundary between them remained sharp and the optical micrographs showed noticeable differences in the level of birefringence corresponding to each of them. However, they both must have in common a precursor that is able to impart high orientation to the crystallites that grow off it.

#### 2.4.1.1 Highly oriented skin

Relatively *small interspacings* between relatively *long threads* are key features of the formation of the highly oriented skin observed ex-situ. Our results are consistent with previous studies in which an unusual upturn in birefringence during shear was correlated with rapid growth of retardance after cessation of flow [19, 20] and with the ex-situ observation of a highly oriented skin [20]. A combination of in-situ optical and WAXD measurements with ex-situ POM and TEM characterization [20, 21] pointed towards the validity of the flow-induced crystallization model put forward by Janeschitz-Kriegl and coworkers [1], and suggested that the upturn is a signature of the generation of large amounts of oriented precursors (Figure 2-14 A). These threads appear to epitaxially nucleate oriented α-iPP crystallites with the polymer chain aligned along the flow direction. Thus, after cessation of flow, oriented lamellae grow off the large surface area provided by the thread-like precursors (Figure 2-14 B) until they impinge with the crystallites growing off neighboring threads (Figure 2-14 C). From these characteristic features of highly oriented skin, we deduce that a successful model of the flow-induced transition to highly oriented growth must include two key features of precursor formation during flow in this region: 1) There must have been many precursors that initiated threads, and 2) once initiated, the threads continued to add length reaching ~ 10 μm without interruption.

When shearing stops, the retardance partially drops (because of the relaxation of the melt flow birefringence) and rapid highly oriented growth of crystallites proceeds (Figure 2-14 B), as indicated by the quick development of retardance. The fast crystallization kinetics and the fact that the growth is highly oriented are both direct consequences of the epitaxial nucleation on long slender threads which are present in large quantities. The oriented lamellae growing off the line nuclei are constrained by geometry: because other highly oriented lamellae are growing close to them, they prevent each other from diverging and they continue to grow in a highly oriented fashion. Only the lamellae growing near the ends of the threads have a chance to diverge as the geometry approximates that of spherulitic growth from a point-nucleus. However, because the threads are relatively long, the amount of growth occurring on end-caps is comparatively very small. After cessation of flow, the growth of kebabs occurs under quiescent conditions: the melt has already relaxed, and prior literature shows that the geometry of nucleation (point-nuclei vs. row-nuclei) does not affect linear growth rates, lamellar thicknesses, or degree of cross-hatching [22]. Therefore, the presence of a large surface area that nucleates oriented lamellae is responsible for the very rapid crystallization that occurs in the oriented skin.

So far the data indicates that very long slender precursors are formed during flow (lamellae propagate outward radially with high fidelity) and there are many of them (the volume swept out by cylindrulites grows very rapidly). Next, the transient optical properties provide evidence that the threads are closely spaced. The small distances between threads are manifested in signatures of impingement of oriented lamellae after a relatively short time (Figure 2-14 C). Signatures of impingement include a more or less sudden leveling of the growth of either retardance [1, 19] or highly oriented WAXD peaks [21]. For conditions that induce a highly oriented skin, we observe a decrease in growth rate of retardance at ~ 100 s. Like Langouche found [19], this leveling-off correlates with a related feature in the transmittance: a plateau or even an increase of transmittance (Figure 2-15). Scattering arises from optical density contrast: The early decay in transmittance is due to the contrast between the growing cylindrulites and the melt. When the cylindrulites grow past the point of occupying 50% of the volume, the skin region becomes optically more homogeneous and loses scattering ability. This type of effect is very clear in the experiments of Langouche in which the optical path length is small and the morphology is independent of depth (Figure 2-16). In our case, the evidence of the increase in transmittance of the oriented skin is more subdued—observed as a plateau or a rise prior to continued decrease in transmittance due to crystallization deeper in the sample. Other studies of crystallizing polymers have observed this type of effect in transmittance and have also attributed them to impingement between structures [19, 23].

After cooling and extracting the sample, the skin area maintains a high degree of orientation, as expected, since most of the crystallization (which was highly oriented) occurred well before cooling to ambient temperature (~ 100 s vs. ~ 1000 s). It is possible that some degree of secondary crystallization occurs after impingement while still holding the polymer isothermally at $T_x$, and that thinner lamellae may form in available spaces while the sample is being cooled to room temperature. TEM micrographs in previous studies and our ex-situ WAXD seem to indicate that if this is the case, any further crystallization in the skin is probably constrained to have high degree of orientation by the surrounding highly oriented lamellae.

#### 2.4.1.2 Sausage-like structures

Highly birefringent and elongated structures (denominated here “sausages”) are commonly evident in ex-situ polarized optical micrographs of specimens subjected to flow-induced crystallization [1, 7, 20]. In many cases, they appear as more or less isolated and sporadic structures[1]; also, a previous study attributed the observation of this type of structures to a gradual transition between the skin and a fine-grained layer in which thread spacing increased continuously for a Ziegler-Natta sample [24]. However, in our investigation, we turn our attention to these structures, because for the greater concentrations of 3.5M long chains used ($C_L \geq 0.5\%$), we find extended regions densely populated with sausage-like birefringent structures that are clearly distinct from the oriented skin: The boundary with the skin remains sharp and visibly distinguishable, and the degree of birefringence abruptly changes in this border. From this we deduce that our dense sausage region does not correspond to a gradual decay of the skin, but that there is some fundamental step in its formation that clearly differs from that of the highly oriented skin. Our results indicate that sausages arise from the same long thread-like precursor as those in the skin, but they are present at considerably lower concentrations.

During flow, no upturn was observed for the experiments in which only sausages formed suggesting that, although some thread-like precursors (and possibly some oriented crystallites on them) are created, their contribution to birefringence is not enough to be

---

[1] The studies cited that present optical micrographs where birefringent elongated structures do not focus on these features. So although "sausage"-like structures appear in this investigation, the subjects of attention are in general the highly oriented skin and the fine grained layer. Some studies have considered that the threads of the oriented skin progressively appear further apart. However, the sharpness observed in our samples suggests that it may not be just a continuous decrease in thread interspacing.

detected above the melt flow birefringence. After flow is stopped, no noticeable growth of retardance occurs (although kebabs will be growing on the sparse threads created). Only after a relatively long time at 137˚C and for the samples that contain relatively substantial quantities of sausages as observed ex-situ can the total volume of the growing oriented crystallites become sufficiently large to produce a small increase in retardance. All these traits point towards the conclusion that the total thread-length per unit volume created in the sausage area is quite low (in contrast to what occurs in the skin). Ex-situ optical microscopy confirms that threads created in the sausage region are far apart from one another, as we are able to resolve individual sausages with the resolution of our optical micrographs.

By the time the sample cell is extracted and starts cooling down, we expect that the sausage diameters are still relatively small. However, as temperature decreases during cooling, growth can continue in an oriented manner. Birefringent sausages can reach significantly large diameters, particularly if they are very far from other sausages. Thus, our results suggest that a significant part of the oriented crystallization in the sausage region occurs while cooling down.

The orientation distribution of the sausage area as observed ex-situ appears qualitatively less well oriented (Figure 2-5 bottom, Figure 2-7 bottom) and with a lower parent-to-daughter ratio (P:D) relative to the skin (Figure 2-9 top, 1p sample). The key difference is that, in the skin, the threads formed during shear are highly concentrated with very small distances between them. Everything else about the precursors to sausages may be the same as for the thread-like precursors in the skin. They propagate to similar lengths during the shearing time (tens of microns). Thus, the orientation distribution of kebabs growing off a sausage thread as well as their characteristic P:D ratio must be similar to that from threads in the skin until the time that the latter ones stop growing because of impingement. As the growth front progresses further in distance, it has been observed to become less orderly [1]. This suggests that in the case of sausages, the kebabs grow up to such long distance and time that they are able to become more divergent, hence the lower degree of orientation observed (Figure 2-17). In addition, whatever growth occurs after the experimental time at $T_x$ reflects non-isothermal effects (e.g., on the P:D ratio, which is strongly dependent on temperature [22, 25, 26]).

### 2.4.2 Model for creation of thread-like precursors: the role of long chains

In the following, we review and extend a conceptual model to explain the role of the long chains in formation of a thread.

Previous studies have observed that thread-like nuclei do not appear until after the point nuclei population has built up, suggesting that formation of point-like precursors is a prerequisite for inception of shish formation [1]. Therefore, the process of creation of a thread begins with a point-like nucleus already present in the melt [7]. Here, we do not treat the creation of the point-like nuclei caused by shear; we assume that the point-nuclei have already formed and that something "special" can occur once they are present.

Based on morphological evidence presented above that the shish can propagate to great length (tens of microns) at stresses much lower (~ ½) than the threshold to prolifically create shish, the present model describes both a threshold stress to propagate a shish and a greater threshold stress to convert a point-like precursor into a propagating one. Previously, only one threshold stress was considered [7]. For this purpose, we consider two different phases in the development of a thread from a point-like precursor: 1) The thread is able to start growing from the point-nucleus ("kick-off" stage), and 2) once the thread has been started, it continues growing in length ("propagation" stage). Note that this model considers a bimodal polymer melt that contains a very low concentration of long chains (so that there is no significant long chain-long chain entanglement).

After describing the conceptual model, we show that it is compatible with the observed morphology, the change in behavior between 1M and 3.5M long chains and the effect of $C_L$.

#### 2.4.2.1 Starting the thread: enhanced orientation of adsorbed long chains

Our description of the first step of formation of a thread-like precursor seeks to capture the conditions under which an elongated long-lived structure can develop from an already present point-like nucleus in the melt. The longest molecules in the melt are known to have a particularly important role in formation of thread-like precursors. This is thought to arise from a high state of orientation or from the occurrence of some chain stretching preferentially in the long chains, because they are particularly slow-relaxing species in a melt mostly consisting of shorter chains (thus, as a result of a high $M_L/M_s$ ratio). Based on these remarks, we consider that the transition from a point-like nucleus to a thread-like nucleus occurs when the order in the material just upstream (or downstream) from the point-like precursor increases stably to a sufficient level. Furthermore, the involvement of long chains in the generation of a high level of orientation in the vicinity of a point-like precursors is essential. Like Seki *et al*. [7], we invoke the adsorption of a long chain on a point-like nucleus during shearing in a molecular mechanism to increase the level of orientation near the point-like nucleus. This is the first step for the start of a shish in our model. The tethering of short chains on the point-like nucleus also occurs (especially given their much larger volume fraction), but their relaxation is so rapid that, even in a tethered state, they have little effect.

In this section, we qualitatively discuss the “high” orientation necessary to bring about the transition to a long-lived type of structure (specific characterization remains the source of debate and investigation). Van Meerveld *et al*. [27] note that the transition from enhanced point-like nucleation to shish-kebab structures tends to correlate with the occurrence of some chain stretching. Both the degree of orientation and the possibility of chain stretching for the longest molecules depend strongly on the ratio of $M_L/M_s$. The present qualitative discussion provides the framework for semi-quantitative comparison of the effects of 3.5M vs. 1M long chains in bidisperse blends (below).

With these considerations in mind, we present the following conceptual model that builds on the ideas of Seki *et al* [7]. Starting a thread preferentially involves long chains that flow past a pre-existing point-like nucleus in the melt (Figure 2-18 A). There is a chance that some segment belonging to the long chain may adsorb onto the point-like nucleus (Figure 2-18 B). If it does and flow is still sustained, most of the long chain molecule will not "know" that it is tethered and will continue flowing past the nucleus. This will impose an increased tension particularly in the segments of the long chain closer to the tethering point, which will therefore become particularly oriented (Figure 2-18 C). In our schematic, we represent this as a "streamer" that emanates from the point-like nucleus: Near the tethering point, a characteristic length $\xi$ will have particularly high segmental orientation, while the rest of the streamer, further away from the tethering point, will be mostly "lumped" near the free end because it does not "know" yet that the long chain is tethered. The probability that the neighboring chains form a long-lived ordered structure increases strongly with the average orientation locally. It is the enhanced orientation of the $\xi$ section of the adsorbed long chain(s) that is responsible for elevating by orders of magnitude the probability of adding ordered material adjacent to an existing precursor (Figure 2-18 D). When this occurs, the thread has "kicked-off" from the point-like nucleus.

At a given shear stress ($\sigma$), the frequency of kick-off events is highly affected by $M_L/M_s$. Therefore, the ratio of molecular weights will strongly affect the level of local stress at which a high concentration of threads can occur. So far in the description of this first stage, we have illustrated only the case in which one single long chain tethers to the pre-existing point-like nucleus. With increasing $C_L$, it becomes more likely that during shear, multiple long chains may be adsorbed on a given point like nucleus. The interaction between long chain streamers may increase the probability that neighboring chains achieve enough orientation for transition to a long-lived structure for a given stress [7].

#### 2.4.2.2 Propagation of the thread

Next, we consider the physics of propagating a shish after it has been kicked-off. In addition to the adsorption process above, growth of a shish via a propagating front advancing through space allows it to incorporate chains in its path. In contrast to adsorption (which requires diffusive or convective transport of chains to the surface of the shish), incorporation by the propagating tip occurs by overtaking chains that have zero relative velocity compared to the shish (they are on the same streamline). Thus, the long chains required to maintain the propagating front may be supplied by adsorption or incorporation or both. When this occurs, new streamers with a sufficiently oriented portion $\xi$ can form and continue the elongation process (Figure 2-19 A). Therefore, we can expect that whether the propagation occurs or not may be highly dependent on the presence of other long chains nearby (i.e. on $C_L$).

First we consider the situation when $C_L \geq C^*$. In this case, finding a long chain near that can incorporate and propagate the shish should be relatively easy (Figure 2-19 B): long chains pervade all the volume so finding one of them is not a limiting factor. However, the situation changes for $C_L < C^*$ (Figure 2-19 C1): A long chain may not be readily available near the shish end, so propagation of the thread depends on whether another long chain can be found while shearing is still imposed.

1. If the length $\xi$ is equal or larger than the characteristic center-to-center distance between the dilute long chains at a given $C_L$, the thread is likely to "intercept" a long chain within its reach $\xi$ (Figure 2-19 C2). The new addition will cause a further increase in thread length on the order of $\sim \xi$, so "catching" another long chain is likely again. The repetition of this sequence of events during shearing can cause rapid propagation of the thread, and will be dependent on the magnitude of $\xi$ and on $C_L$. In turn, $\xi$ is expected to be greater for larger $M_L/M_S$ and increasing stress imposed $\sigma$.

2. Long chains may flow past the thread due to the imposed shear flow (Figure 2-19 C1). For increasing $C_L$, it becomes more likely that a smaller distance will have to be spanned by a long chain to flow near the thread. Also, the velocity at which a long chain flows will scale as $\sim R_{g,L}\times$(shear rate), $R_{g,L}$ being the radius of gyration of the long chain. Thus, this type of event will become more probable for higher $C_L$, higher shear rate (thus higher $\sigma$), and possibly $M_L$(as it affects $R_{g,L}$).

Thus, for $C_L<C^*$, there is an interplay between $C_L$, $M_L/M_S$, and the stress $\sigma$ that determines whether propagation will occur. Then, once $C^*$ has been reached, further increase of long chain concentration (but still at concentrations below entanglement between the long chains themselves) may not significantly further enhance the propagation of the thread-like precursors.

### 2.4.3 Generation of threads in the highly oriented skin and in the sausage region

We described earlier that both the skin and the sausage morphologies arise from the formation of threads during shear, but with greatly different concentration. The skin is characterized by a very large number of threads per volume. This means that two conditions must be met to form a highly oriented skin: The stress is above $\sigma_{\text{kick-off}}$ and propagation is successful as well (which depends on an interplay of variables as explained above). The fact that we are above $\sigma_{\text{kick-off}}$ is crucial.

The relatively isolated threads characteristic of sausage regions suggest that they form at stresses below $\sigma_{\text{kick-off}}$, where very few of the point-like precursors convert to propagating shish. A dust particle or some sort of inhomogeneity in the flowing melt may be responsible, creating a stagnation point near which local levels of stress are high enough to induce the start of a shish. The formation of sausages depends strongly on $C_L$, most evident near and above overlap for 3.5M chains where threads can propagate over long distances. This suggests that once a relatively unusual event starts the shish, then the propagation easily continues if $C_L>C^*$.

Adequate identification of the parameters that preferentially generate a skin or a dense sausage area is also important because the final properties in the solid state depend on the final morphology obtained in the polymer. It is well known that crystallinity, permeability, and mechanical properties are strongly dependent on the level of orientation, but the nature of these correlations is gross in nature (without taking into account the detailed structure). Thus, development of a model that accurately captures the occurrence of both types of regions for specific molecular parameters and processing conditions is important.

### 2.4.4 Effect of $M_L/M_S$ on formation of threads: 3.5M and 1M blends

The data (and model) suggest that $M_L/M_S$ has a strong effect on the kick-off stress. Consider first concentrations near C*, to focus on the intrinsic limitations due to $M_L/M_S$ when the arrival or supply of long chains is not limiting (they pervade all volume, and $\sigma^*_{skin}$ has saturated). The strong effect of $M_L$ holding $M_S$ fixed is very clear in the comparison of $\sigma^*_{skin}$ at and above $C_L \approx C^*$: The threshold stress $\sigma^*_{skin}$ at $C_L/C^* \approx 1$ is a mere 0.04 MPa for $M_L$ = 3.5M—less than half the stress required when $M_L$ = 1M (Figure 2-8 bottom). The model anticipates that $M_L$ will have a strong effect at fixed $M_S$ at $C_L \approx C^*$, because the onset of chain stretching will be governed by the chain length equilibration time of the long chains, which will be accessible first for adsorbed long chains.

The chain length equilibration time of the adsorbed long chains may be estimated roughly by using a simple argument. Adsorption of a small portion of a chain may be viewed as dividing the chain into two dangling strands, the longer strand having length between (N/2) and N (the length of the entire chain). It is this longer strand that has the lower threshold for undergoing stretching. Chain stretching occurs when the deformation rate is faster than the relaxation of the contour length of the chain, given by its Rouse relaxation time $\tau_R$ [28]. A tethered chain of a given length has Rouse modes equivalent to a free chain of twice that length. The onset of chain stretching of adsorbed long chains will occur first for chains that adsorb near one of their ends. Since the Rouse time varies quadratically with chain length, such a long dangling strand will have roughly 4-fold longer Rouse time than a free chain.

In our bimodal blends, the concentration of long chains is very low. Because we are considering blends that contain very few long chains in a matrix of shorter chains, the viscosity changes very little with the addition of long chains. Therefore, for a given applied stress σ, the resulting shear rate will be on the order $\sim \sigma/(\tau_S G_N^\circ)$. The base resin has viscosity $\eta_S = G_N^{\circ}\tau_S$, where $\tau_S$ is the reptation time of the short chain and $G_N^{\circ}$ is the plateau modulus of polypropylene; all blends have $\eta \in (\eta_S, 2\,\eta_S)$.

Therefore, chain stretching is expected to occur when the shear rate, $\sigma/(G_N^{\circ}\tau_S)$, exceeds the inverse of contour length relaxation time of a tethered long chain $4\tau_{R,L}$. Thus, the threshold stress for kick-off is expected to scale as $\sigma^*_{\text{kick-off}} \sim (\tau_S\, G_N^{\circ})/(4\,\tau_{R,L})$. This sets the stage for understanding why adsorption of long chains to a precursor has such a large effect beyond that of adsorbed short chains, and why the increase in $M_L$ from 1M to 3.5M has a profound effect. Because the shear rate scales as $1/\tau_S$, it is useful to examine all relaxation times of all species in units of $\tau_S$, the reptation time of the short chains ($N_S$ units long). The contour length relaxation time of the short chains is

$$\tau_{R,S} = \frac{N_e}{3N_S}\tau_S$$

and for an adsorbed short chain it is $4\tau_{R,S}$. For a long chain of length $N_L$ units, its reptation time is roughly:

$$\tau_L = \left(\frac{N_L}{N_S}\right)^3 \tau_S$$

its contour length relaxation time is

$$\tau_{R,L} = \frac{N_e}{3N_S}\left(\frac{N_L}{N_S}\right)^2 \tau_S$$

and for an adsorbed long chain it is 4-fold longer. For the short chains, even adsorbed ones, their contour length remains fully relaxed when the shear rate is $\leq 1/\tau_S$, as shown in Figure 2-20. Even for chains of 1M, the free chains do not stretch; however, adsorption slows contour length relaxation enough that it is near the threshold for onset of chain stretching. The significant feature of chains of 3.5M relative to 1M is that the adsorbed chains clearly can undergo chain stretching, and even free long chains of 3.5M have a greater propensity for chains stretching than the adsorbed 1M long chains.

### 2.4.5 Cooperative role of the long chains—effect of $C_L$: 3.5M and 1M blends

The observation that the critical stress for formation of highly oriented skin in the 3.5M decreases for increasing $C_L$ up to C* indicates that the long chains act cooperatively to create the high thread-length per volume responsible for the formation of a highly oriented skin. If it were a single chain effect, then the threshold stress would not change significantly with concentration; at any given stress the rate of the process (proportional to thread-length/volume) would simply increase in proportion to $C_L$ (with no saturation or leveling off). For example, at a stress of $\sigma_w$ = 0.065 MPa, the effect of long chains qualitatively changes as $C_L$ doubles from 0.5C* to C*, which cannot be explained by simply doubling the rate of processes active in the $C_L$ = 0.5C* material. In contrast, as $C_L$ increases, the kick-off and propagation stage become highly successful at progressively lower stresses with increasing volume pervaded by the long chains. At least two types of interactions between long chains can contribute to the observed reduction of $\sigma^*_{skin}$. First, if more than one long chain can adsorb during shearing to the point-like nuclei (which is more likely as $C_L$ increases), the interaction between the streamers can increase the local level of orientation; therefore, the macroscopic stress required to form a long-lived nuclei decreases as $C_L$ increases. Second, the addition of material to the growing tip will be increasingly rapid as the supply of long chains increases.

For $C_L \geq$ C*, $\sigma^*_{skin}$ decreases very slowly with increasing concentration, suggesting that the effect of long chain concentration on the critical stress has saturated. On one hand, the decrease of $\sigma_{kick\text{-}off}$ due to long chain adsorption may saturate if limited by the number of available adsorption sites. On the other hand, the rate limiting factor for the propagating tip of the shish will not be the capture of long chains, as the whole volume is already pervaded by them.

This physical picture is consistent with the effects of $C_L$ observed for $M_L$ = 1M g/mol [7, 18] and our 3.5M g/mol. In both cases, $\sigma^*_{skin}$ decreased with increasing $C_L < C^*$ and saturated near $C_L \approx C^*$. Distinctions between the two cases are also compatible with the present physical picture. In the case $M_L$ = 1M, only $\sigma^*_{skin}$ was evident (there were not densely populated sausage areas as in the 3.5M), so we infer that $\sigma^*_{skin} \approx \sigma^*_{saus}$ (equivalently $\sigma_{kick\text{-}off} \approx \sigma_{prop}$) in the case of 1M long chains. Perhaps the relative ease of propagation compared to kick-off that is evident for 3.5M results from the more pronounced ξ-portion of a tethered 3.5M chain; hence, the greater reach of the downstream strand, facilitating recruitment of nearby chains and including capture of long chains in the path of propagation once it has been started. The facile formation of a stretched ξ-portion of an adsorbed 3.5M chain ($4\tau_{R,3.5M} > 10\tau_S$) may also explain why the addition of as little as 0.3C* has a strong effect, while very weak changes in flow-induced crystallization were seen at 0.25C* for 1M ($4\tau_{R,1M} \approx \tau_S$). In relation to the effect of concentration, the marginal case of $M_L$ = 1M g/mol may lead to the necessity that $C_L \geq 0.5C^*$ in order to have much effect at all.

### 2.4.6 Effect of long chains on formation of point-like precursors

Flow is known to create point-like precursors even at levels of stress that are too low to produce the transition to highly oriented growth. In general, the formation of point-like nuclei by flow depends on the temperature of shearing, on the level of stress, and on shearing time [29]. The nature and process by which these point-like precursors are created remains obscure, although some possible mechanisms have been suggested (such as the coalescence of athermal nuclei [30], or a certain degree of molecular extension [5]).

A previous study of the effect of long chains of a different molecular weight (1M instead of our 3.5M) did not find evidence of an effect of the long chains on point-like nuclei [7]. The present results provide evidence of an effect of the long chains on the number of point-like precursors formed during shear: We observe a fine-grained layer at progressively lower stresses as $C_L$ increases to 0.5%. The reason this effect is evident for 3.5M and absent for 1M may trace back to the relaxation rates of the long chains of 1M and

3.5M relative to the short chains, particularly to our estimation that the longer 3.5M chains may undergo some chain stretching even when they are free in the melt. At present, we cannot tell if the effect of $C_L$ is linear (a single chain effect) or nonlinear (depending on two or more long chains). The reason for this ambiguity is the following: Our optical micrographs do not allow us to infer the nature or the number of those small sized structures. Therefore, we are not in a position to compare the number of point-like nuclei formed at a given stress in two samples with different long chain content, which would be required to deduce the dependence on $C_L$. Future studies that include transmission electron microscopy would allow us to survey the number and size of spherulites.

### 2.4.7 Time for upturn

The time for the birefringence upturn is related to the development of the highly oriented skin: When a large amount of thread-like precursors form (and possibly with some oriented crystallites already growing on them), they induce a sharp rise in birefringence beyond the melt flow birefringence. Thus, the upturn can be considered as a measure of the time elapsed from the inception of shear through the formation of point-like nuclei to prolific kick-off and propagation of threads. At a given shear stress, the time for upturn does not change much for increasing $C_L$s above C*, where the effect of long chain concentration on the formation of threads has saturated, and the thread readily finds long chains close by to proceed with propagation. This suggests that, for a given applied shearing stress, the time for build-up of point-like nuclei is relatively similar for different $C_L$s, and therefore the changes in $t_u$ would be dominated the time necessary for kick-off and propagation to occur at different long chain concentrations. With decreasing $C_L$s below C*, it takes longer times to achieve the upturn. In view of our proposed model, this suggests that the adequate supply of long chains for kick-off and propagation may take a longer time to occur effectively when they do not pervade all the volume. In the case of 1M chains, the upturn could only be observed for the concentrations 0.5C* and above, and remained constant over this range, as did the corresponding $\sigma^*_{skin.}$

## 2.5 Conclusion

The addition of ultra-high molecular weight long chains (3.5M) to a matrix of shorter chains (180k; i.e., $M_L/M_S \approx 20$) can trigger the prolific creation of thread-like precursors even at long chain concentrations $C_L$ much lower than the overlap concentration C*, manifested as a strong reduction in the critical shear stress for transition to highly oriented skin. This adds to the evidence that the long chains act cooperatively to form the shish, and shows that as $M_L$ increases to $20\times M_S$, the effects of long chains are even significant at low $C_L$s at which they do not pervade the whole volume. Above C*, their effect saturates, indicating that the supply of long chains to be involved in formation of the thread is no longer a limiting factor. Also, we have shown that there appear to be two stages in thread formation from an already present point-like nuclei (kick-off and propagation) and that the stress requirements for kick-off are more stringent than the stress required for propagation of the thread ($\sigma_{\text{kick-off}} > \sigma_{\text{prop}}$). Thus, if an unusual event causes a kick-off at a lower macroscopic stress than the critical stress for the skin, the thread may propagate for tens of microns if $\sigma > \sigma_{\text{prop}}$.

In hindsight, prior experiments using long chains of 1M g/mol ($M_L/M_S \approx 6$) are now seen to be a marginal case: Only when tethered would the long chains experience chain stretching. By moving to significantly longer chains, it becomes possible for tethered chains to develop a strongly oriented portion near the adsorption site. Indeed, we believe this produced a dramatic increase in proliferation of shish. The data are consistent with the hypothesis that the interaction of long chains with the tip of a shish creates a local orientation that is not found elsewhere in the flowing melt. The results anticipate that a molecular perspective on chain dynamics in the melt and when adsorbed to precursors may provide predictive models linking MWD and flow conditions with the resulting kinetics and morphology of crystallization.

## 2.6 Tables

| | $M_w$[a] (kg/mol) | $M_n$[a] (kg/mol) | $M_w / M_n$ | [mmmm][b] (mol%) | $T_m$[c] (˚C) |
|---|---|---|---|---|---|
| ***Base-PP*** | 186.0 | 86.9 | 2.3 | 96.0 | 149.3 |
| ***3500k*** | 3500 | 1950 | 1.8 | > 98 | 144.3 |

**Table 2-1. Molecular characteristics of the isotactic polypropylene components used for the bimodal blends**

**[a] Determined by GPC-MALLS.**

**[b] $^{13}C$ NMR.**

**[c] The apparent melting temperature was determined as the peak temperature of differential scanning calorimetry (DSC) on second heating with scanning rate of 5°C/min and under $N_2$ atmosphere.**

| | ***weight % of 3500k*** | ***$C_L^a \times 10^{-3}$ (g/cm$^3$)*** | ***$C_L / C_L^*$*** | ***$T_x^b$ (˚C)*** | ***$T_m^b$ (˚C)*** |
|---|---|---|---|---|---|
| ***B0*** | 0 % | 0 | 0 | 109.9 | 149.6 |
| ***0125p*** | 0.125 % | 1.07 | 0.3 | 111.3 | 151.1 |
| ***025p*** | 0.25 % | 2.14 | 0.6 | 110.9 | 150.2 |
| ***05p*** | 0.5 % | 4.27 | 1.2 | 110.6 | 150.5 |
| ***1p*** | 1 % | 8.54 | 2.4 | 110.8 | 149.6 |
| ***2p*** | 2 % | 17.08 | 4.8 | 110.8 | 149.6 |

**Table 2-2. Characteristics of the bimodal blends of 3500k long chains into Base-PP short chains**

**[a] Concentration of 3500k long chains**

**[b] Determined as the peak temperatures of differential scanning calorimetry (DSC) on second cooling and heating, respectively. The scanning rate was 5°C/min. Measurements were performed under $N_2$ atmosphere.**

## 2.7 Figures

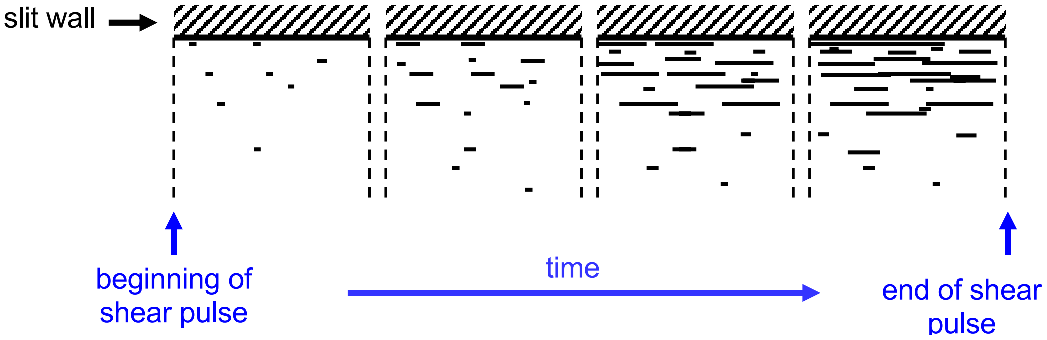

Figure 2-1. Qualitative model of flow induced crystallization. Shear first induces point-like nuclei. If shear is sustained for long enough, thread-like precursors can develop from these point-like nuclei at high enough shear stresses (close to the wall of the mold), and additional point-like nuclei may appear. If flow is sustained for a very long time, saturation of formation of threads may occur. After flow is stopped, the threads nucleate highly oriented lamellae that grow out radially.

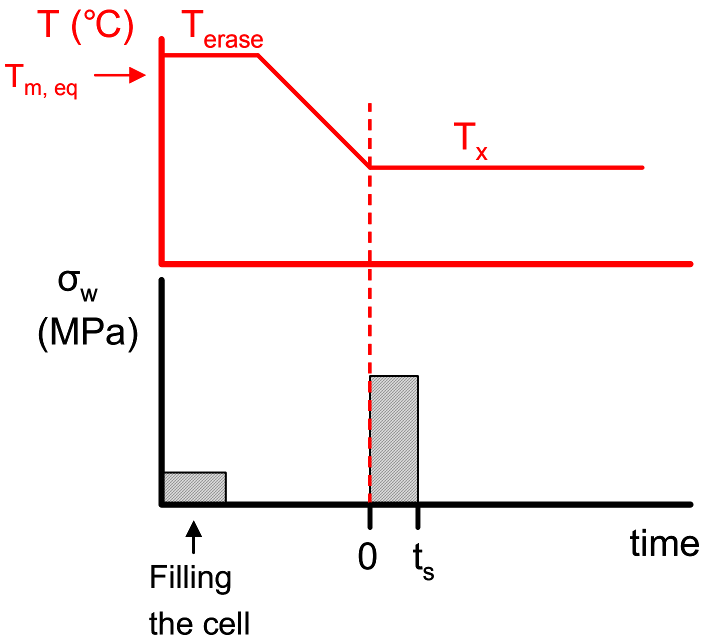

**Figure 2-2. Experimental protocol for flow-induced crystallization experiments**

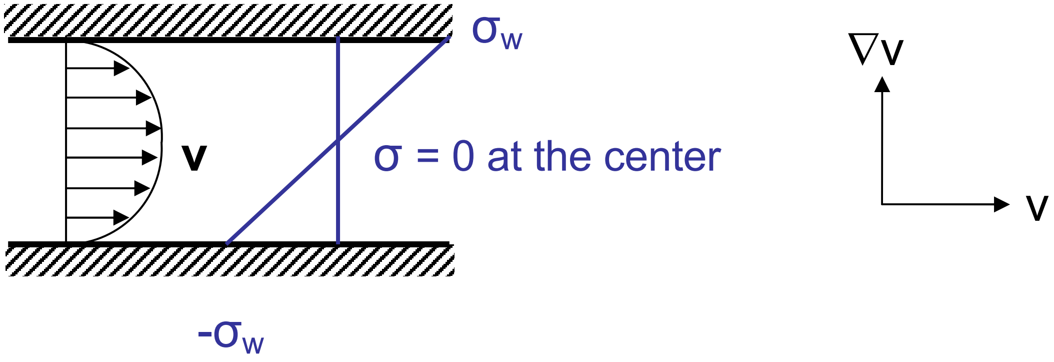

**Figure 2-3. Schematic showing flow profile and shear stress profile across the gap of the rectangular slit channel. The optical path is along the velocity gradient direction, denoted ∇v.**

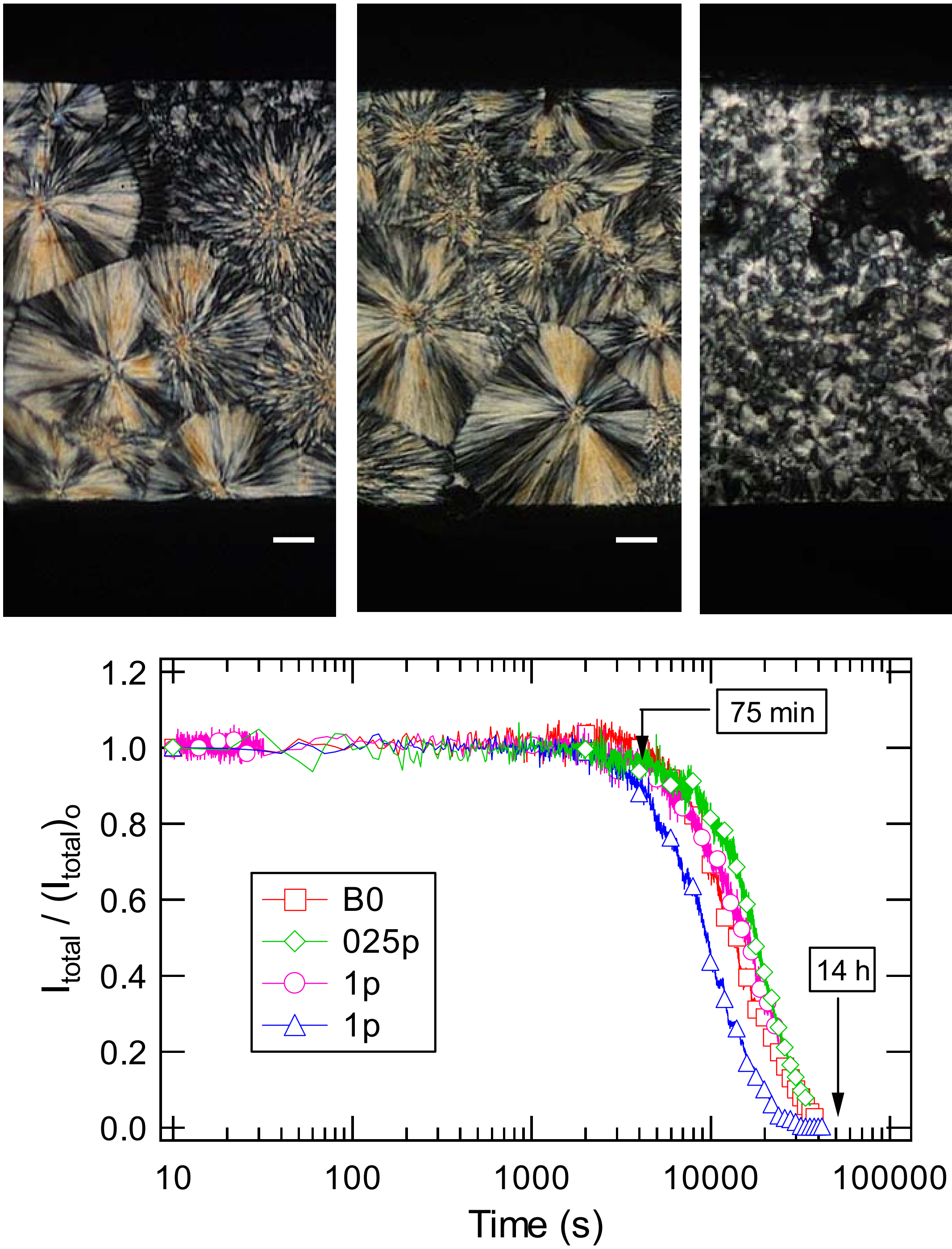

**Figure 2-4.** Top: Polarized optical micrographs of the ex-situ morphology after quiescent crystallization at 137˚C of: B0 cooled after 14 h (left micrograph); 1p quenched after 14 h (center); and 1p cooled after 75 min (right). Bottom: In-situ turbidity measurement during quiescent crystallization at 137˚C of B0, 025p, and 1p.

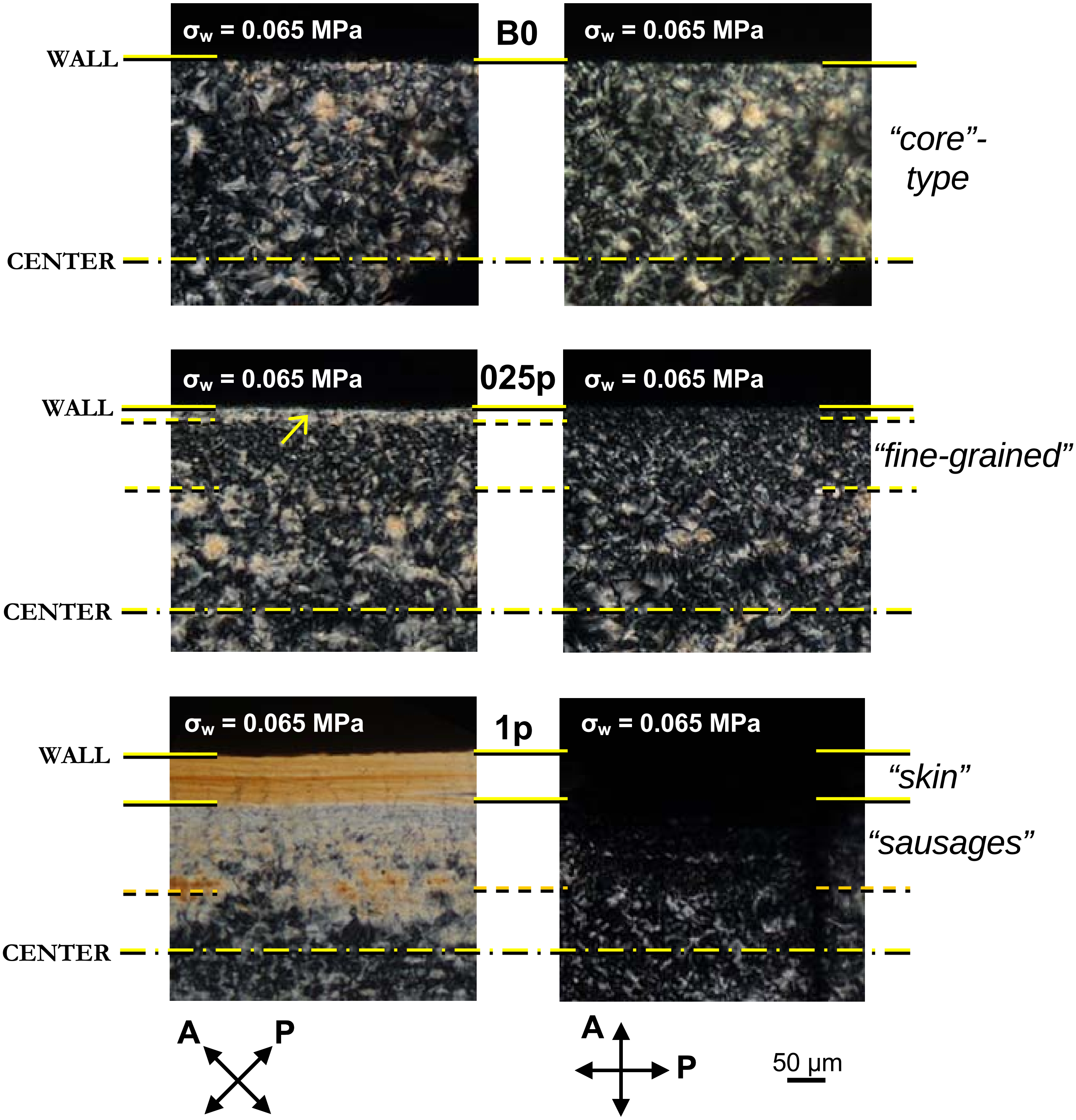

**Figure 2-5.** Ex-situ polarized optical micrographs of B0 (top), 0.25p (middle), and 1p (bottom) sheared at 137°C with wall shear stress $\sigma_w$ = 0.065 MPa and cooled after 75 minutes. The extruded amounts were ~ 100 mg ($t_s$ = 8.3 s, 8.7 s and 12 s for B0, 025p and 1p respectively). Flow direction is horizontal. Left column: Polarizer P is 45° to flow; right column: P is parallel to flow. The center to the wall of the sample corresponds to 250 μm.

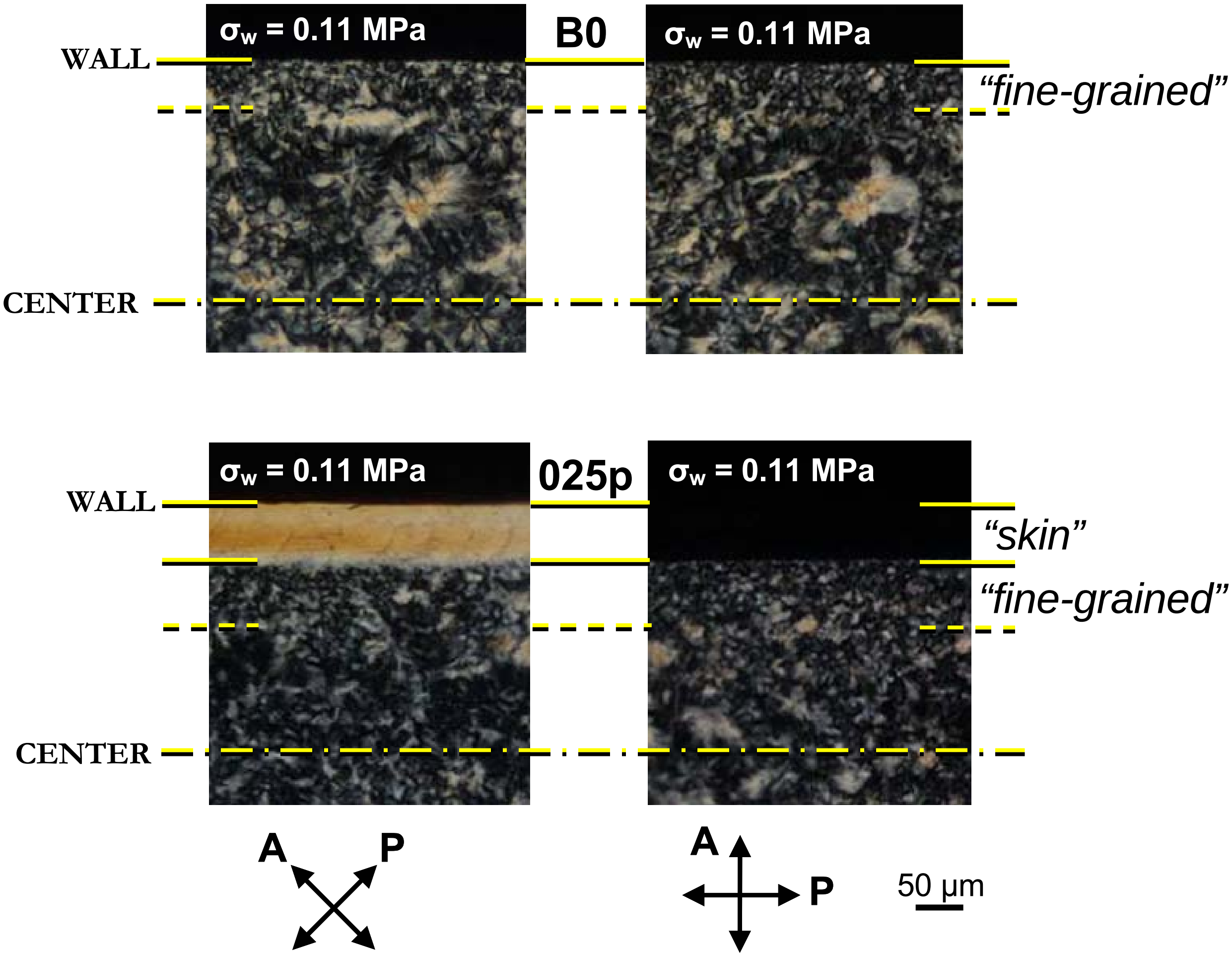

**Figure 2-6.** Ex-situ polarized optical micrographs for B0 (top) and 025p (bottom) crystallized at 137˚C for 75 min after imposing a pulse of $\sigma_w$ = 0.11 MPa. Extruded amounts were ~ 100 mg ($t_s$ = 1.4 s and 2.4 s for B0 and 025p, respectively).

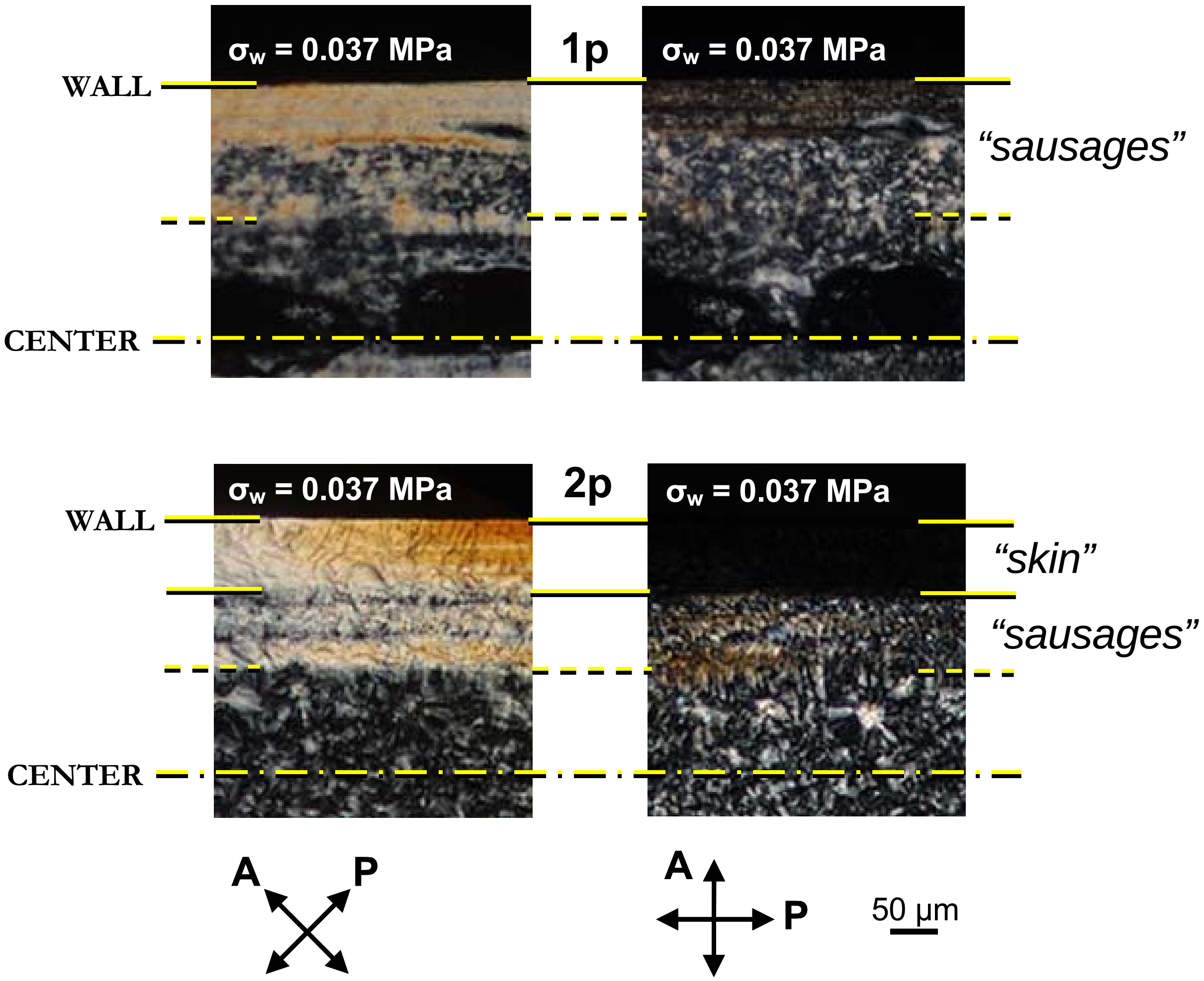

**Figure 2-7. Ex-situ polarized optical micrographs for 1p (top) and 2p (bottom) crystallized at 137˚C for 75 min after imposing a pulse of $\sigma_w$ = 0.037 MPa. Extruded amounts were ~ 100 mg ($t_s$ = 26 s and 27 s for 1p and 2p respectively).**

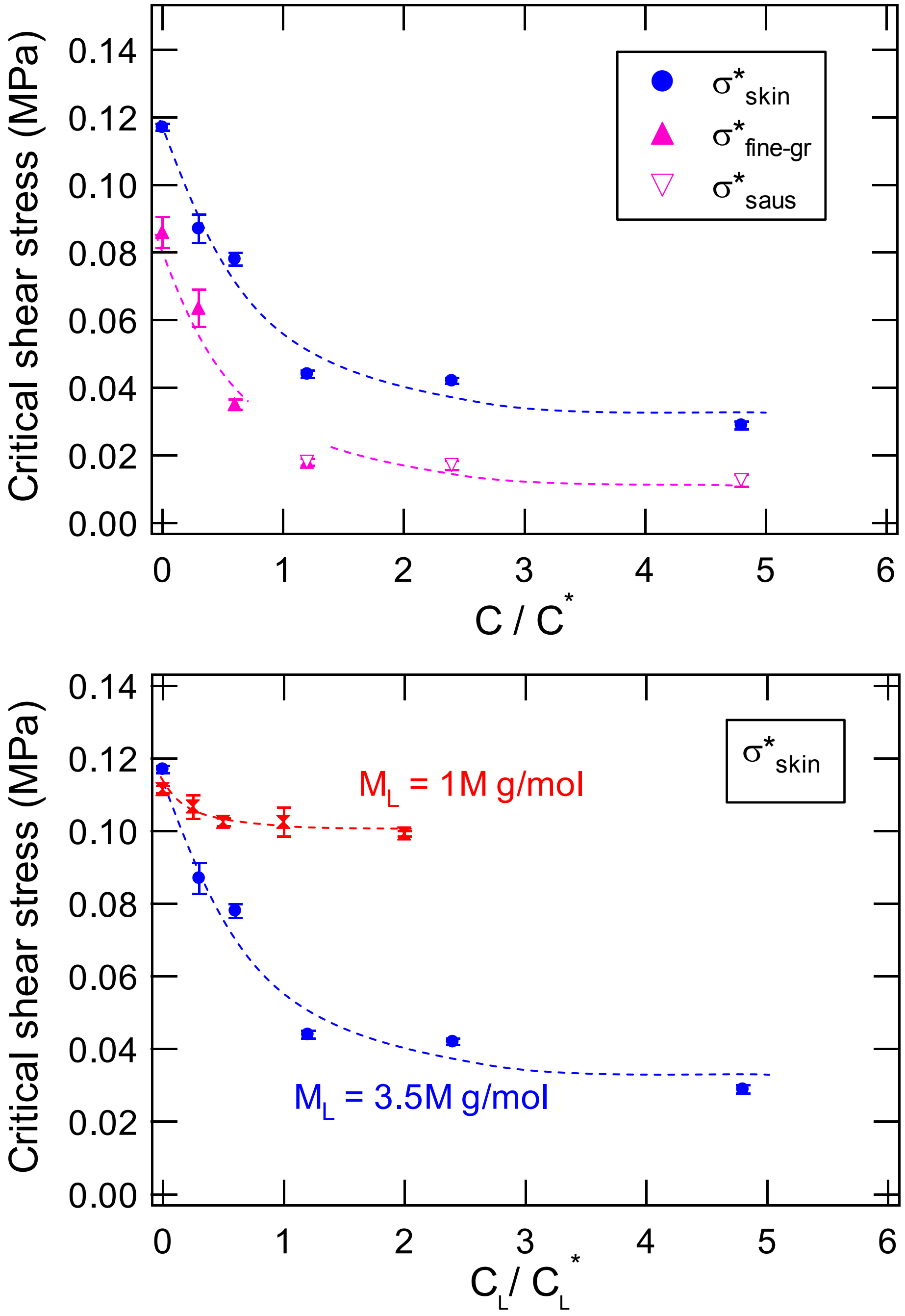

Figure 2-8. Top: effect of the concentration of 3500k long chains $C_L$ (relative to their overlap concentration $C_L^*$ ) on $\sigma^*_{skin}$ (for all $C_L$s), on $\sigma^*_{fine\text{-}gr}$ (for the smaller $C_L$s), and on $\sigma^*_{skin}$ (for the bigger $C_L$s) at 137°C and fixed total mass extruded. The dashed curves are for guiding the eye. Error bars refer to variations in the thicknesses of the skin, fine-grained, and sausage areas. Bottom: comparison of the impact of $M_w$ (either 1M from [7, 18] or 3.5M in the current study) of the long chains on $\sigma^*_{skin}$. $C_L^*$ is 0.0069 and 0.0036 g/cm$^3$ for 1M and 3.5M chains, respectively. The stresses reported in [7] were corrected according to [18].

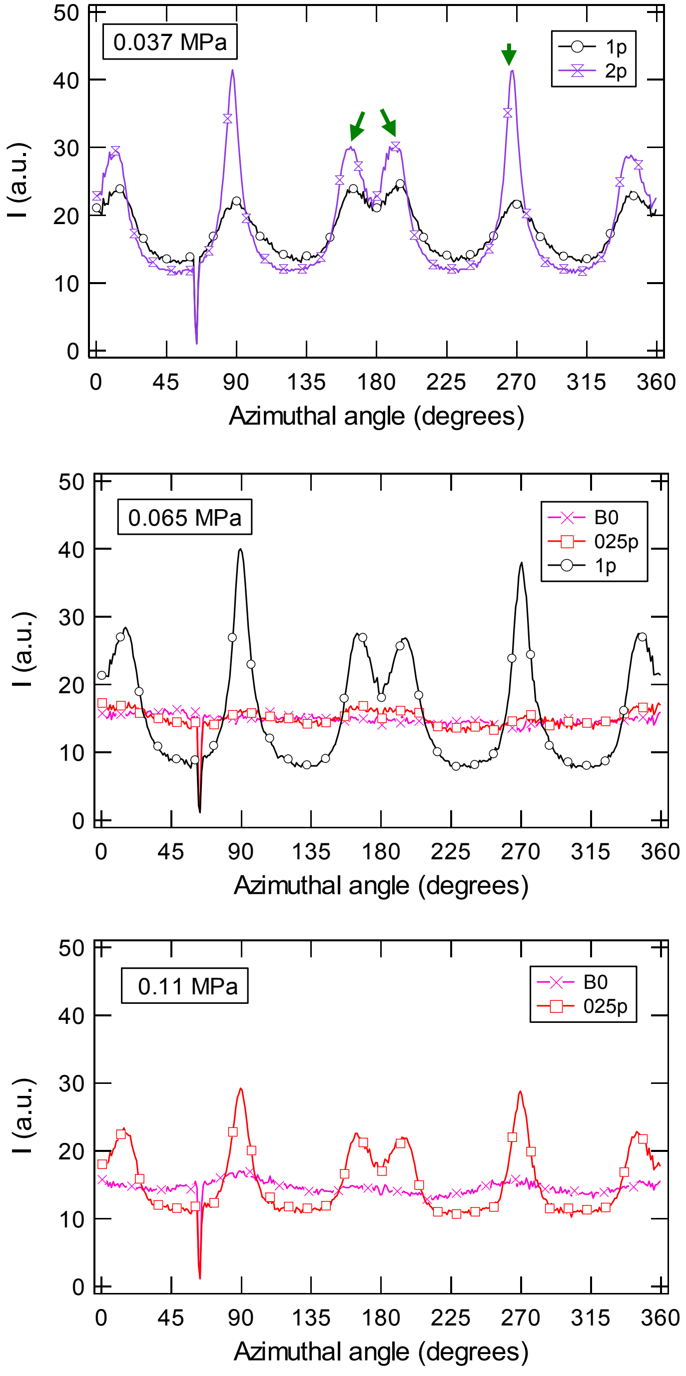

**Figure 2-9.** Ex-situ WAXD azimuthal distribution of the (110) reflection of α-iPP. Samples were sheared at 137˚C and $\sigma_w$ = 0.037 MPa (top), 0.065 MPa (center), and 0.11 MPa (bottom). They correspond to the POM shown in the previous figures: compare top to Figure 2-7, center to Figure 2-5, and bottom to Figure 2-6.

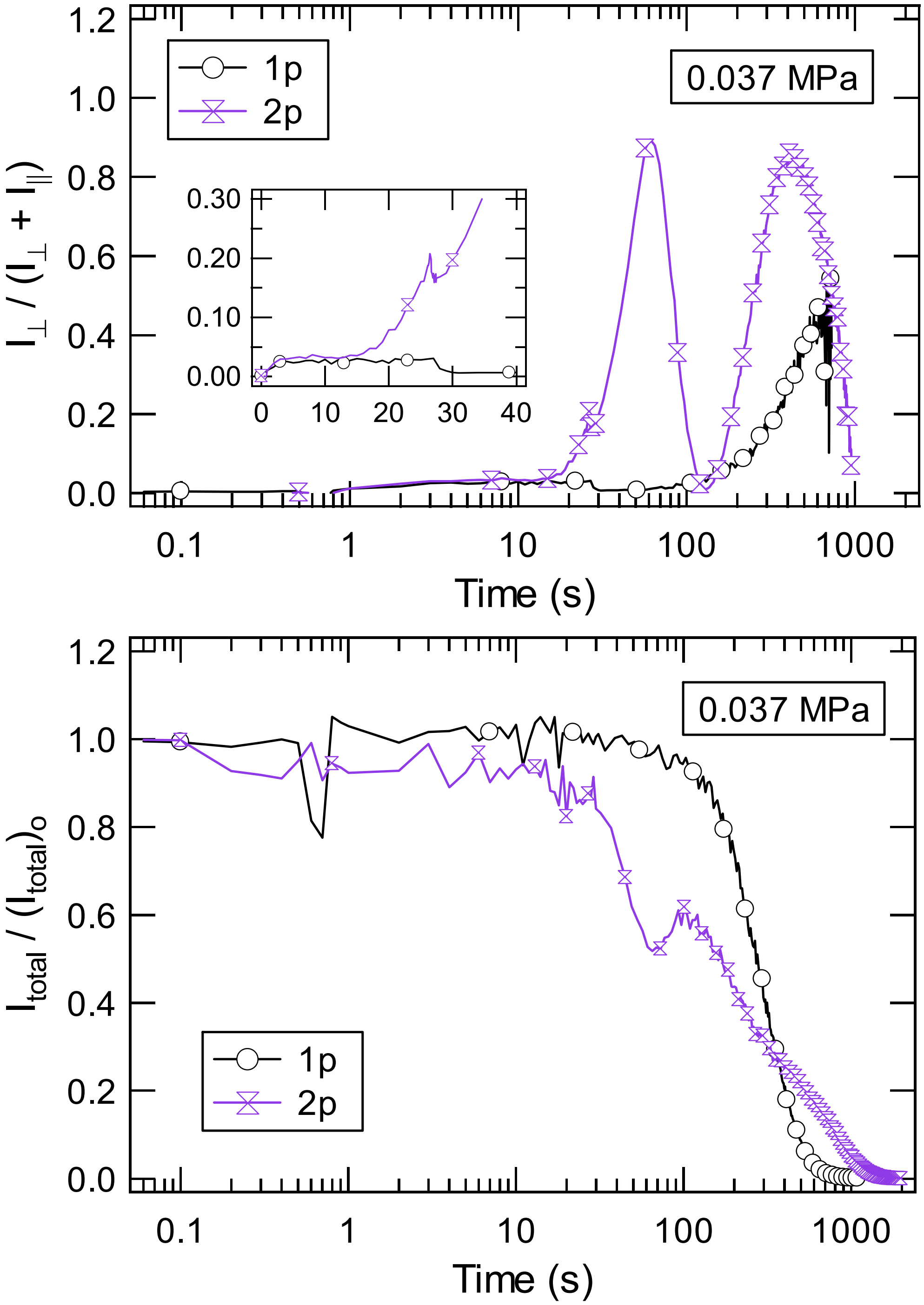

**Figure 2-10.** **Real-time optical polarimetry (top) and turbidity (bottom) measurements for 1p and 2p subjected to flow-induced crystallization at 137˚C and $\sigma_w$ = 0.037 MPa. Extruded mass was ~ 100 mg. The shearing times were 26 s and 27 s for 1p and 2p, respectively. Inset shows the details of upturn during earlier times, 0-40 s.**

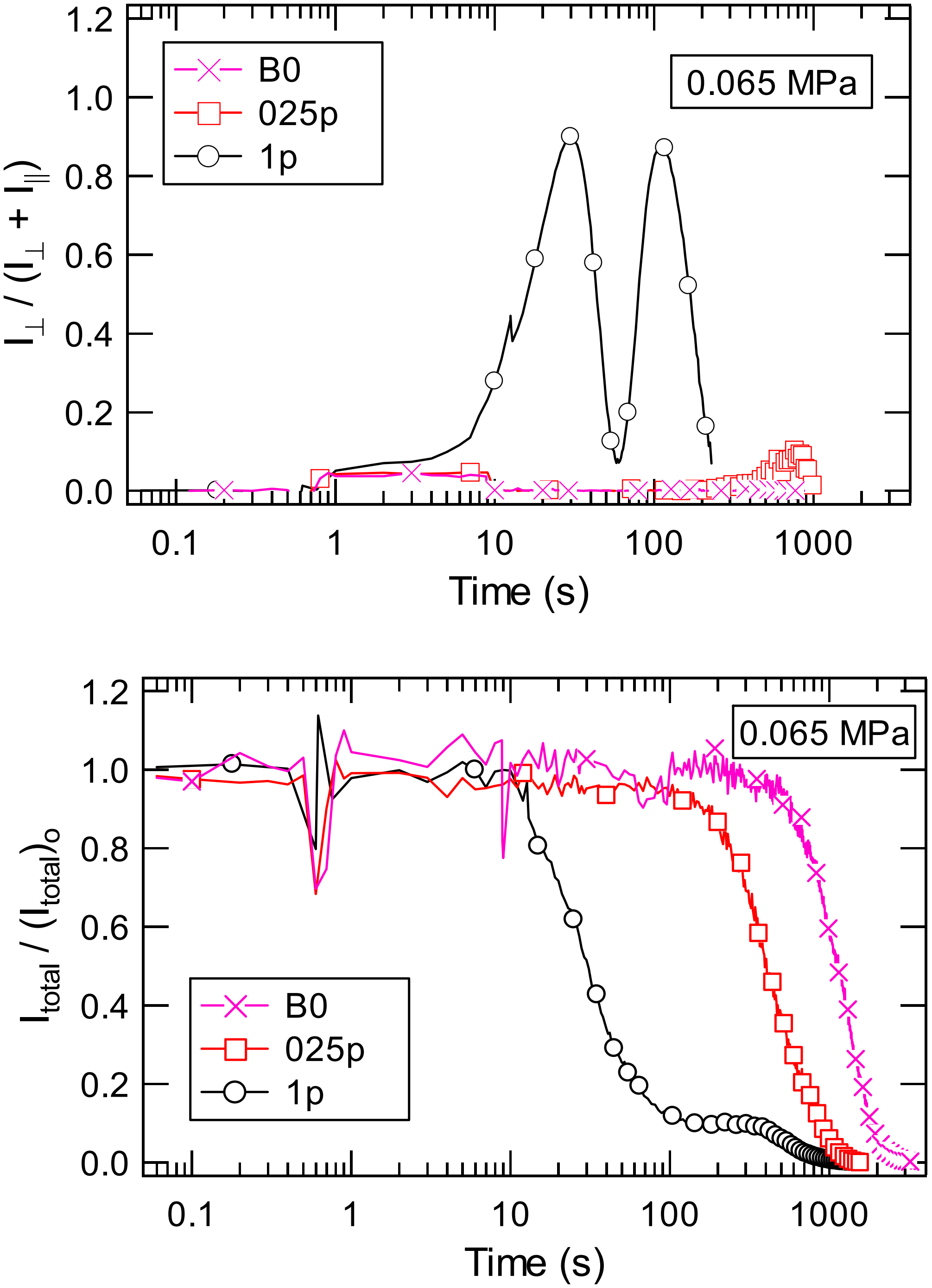

**Figure 2-11.** In-situ measurement of optical polarimetry (top) and turbidity (bottom) for 137˚C and a shear pulse of $\sigma_w$ = 0.065 MPa. The extruded amount was ~ 100 mg; $t_s$ = 8.3 s, 8.7 s, and 12 s for B0, 025p, and 1p respectively.

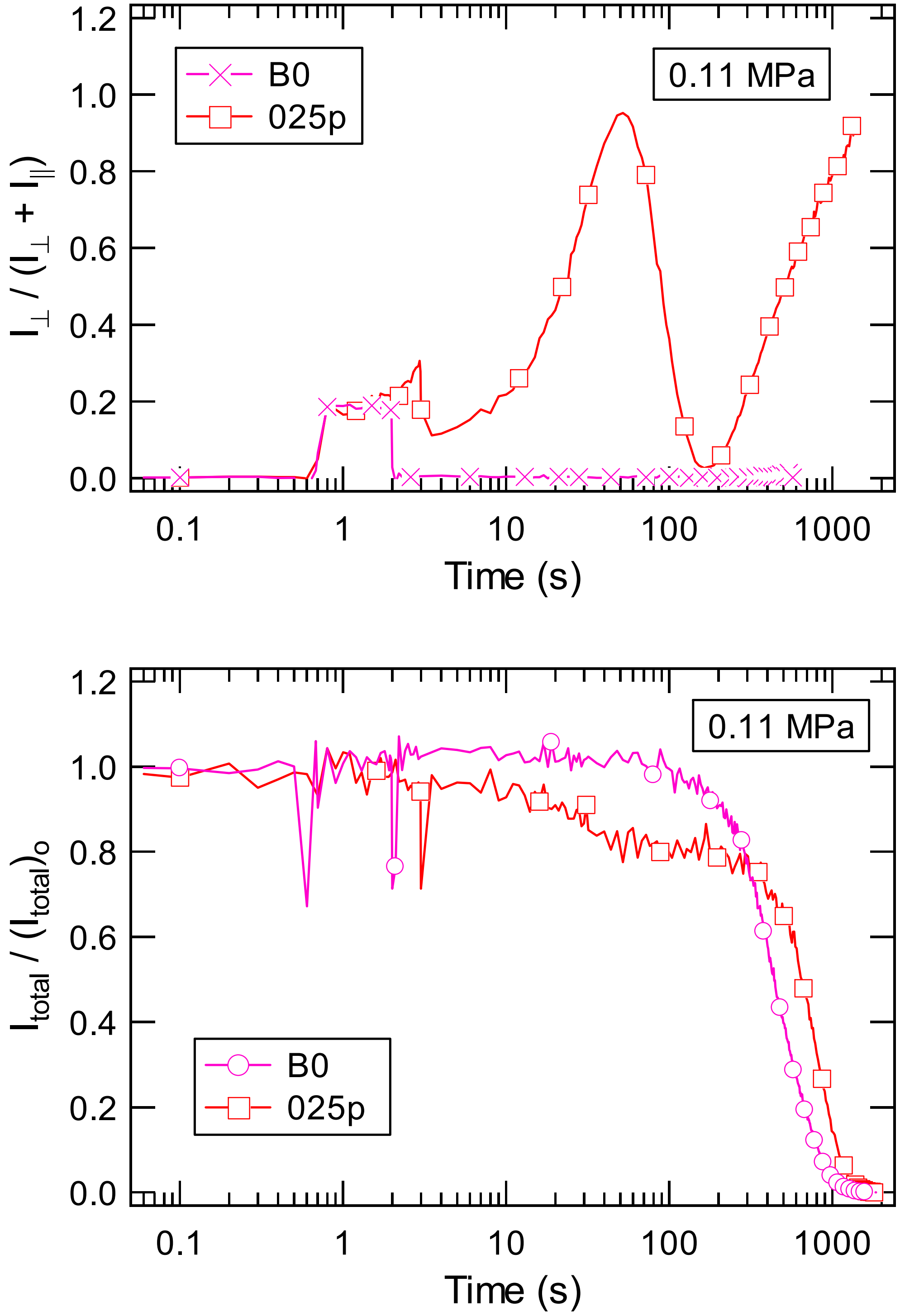

**Figure 2-12. Real-time birefringence (top) and turbidity (bottom) measurements at 137˚C, $\sigma_w$ = 0.11 MPa and ~ 100 mg extruded mass. The shearing times were 1.4 s and 2.4 s for B0 and 025p.**

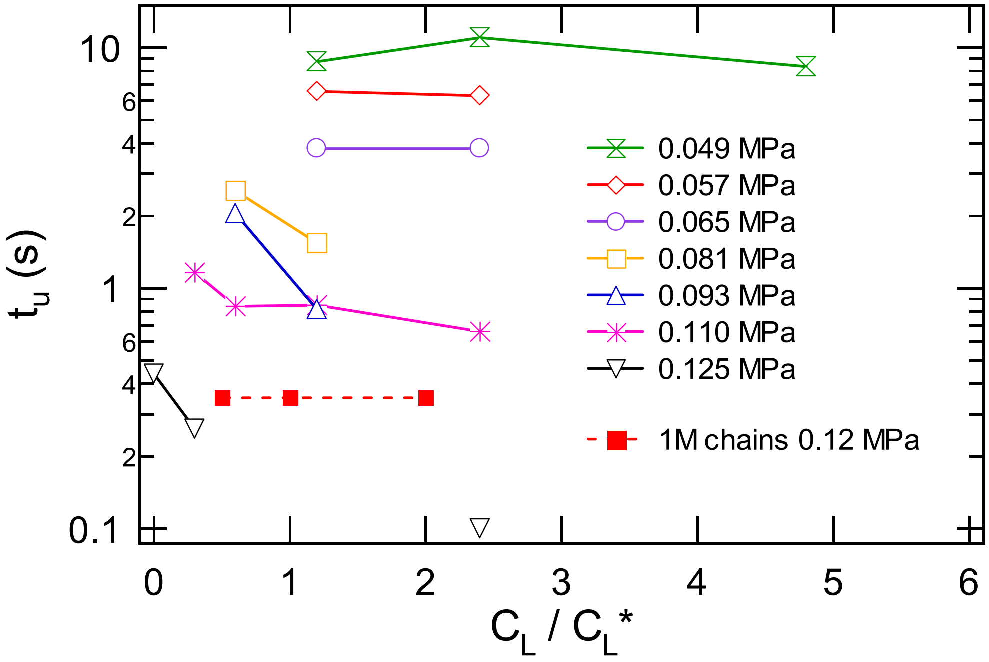

**Figure 2-13.** **Time for upturn ($t_u$) in birefringence signal during the shear pulse for different wall shear stresses and $C_L$s of 3.5M long chains. The data on 1M long chains and 0.12 MPa from [7] is also plotted.**

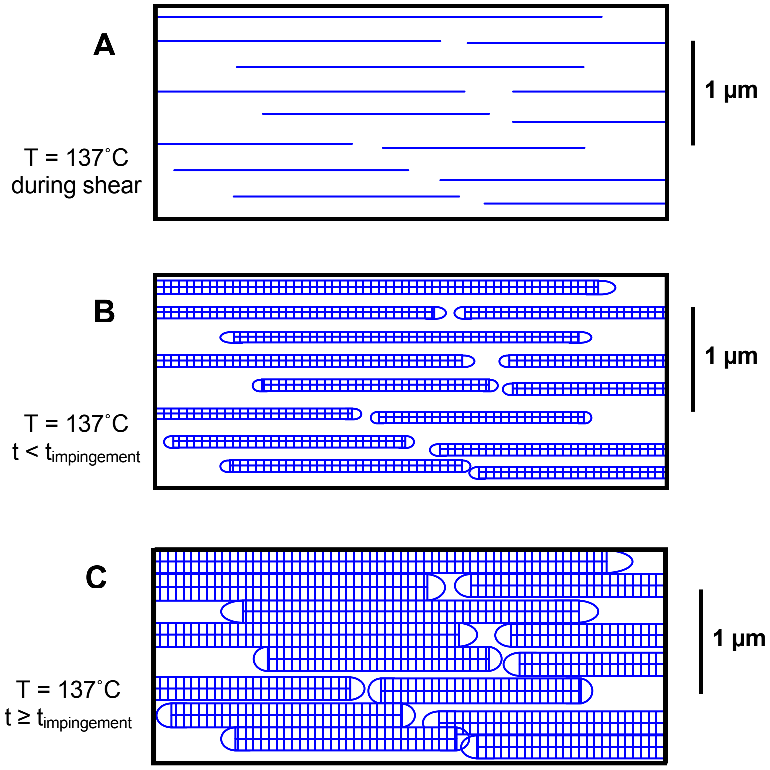

**Figure 2-14.** Schematic of formation and development of highly oriented skin during an isothermal flow-induced crystallization experiment. A) Large amount of long threads form during flow, giving rise to an upturn in birefringence. Some kebabs may already grow during flow (thus contributing to the upturn), but they are not drawn in this figure. B) After cessation of flow, oriented lamellae grow off the threads. C) Impingement occurs shortly after cessation of flow because of the small interspacings between the threads in the highly oriented skin.

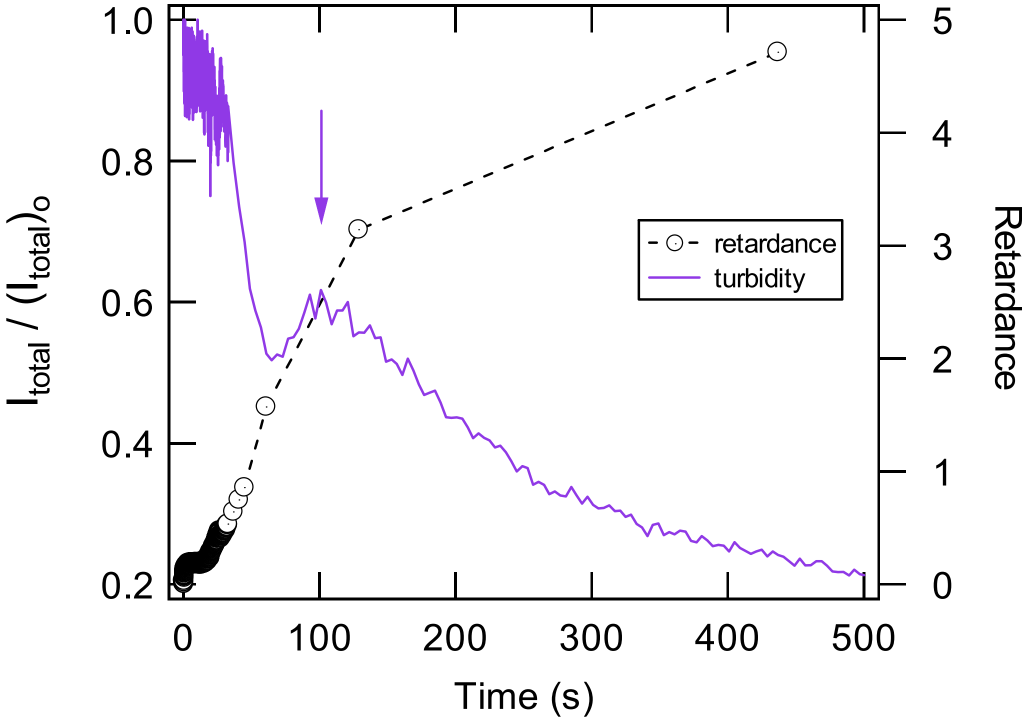

**Figure 2-15. Example of signatures of highly oriented skin impingement in retardance and turbidity signals. This experiments corresponds to 2p sample for $T_x$ = 137°C and $\sigma_w$ = 0.037 MPa.**

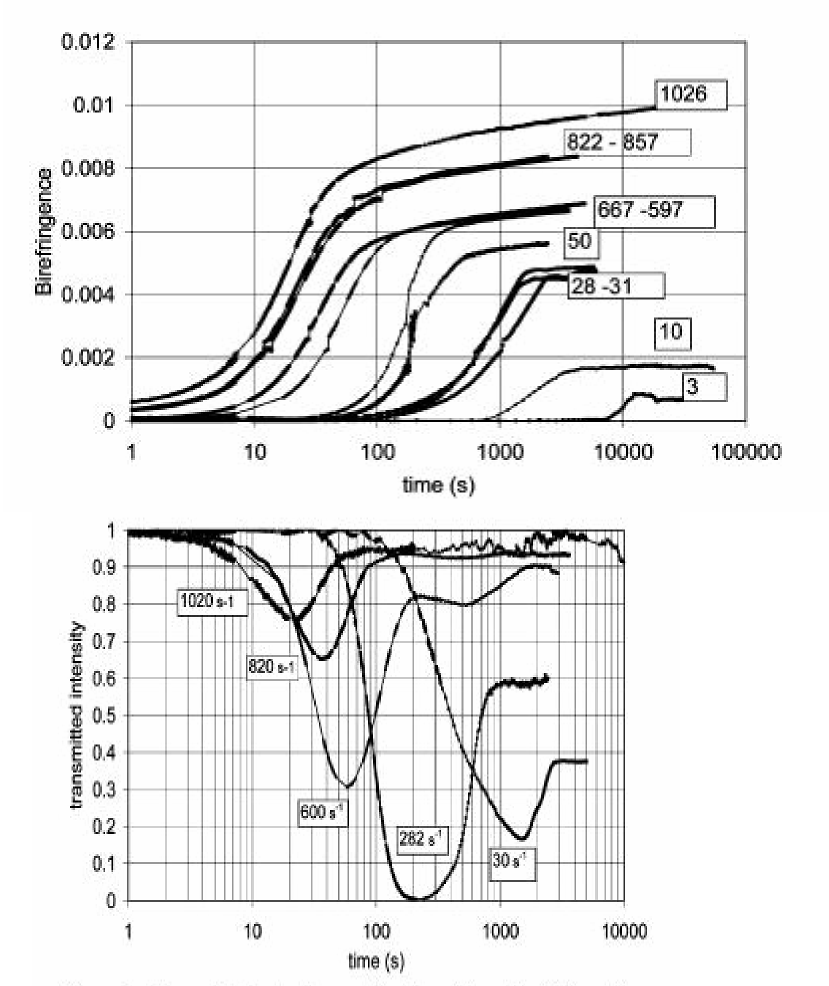

**Figure 2-16. Retardance and transmittance curves reprinted with permission from [19], Copyright 2006 American Chemical Society. The transmittance figure has been rescaled so that both time axes match. The correspondence between the retardance leveling off and the increase in transmittance can be well observed.**

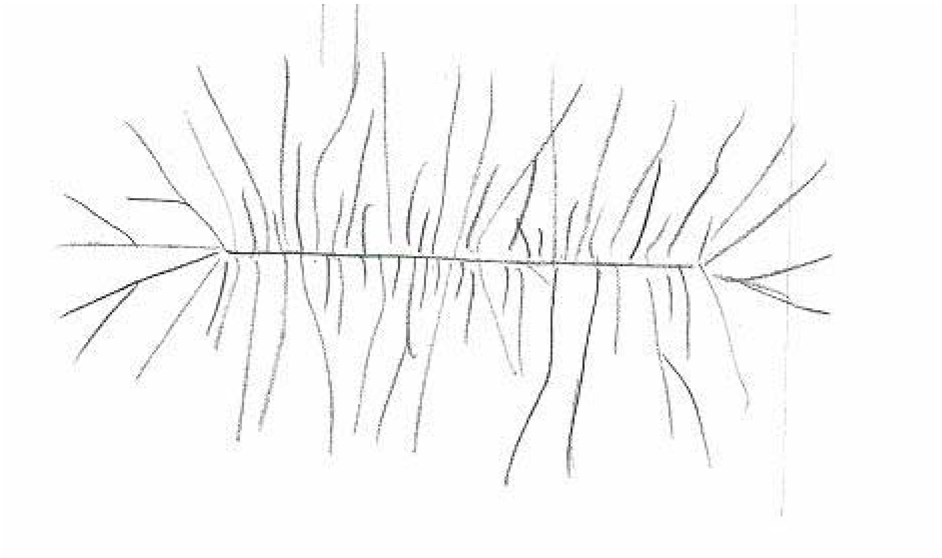

**Figure 2-17. Sausages grow to much larger diameters than kebabs in skin. There is more space at larger distances from the thread for non-crystallographic branching, so high degree of orientation is progressively lost.**

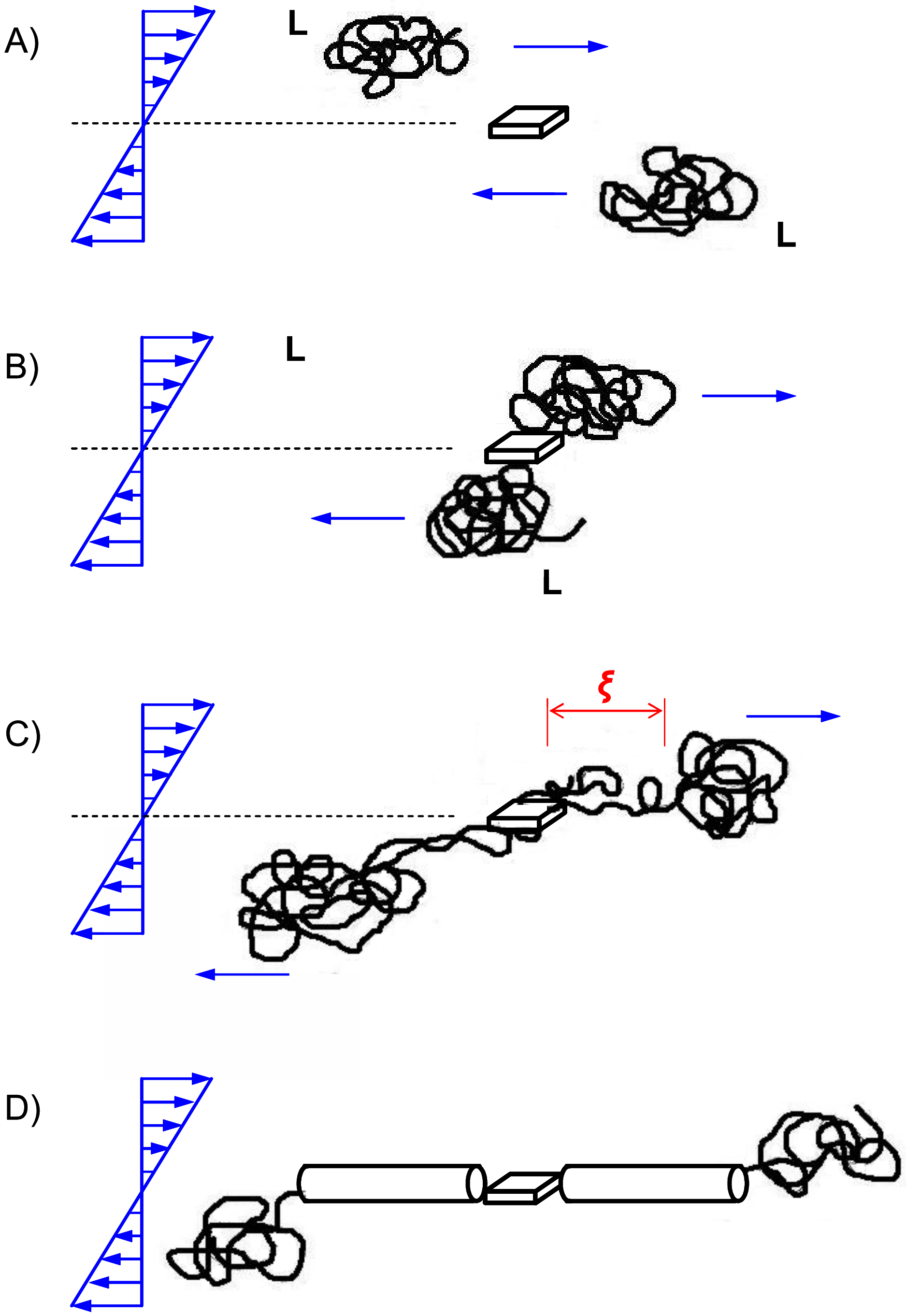

**Figure 2-18.** Kick-off stage in model for flow-induced formation of thread-like precursors

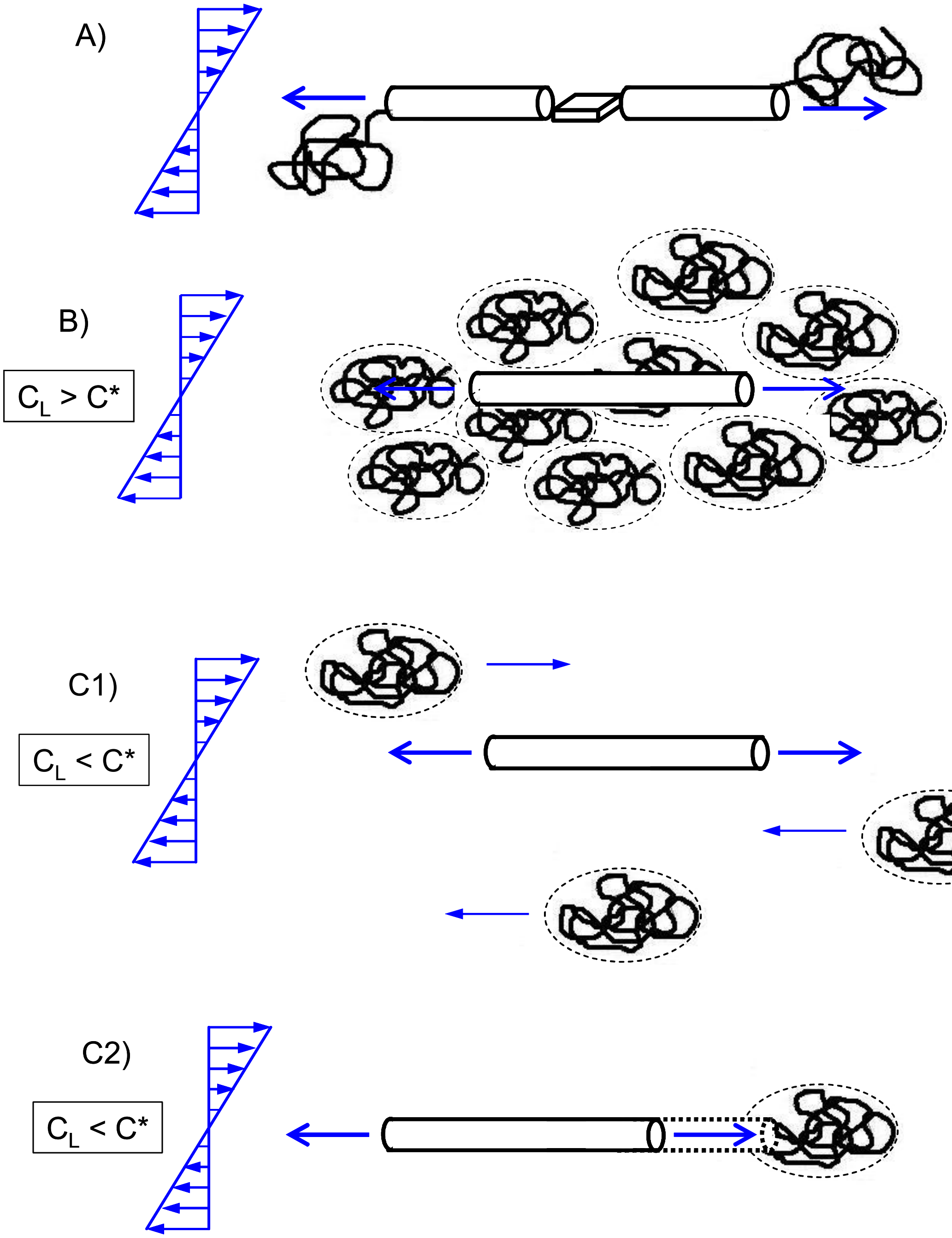

**Figure 2-19. Propagation stage: dependence on concentration of long chains**

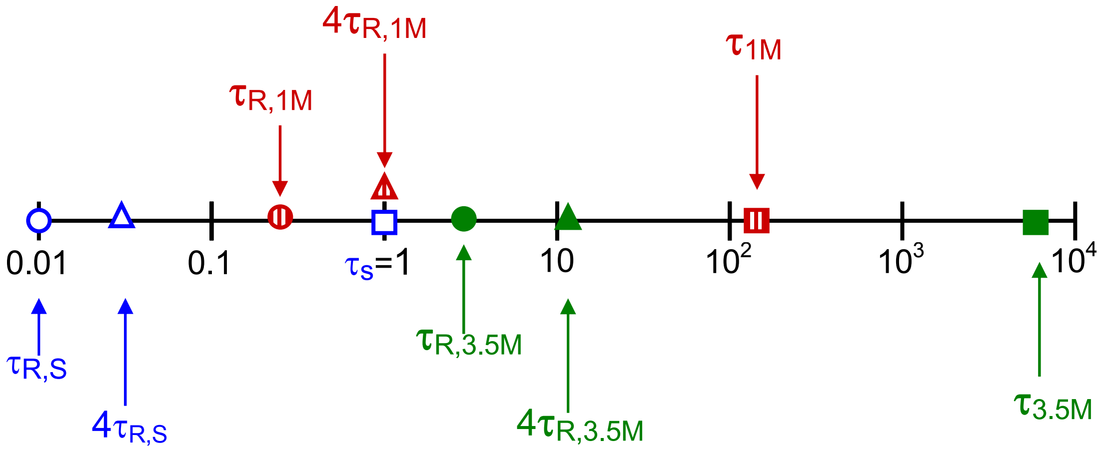

**Figure 2-20.** Retraction times for untethered and tethered short chain ($\tau_{R,S}$, $4\tau_{R,S}$), 1M long chains ($\tau_{R,1M}$, $4\tau_{R,1M}$), and 3.5M long chains ($\tau_{R,3.5M}$, $4\tau_{R,3.5M}$). Reptation times of 1M and 3.5M are also indicated ($\tau_{1M}$ and $\tau_{3.5M}$).

## 2.8 References

1. Liedauer, S., G. Eder, H. Janeschitzkriegl, et al. *On the Kinetics of Shear-Induced Crystallization in Polypropylene.* International Polymer Processing, 1993. **8**(3): 236-244.
2. Keller, A., and M.J. Machin. *Oriented Crystallization in Polymers.* Journal of Macromolecular Science, Part B, 1967(B1): 41.
3. Sherwood, C.H., F.P. Price, and R.S. Stein. *Effect of Shear on Crystallization Kinetics of Poly(Ethylene Oxide) and Poly(Epsilon-Caprolactone) Melts.* Journal of Polymer Science Part C-Polymer Symposium, 1977(63): 77-94.
4. Jerschow, P., and H. JaneschitzKriegl. *The role of long molecules and nucleating agents in shear induced crystallization of isotactic polypropylenes.* International Polymer Processing, 1997. **12**(1): 72-77.
5. Somani, R.H., B.S. Hsiao, A. Nogales, et al. *Structure development during shear flow-induced crystallization of i-PP: In-situ small-angle X-ray scattering study.* Macromolecules, 2000. **33**(25): 9385-9394.
6. Vleeshouwers, S., and H.E.H. Meijer. *A rheological study of shear induced crystallization.* Rheologica Acta, 1996. **35**(5): 391-399.
7. Seki, M., D.W. Thurman, J.P. Oberhauser, et al. *Shear-mediated crystallization of isotactic polypropylene: The role of long chain-long chain overlap.* Macromolecules, 2002. **35**(7): 2583-2594.
8. Kumaraswamy, G., R.K. Verma, and J.A. Kornfield. *Novel flow apparatus for investigating shear-enhanced crystallization and structure development in*

*semicrystalline polymers.* Review of Scientific Instruments, 1999. **70**(4): 2097-2104.

9. de Gennes, P.G., *Scaling Concepts in Polymer Physics*. 1979, Ithaca, N.Y.: Cornell University Press.
10. Takahashi, Y., Y. Isono, I. Noda, et al. *Zero-Shear Viscosity of Linear Polymer-Solutions over a Wide- Range of Concentration.* Macromolecules, 1985. **18**(5): 1002-1008.
11. Ballard, D.G.H., P. Cheshire, G.W. Longman, et al. *Small-Angle Neutron-Scattering Studies of Isotropic Polypropylene.* Polymer, 1978. **19**(4): 379-385.
12. Kumaraswamy, G., J.A. Kornfield, F.J. Yeh, et al. *Shear-enhanced crystallization in isotactic polypropylene. 3. Evidence for a kinetic pathway to nucleation.* Macromolecules, 2002. **35**(5): 1762-1769.
13. Spherulites consiste of lamellae that grow and splay out from the center. There is intrinsic anisotropy within a spherulite (which explaines why under crossed polarizers they reveal Maltese-cross type patterns, and not a completely dark image). However, it is at larger scales that themselves they can be considered "macroscopically isotropic". For instance, on average, they would not induce measurable retardation on a transmited optical beam.
14. Isayev, A.I., T.W. Chan, K. Shimojo, et al. *Injection-Molding of Semicrystalline Polymers .1. Material Characterization.* Journal of Applied Polymer Science, 1995. **55**(5): 807-819.
15. Fujiyama, M., T. Wakino, and Y. Kawasaki. *Structure of Skin Layer in Injection-Molded Polypropylene.* Journal of Applied Polymer Science, 1988. **35**(1): 29-49.

16. Fitchmun, D.R., and Z. Mencik. *Morphology of Injection-Molded Polypropylene.* Journal of Polymer Science Part B-Polymer Physics, 1973. **11**(5): 951-971.

17. Kantz, M.R., F.H. Stigale, and H.D. Newman. *Skin-Core Morphology and Structure-Property Relationships in Injection-Molded Polypropylene.* Journal of Applied Polymer Science, 1972. **16**(5): 1249-&.

18. Thurman, D.W., *Molecular Aspects of Flow-Induced Crystallization of Polypropylene*. 2005, California Institute of Technology.

19. Langouche, F. *Orientation development during shear flow-induced crystallization of i-PP.* Macromolecules, 2006. **39**(7): 2568-2573.

20. Kumaraswamy, G., A.M. Issaian, and J.A. Kornfield. *Shear-enhanced crystallization in isotactic polypropylene. 1. Correspondence between in situ rheo-optics and ex situ structure determination.* Macromolecules, 1999. **32**(22): 7537-7547.

21. Kumaraswamy, G., R.K. Verma, A.M. Issaian, et al. *Shear-enhanced crystallization in isotactic polypropylene Part 2. Analysis of the formation of the oriented "skin".* Polymer, 2000. **41**(25): 8931-8940.

22. White, H.M., and D.C. Bassett. *On variable nucleation geometry and segregation in isotactic polypropylene.* Polymer, 1997. **38**(22): 5515-5520.

23. Spruiell, J.E., F.M. Lu, Z. Ding, et al. *The influence of isotacticity, ethylene comonomer content, and nucleating agent additions on the structure and properties of melt-spun isotactic polypropylene filaments.* Journal of Applied Polymer Science, 1996. **62**(11): 1965-1975.

24. Jerschow, P., and H. JaneschitzKriegl. *On the development of oblong particles as precursors for polymer crystallization from shear flow: Origin of the so-called fine grained layers.* Rheologica Acta, 1996. **35**(2): 127-133.

25. Lotz, B., J.C. Wittmann, and A.J. Lovinger. *Structure and morphology of poly(propylenes): A molecular analysis.* Polymer, 1996. **37**(22): 4979-4992.

26. Janimak, J.J., S.Z.D. Cheng, P.A. Giusti, et al. *Isotacticity Effect on Crystallization and Melting in Poly(Propylene) Fractions .2. Linear Crystal-Growth Rate and Morphology Study.* Macromolecules, 1991. **24**(9): 2253-2260.

27. van Meerveld, J., G.W.M. Peters, and M. Hutter. *Towards a rheological classification of flow induced crystallization experiments of polymer melts.* Rheologica Acta, 2004. **44**(2): 119-134.

28. Doi, M., and S.F. Edwards, *The Theory of Polymer Dynamics*. 1986, New York: Oxford University Press.

29. Janeschitz-Kriegl, H., E. Ratajski, and M. Stadlbauer. *Flow as an effective promotor of nucleation in polymer melts: A quantitative evaluation.* Rheologica Acta, 2003. **42**(4): 355-364.

30. Janeschitz-Kriegl, H., E. Ratajski, and H. Wippel. *The physics of athermal nuclei in polymer crystallization.* Colloid and Polymer Science, 1999. **277**(2-3): 217-226.

## *Chapter III*

# *Real-Time Depth Sectioning Method: Isolating the Effect of Stress*

## 3.1 Introduction

Thread-like precursors are at the heart of flow-induced crystallization, as they are responsible for the dramatic changes in kinetics of crystallization and in the final morphology obtained. The creation of these precursors is highly dependent on stress, as illustrated in the schematic model depicted in Figure 2-1 (Chapter II), which is based on the model put forward by Janeschitz-Kriegl and coworkers [1].

In this model, point-like nuclei will form in the regions of higher stress (close to the walls of the mold) due to the shear imposed on the melt. With prolonged shear, thread-like precursors can grow from these point-like nuclei but only in the regions where the shearing stress is above a certain critical level. These threads continue to grow in length during flow, increasing the length thread/volume (the density of threads). If shear is sustained for a long enough time, there can be a saturation of this effect, which is perhaps due to impingement of the growing threads.

After flow has stopped, each of the oriented precursors nucleates highly oriented lamellae, which grow radially at the quiescent crystallization linear growth rate until they impinge with the oriented lamellae growing from neighboring threads. The presence of the oriented threads signifies a dramatic increase in the nucleation surface when compared to quiescent crystallization. This explains the observed increase in the kinetics of crystallization by orders of magnitude when compared with the kinetics under quiescent conditions [2, 3]. Also, if the oriented precursors are quite close to each other, the growing oriented lamellae do not have much space to diverge, and the final morphology will show a very high degree of orientation in the crystallites. Because thread-like precursors are key elements in the big effects that flow can have on kinetics and morphology of crystallization, there is great interest in investigating how their creation depends on stress, temperature, and characteristics of the resin. However, it is very difficult to detect the bare thread-like precursors (when no kebabs have grown on them), and therefore quantifying the number and length of threads remains a challenge. The kinetics of crystallization and morphology are extremely sensitive to the presence of these oriented precursors, which opens up the way for quantifying them in an indirectly by "reading" out their effects.

Our flow-induced crystallization apparatus [4] uses the short-term shearing protocol developed by Janeschitz-Kriegl [1, 5-7]: After a brief and intense shear pulse on the polymer melt, we monitor the real-time development of crystallization with a variety of in-situ probes. This instrument produces a pressure driven flow through a slit channel and allows us to control the shear stress imposed on the wall of the channel. The flow and temperature histories are well defined, and because stress is the controlled variable, the average stress can be maintained similar for resins in which a small amount of long chains is introduced. However, it is essential to realize that the optical and X-ray probes for real-time measurements traverse the width of this channel (Figure 3-1). Therefore, they survey the progress of crystallization all throughout the depth of the channel, so the outgoing signal corresponds to the average of shear stresses between the wall shear stress ($\sigma_w$) and the center of the channel (where the stress is zero).

We have developed the depth sectioning method as a strategy to isolate the contribution to the real-time signal that arises from a given depth of the flow channel (i.e., a certain level of shear stress). This method is important, as the formation of thread-like precursors (and thus the kinetics and structure) are strongly dependent on stress. Our flow cell allows us to extract the sample for ex-situ observation of the final morphology; however, we cannot extract information about the development of thread length per volume during flow, as this can only be determined from the kinetics of growth of the oriented crystallites. It is also possible to observe certain type of ex-situ structure that has been formed from different thread-densities (i.e., different kinetics of crystallization). Therefore, the depth sectioning method is a promising approach for investigating the formation of thread-like precursors as a function of stress, shearing time, temperature, and molecular variables.

## 3.2 Depth sectioning method

The depth sectioning method is based on the fact that for a pressure driven flow throughout a slit channel, the stress profile varies linearly from a given shear stress at the wall ($\sigma_w$) to zero at the center of the channel (Figure 3-1). This linear profile arises directly from the force balance for a rectangular duct, and therefore it is independent of what the material is (e.g., solid vs. liquid) or how it is deforming (e.g., flowing vs. static vs. slipping). Therefore, we can rigorously calculate the stress $\sigma_{xy}$ imposed on a material point located at a certain distance y from the mold wall if the wall shear stress is known.

The robust relationship between distance y from the wall and its corresponding shear stress $\sigma_{xy}$ allows us to isolate the contribution from a given slice of material (i.e. from a region of a certain range of shear stress) if we use a set of several experiments for which different wall shear stresses have been applied, but that have been performed under identical conditions of crystallization temperature ($T_x$) and shearing time ($t_s$). The top row of Figure 3-2 illustrates the final ex-situ polarized optical micrographs for a set of four different flow-induced experiments in which subsequently lower wall shear stresses $\sigma_w$ were imposed, while holding $t_s$ and $T_x$ constant. The plane of observation in these micrographs corresponds to the flow-velocity gradient xy. The corresponding in-situ measurements were obtained with a beam that traversed each specimen from top to bottom (dashed arrow). Therefore, the real-time signal that was obtained for each experiment corresponded to the average throughout the depth of each sample.

The far left micrograph in the top row of Figure 3-2 corresponds to the first experiment, performed at the highest wall shear stress ($\sigma_{w,1}$ = 65 kPa). The second experiment was performed at a wall shear stress slightly lower ($\sigma_{w,2}$ = 58 kPa), and due to the direct correlation between depth and stress, we can identify this second experiment as equivalent to an inner portion of the first experiment. If we subtract from an appropriate, real-time observable of the first experiment the real-time observable corresponding to the second experiment (rescaled to account for the difference in path length), the resulting real-time observable will correspond to the contribution from only the outermost slice of material in the first experiment (i.e., to the range of stress between 65 kPa and 58 kPa). This scheme can be repeated by performing experiments at successively lower wall shear stresses, thus enabling the isolation the signal arising from slices at different depths (i.e., different ranges of shear stress) for each point in time.

In our rheo-optical and rheo X-ray experiments, the probe beam is transmitted through the entire range of structures from those near the wall to those at the center. The real-time WAXD patterns that match the optical micrographs after substantial crystallization has occurred (30 minutes after cessation of shear) are shown in Figure 3-2, middle row. As will be discussed in the next sections, the contribution of each differential layer of sample to the overall diffraction pattern is additive. Therefore, the difference between the rescaled scattering patterns of successively lower wall shear stress experiments (bottom of Figure 3-2) isolates the structure formation in the layers corresponding to ($\sigma_i$—$\sigma_{i+1}$). This reasoning holds at each moment in time, during and after shear, provided the sample, the shearing time, and the temperature are all held constant for all experiments. After the observable corresponding to a given depth slice is calculated, it must be normalized by the thickness of the depth section, so that an average quantity is extracted and the results obtained from depth slices of different thicknesses can be compared.

The successful application of the depth sectioning method inherently involves some assumptions: 1) local response of flow-induced crystallization phenomena, and 2) additive contribution of each slice to our observable. For our flow-induced experiments, these conditions typically hold. In the following, we first look at the local character of flow-induced crystallization, and then we treat the interaction of the real-time probe beams with the sample to discuss the additivity of each observable .

### 3.2.1 Flow-induced crystallization as a local phenomenon

Previous studies have shown that flow-induced crystallization is a local phenomenon that does not depend on how far away the mold wall is situated, but on the specific flow conditions at a given point in the material. Nucleation on the wall surface is found to be negligible [8] and the formation of flow-induced nuclei effectively screens the material in the interior from any influence of the wall. The length scale of communication of nucleation in one region with growth at a distance from it is set by the distance between nucleation sites. For regions that correspond to high nucleation density of thread-like precursors, these row-nucleated morphologies have been observed to vary between 250 and 750 nm [3, 9]. These length scales are much smaller than the thinnest depth section thickness we used (~ 23 μm).

Since structure development is local, the stress level determines the nucleation density and morphology. If $(\partial\sigma_{xy}/\partial y)$ is shallower, then a thicker differential layer has the structure for $\sigma_o \pm \delta\sigma$ than in the case of a steeper gradient, and rescaling can be used to account for it. This applies if, as in our case, the increments used are much larger than the maximum length scale observed in the experiments.

### 3.2.2 Additive contributions to optical and X-ray observables

Due to symmetry and limited to the regime of single scattering, the key observables used to characterize flow-induced crystallization can be analyzed as the sum of contributions from each depth in the sample. To understand the regime of validity of this procedure, consider first the polarimetric observable (retardance) and then the scattered intensity in the case of SAXS and WAXD.

#### 3.2.2.1 Retardance

As polarized light passes through a polymer melt in which crystallization is beginning, it is altered by the anisotropic retardance (including intrinsic and form birefringence) and by scattering due to structures that can have anisotropic shape and optical properties, which result in anisotropic attenuation (dichroism). In the present experiments, light propagates through a material with optical properties that vary with position. Therefore, it is useful to approximate the system as a succession of optical elements with different birefringence and dichroism.

The present rheo-optical measurements use light propagating in y direction (Figure 3-1); the polarization state (the $E_x$ and $E_z$ components of the electric vector and the relative phase angle between these two components) is altered as it propagates through the material. Here we consider linear transformations, so matrix operations can be conveniently used for describing the effect of the optical elements on the incoming light.

**Jones matrix.** The polarization properties of light can be represented by the Jones vector **A** [10], which is a two-component vector that describes the x and y components of the electric vector of light propagating along the z axis. The incident light will be represented by $\mathbf{A_o}$, and the exiting light will have properties $\mathbf{A_1}$ after its transmission through a particular optical element. Jones calculus accounts for each optical element i by a Jones matrix $\mathbf{J_i}$ that describes the change in the intensity and polarization state of light due to the i$^{th}$ element with respect to a given orthonormal basis set of directions. Then, matrix operations can conveniently describe this transformation. For a single optical element:

$$\mathbf{A_1} = \mathbf{J} \cdot \mathbf{A_0} \ .$$

**Coaxial birefringent and dichroic elements.** We consider two types of optical elements that we may have to be considered in our crystallizing polymer: anisotropic retarder (birefringence) and anisotropic attenuator (dichroism). A birefringent and dichroic medium changes the phase and amplitude of the electric vector differently for its two orthogonal components. Such an optical element has a complex refractive index tensor **n = n' + in" [10].** In shear flow with velocity along x, gradient of velocity along y and vorticity along z (Figure 3-1), by symmetry $n_{xz} = n_{xy} = 0$:

$$\mathbf{n} = \begin{bmatrix} n_{xx} & n_{xy} & 0 \\ n_{xy} & n_{yy} & 0 \\ 0 & 0 & n_{zz} \end{bmatrix} \ .$$

If light propagates through it along the y axis, it is affected by both the linear birefringence in the xz plane ($\Delta n' = n'_{zz} - n'_{xx}$) and by the linear dichroism in the xz plane ($\Delta n'' = n''_{zz} - n''_{xx}$). For the case of shear and for light propagating in the y-direction, the principal axis for dichroism and birefringence are coaxial, so we can describe the Jones matrix for such an element of thickness *d* as:

$$\mathbf{J} = \begin{bmatrix} e^{i\frac{2\pi n_{xx} d}{\lambda}} & 0 \\ 0 & e^{i\frac{2\pi n_{zz} d}{\lambda}} \end{bmatrix} = e^{i\frac{2\pi n_{xx} d}{\lambda}} \cdot \begin{bmatrix} 1 & 0 \\ 0 & e^{-i\delta} \end{bmatrix}$$

where $\delta = \delta' + i\,\delta''$, $\delta'$ being the retardance:

$$\delta' = \frac{2\pi \Delta n' d}{\lambda}$$

and $\delta''$ being the extinction:

$$\delta'' = \frac{2\pi \Delta n'' d}{\lambda} \quad .$$

Note that retardance and extinction change the phase and the amplitude, respectively, of the components of the electric vector **A**. In addition, depolarization of light due to multiple scattering can occur when the material becomes highly turbid. We note that isotropic retarders and isotropic attenuators can be regarded as particular cases of their anisotropic counterparts.

**Consecutive optical elements.** If there is an array of m optical elements in series, each can be described by its particular Jones matrix. The net result on the polarization of the traversing beam by a series of n polarizing elements can be obtained by simple matrix multiplication [10]:

$$\mathbf{A_m} = \mathbf{J_m} \cdot \mathbf{J_{m-1}} \cdot \ldots \cdot \mathbf{J_2} \cdot \mathbf{J_1} \cdot \mathbf{A_0} \quad .$$

The expression above implies that all these Jones matrices have been calculated with respect to the same orthonormal basis set of directions.

Suppose the thickness of our sample is divided into m slices of thickness Δy. Then the cumulative change in the polarization state of the light upon transmission through the sample is:

$$\mathbf{A_m} = \prod_{i=1}^{m} J_i = \prod_{i=1}^{m} e^{\left(\frac{2\pi\ n_{xx}(y_i)\Delta y}{\lambda}\right)} \begin{bmatrix} 1 & 0 \\ 0 & e^{-i\,\delta(y_i)} \end{bmatrix} \mathbf{A_o} \quad .$$

Note that the expression above implies that all slices have the same principal axis (so there is one set of orthonormal directions for which the Jones matrices of all slices are diagonalized). Defining the mean refractive index as:

$$\langle n \rangle = \frac{\sum n_{xx}(y)\Delta y}{d}$$

then

$$\mathbf{A_m} = e^{\left(\frac{2\pi\langle n\rangle 2l}{\lambda}\right)} \begin{bmatrix} 1 & 0 \\ 0 & e^{-i\sum\delta(y_m)} \end{bmatrix} \mathbf{A_o} \quad .$$

In the limit Δy → 0, the sum may be expressed as an integral, so:

$$\mathbf{A_m} = e^{\left(\frac{2\pi\langle n\rangle d}{\lambda}\right)} \begin{bmatrix} 1 & 0 \\ 0 & e^{-i\int_{-l}^{+l}\delta(y)dy} \end{bmatrix} \mathbf{A_o} \quad .$$

The continuum approximation assumes the smallest length scale of interest is greater than the structural length scale of the material. In the present case, we restrict depth sections to 30 μm or more. The texture in highly oriented skin and in the fine-grained layer are consistently on length scales ≤ 5 μm; the sausage layer may sometimes violate the separation of length scales.

**Application to shear-induced crystallization experiments.** In our flow-induced crystallization experiments, we monitor the overall intensity that passes through the sample. Polarimetry measurements are only taken at early stages when not very much turbidity has developed. Therefore, there is little absorption or scattering (even isotropic) by the sample, so neither dichroism nor depolarization are significant. Thus, in the depth sectioning method we only need to consider the retardance contribution of each depth slice to the final signal.

In addition, the symmetry of shear flow provided a significant simplification because the principal axes of the optical anisotropy tensor in the (x,z) plane coincide with the x- and z- axis. This is true throughout the depth of our sample (i.e., for the different shear stresses), and it is true both for the retardance that arises during shear flow (as considered above), and for the retardance that arises from the ongoing oriented crystallization after shear has stopped. After flow, the growth of retardance arises from the growth of oriented crystallites nucleated by the flow-induced precursors and, in iPP, their epitaxial daughters. The growth process does not alter the symmetry in the (x,z) plane. Thus, the principal axes coincide with the x and z directions.

### 3.2.2.2 X-ray measurements: WAXD and SAXS

In the previous section, our optical measurements dealt with changes of polarization in the transmitted beam. Therefore, it was important to take into account the effect that consecutive different depth slices of the sample have on the beam that is being transmitted through the sample. We have shown that under our experimental conditions, the retardance (calculated from our intensity measurements) is the additive observable to account the contribution of each depth slice. In the case of WAXD and SAXS under our experimental conditions, however, it is the actual observed intensity (that is, the recorded scattering patterns) that can be added for each depth slice.

We assume that the scattered X-rays interfere with other scattered X-rays but do not undergo any further interactions with other atoms (this is the kinematic theory of diffraction) [11]. The thickness of our sample is thin enough and its scattering power is low enough that most photons pass through our sample undeviated, a few will be scattered once, and that any multiple scattering that may occur will be negligible. Exceptions to this approximation can occur, for example, in a large, perfect crystal, in which a diffracted ray could be diffracted many times in different regions before finally leaving the crystal (dynamic theory of X-ray diffraction). Because this assumption is valid for the entire thickness of our sample (0.5 mm), it will also apply to each of the depth slices considered.

We also assume the Fraunhofer approximation is applicable: all scattered X-rays arriving at a given observation point (i.e., at the detector) are parallel (this would exclude observation points at a distance from two or more scattering points that are comparable with the separation between the points) [11]. This is equivalent to considering the observation distance as effectively infinite. In our case, the total thickness of our sample (0.5 mm) is very small when compared with the camera length (which is typically > 170 mm for WAXD and > 6000 mm for SAXS measurements). Consequently, the Fraunhofer approximation will also be applicable for the whole sample, and therefore, for each of the depth sections within it.

The two assumptions described above imply that inverse Fourier transformation can be applied to determine the angular distribution of the X-ray scattering amplitude from the electron density of the scattering substances, and the composite amplitude of the scattered waves from a discontinuous set of points may be found by a simple summation of their individual scattering amplitudes and the appropriate exponential phase terms for their path differences relative to a convenient origin [11]. For scatterers that are numerous and more or less continuously dispersed in space in the sample:

$$A(\mathbf{s}) = \int_V \rho(\mathbf{r}) e^{-iq\mathbf{r}} d\mathbf{r}$$

where $A(\boldsymbol{q})$ is the normalized (by the incident $A_o$) amplitude of the scattered wave, $d\boldsymbol{r}$ is a volume element ($dxdydz$ around $\boldsymbol{r}$), $V$ is the scattering volume, $\rho(\boldsymbol{r})$ is the scattering length density distribution, and ***q*** is the scattering vector. Therefore, *A(**s**)* is the 3-dimensional Fourier transform of *ρ(**r**)*. The integration has to be performed over the illuminated volume sample *V*.

In the experiments, what we actually observe are the scattered intensities *I*, which are related to the scattered amplitudes *A* by:

$$I(\mathbf{q}) = \left\langle \left| A(\mathbf{q}) \right|^2 \right\rangle = \left\langle \left| \int_V \rho(\mathbf{r}) e^{-iq\mathbf{r}} d\mathbf{r} \right|^2 \right\rangle = \int_V \Gamma_\rho(\mathbf{r}) e^{-iq\mathbf{r}} d\mathbf{r}$$

where $\Gamma_\rho$ is the autocorrelation function of *ρ(**r**)*, and *V* is the illuminated volume of our sample. Where the origin of ***r*** is taken does not matter, and $\Gamma_\rho$ goes to $<\rho^2>V$ when ***r*** is large enough that there is no correlation in the density. For our depth sectioning method, we are "dividing" the sample in depth slices (volumes) of scattering samples. The thickness of these slices is always much greater than the length-scale periodicities that give rise to our WAXD and SAXS patterns, that is, there is no long range order at the size scale of the thickness of our slices contributing to the scattering patterns. As a result, the derivation of intensity described above applies for each slice *m* (with volume $V_m$) independently, and the sum of the contributions of all the slices to the total scattered intensity will be simply the addition of integral corresponding to each volume of slice illuminated, that is, the intensity arising for each of those slices. Because the intensities are simply summed, it is easy to realize that there is commutative property: the order of the slices does not affect their contribution to the scattering pattern.

## 3.3 Experimental

### 3.3.1 Materials

A bimodal blend containing 1% in weight of high molecular weight isotactic polypropylene (3500k, of $M_w$ = 3500kg/mol and PDI = 1.8) in a lower molecular weight iPP resin (Base-PP, of $M_w$ = 186 kg/mol and PDI = 2.3) was employed. The details on these individual components and on the solution blending procedure are given in the experimental section of Chapter II.

### 3.3.2 Flow-induced crystallization apparatus and protocol

The experimental apparatus and protocol are the same as were described in the experimental section of Chapter II. The specific conditions for isothermal flow-induced crystallization employed in this chapter were the following: temperature of crystallization ($T_x$) of 137˚C, and wall shear stresses ($\sigma_x$) that ranged between 0.065 and 0.036 MPa and that were imposed for both shearing times ($t_s$) of 7 s and 12 s.

### 3.3.3 In-situ optical measurements

The details of the optical setup and measurements are those described in the experimental section of Chapter II. From the $I_\perp/(I_\perp+I_{||})$ measurements obtained, we can compute the retardance $\delta$ due to the sample:

$$\delta = 2\arcsin\sqrt{\frac{I_\perp}{I_\perp + I_{||}}}$$

We employ this method for early times, before the measured intensity reaches its first maximum (when $\delta/2 = \pi/2$). At later times, we simply compute the points in time at which we observe the successive maximums and minimums in the intensity and for which the corresponding retardance is known ($\delta/2 = \pi/2$, $\pi$, $3\pi/2$, etc.). To apply the depth sectioning method, the retardance was computed for each of the experiments, rescaled to account for the corresponding optical path (as illustrated in Figure 3-2), and subtracted appropriately to isolate the contribution to the total retardance arising from each depth slice. For the data ranges where the retardance had already gone over orders, we utilized a linear interpolation between the values of $\delta$ corresponding to “peaks” and “valleys” for performing the subtractions. Then, the average birefringence $\Delta n$ of each depth section was computed from its retardance $\delta$ as follows:

$$\Delta n = \frac{\delta\lambda}{2\pi d}.$$

where $d$ is the thickness of each depth slice, and $\lambda$ is the wavelength.

### 3.3.4 In-situ X-ray measurements

Real-time WAXD measurements were performed at the X27C beamline of the National Synchrotron Light Source, Upton, N.Y. The experimental setup is the same, except that the windows used consist of beryllium (which are largely X-ray transparent). The wavelength used was 1.371 Å. A MARCCD camera was used as the detector and placed at ~ 17 cm from the sample position. We used an $Al_2O_3$ standard to calibrate the camera length. The real time WAXD work in this chapter was done in collaboration with D.W. Thurman. We jointly collected the real-time WAXD data at the National Synchrotron Light Source, Upton, N.Y. D.W. Thurman performed real-time WAXD data analysis, which can also be found in Chapter V of reference [8].

For applying the depth sectioning method, we performed the subtraction of the WAXD patterns at each point in time (which had been previously rescaled to account for the differences in optical path, Figure 3-2). Finally, the intensity corresponding to each depth slice was normalized by the thickness of the slice, so that all our derived quantities correspond to the average characteristic of each depth section.

The data processing of the 2D WAXD patterns involves performing a background subtraction of the pattern corresponding to the empty cell (no sample). All acquired patterns are normalized by the incident intensity of the X-ray source and by the acquisition time employed. In our experiments, we typically employ 5 s frames at early time (to capture the rapid changes that can occur shortly after shear), and then 30 s frames at later times. We analyzed the intensity distribution vs. the scattering vector $\boldsymbol{q}$ and vs. the azimuthal angle for the crystallographic reflections that correspond to the (110) and (040) planes of the α morph of isotactic polypropylene. The amorphous contribution was subtracted prior to performing the azimuthal scans of intensity. Then, the (040) reflection was used to estimate the isotropic crystalline contribution to scattering, which was subtracted from the (110) azimuthal scan. The reason for utilizing the (040) reflection is that when there are oriented parents and their epitaxial daughters both scatter intensity only in the equatorial region for the (040) plane (as they share the direction of the b axis) so the isotropic part can be more accurately determined. In contrast, the parent lamellae and their epitaxial daughters scatter at different angles in the (110) reflection, which makes it possible to distinguish the contribution of each type of population. After the isotropic baseline was subtracted from the (110) intensity, a geometrical correction of the intensity was applied to estimate the amounts of parent and daughter lamellae [12]. Azimuthal scans were fitted by Lorentzian peaks, and the area and FWHM for each one of them was computed. The areas of the (110) parent and daughter peaks were used to calculate the ratio of these types of lamellae.

### 3.3.5 OPM ex-situ characterization

Ex-situ sections of the flow-velocity gradient plane were obtained from the quenched sample and examined under crossed polars in an optical microscope. The samples were imaged such that the polarizer was placed at 45° from the flow direction.

### 3.3.6 Ex-situ microfocus WAXD characterization

Slices of thickness ranging between 0.5 and 1 mm of the ex-situ sample corresponding to the flow-velocity gradient plane were obtained and used for microfocus WAXD characterization. Experiments were performed by J.W. Housmans at the ID13 beamline of the European Synchrotron Radiation Source (Grenoble, France). A beam of 5 μm size was used to scan the sample in 5 μm steps. The wavelength was 0.984 Å, and the WAXD patterns were collected with a CCD camera of 1024x1024 pixels, and pixel size of 157.88 μm. The X-ray probe traversed the sample in the direction normal to the flow-velocity gradient; thus, the direction of this ex-situ beam is perpendicular to that of the in-situ optical and X-ray beams. Rastering the micro-beam across the sample allows us to spatially resolve the final WAXD patterns arising from various distances from the wall, i.e., from each level of shear stress. To match the results obtained from depth-sectioning of the real-time WAXD patterns, we performed the average of the particular ex-situ patterns that corresponded to each of the slices considered in depth-sectioning.

## 3.4 Results

We applied the depth sectioning method to the real-time retardance and WAXD measurements obtained for two different shearing times (7 s and 12 s) and a maximum shear stress of 0.065 MPa. First we examine the depth dependence of the rheo-optical and WAXD results for a fixed shearing time $t_s$ = 12 s. Then, we compare the results for 7 s and 12 s. Finally, we relate the real-time depth sectioning data to the final ex-situ structure obtained using microfocus WAXD on samples that had been cooled to ambient temperature and removed for subsequent analysis.

In the following, we refer to depth sections and discuss our results in terms of the distances from the wall that would correspond to the highest wall shear stress used in this series of experiments ($\sigma_w$ = 0.065 MPa). Thus, this wall shear stress is implicitly considered as the reference in this case because it allows visualizing the depth sectioning results as corresponding to the different distances from the wall for the sample sheared at the highest stress.

### 3.4.1 Depth sectioning of retardance measurements for $t_s$ = 12 s

At very early times—during and right after shearing—the sensitivity and speed of rheo-optical measurements allows us to observe the average birefringence of each depth slice time (Figure 3-3, top). Upon inception of shear, the melt stress optical contribution appears immediately as a small step increase. For the outer section (up to 27 μm), a further increase in birefringence starts ~ 4.5 s after inception of flow. Then, after flow has stopped, the birefringence continues to rise with approximately the same slope as at the end of the shear pulse. The only other slice that shows development of retardance during the shear pulse is the adjacent one, 27 to 62 μm from the wall. For this second section, the growth of birefringence starts later (after 7 s of shearing), and the value of the birefringence that is reached by the end of the shear pulse is smaller in magnitude than for the outer 27 μm. Its rate of growth diminishes slightly when flow stops. Both growth rates (during and after flow) are smaller than for the outer slice.

After cessation of flow for as long as birefringence measurement is possible (i.e., until turbidity becomes significant), the birefringence of the outermost 27 μm rapidly increases (Figure 3-3, middle). With decreasing shear stress (increasing depth) the retardance develops more slowly (Figure 3-3), slightly so at depths corresponding to the oriented skin (~ 60 μm) and significantly so in the "dense sausage layer" (~ 60 – 100 μm) seen ex-situ (Figure 3-2, far left micrograph). At still greater depth, birefringence is very low.

The raw data used to compute the depth sections is the light intensity transmitted through crossed polarizers normalized by the total intensity transmitted by the sample (Figure 3-3, bottom). The raw data recorded for each of four experiments performed at progressively lower wall shear stresses shows the qualitative trends evident above. The sample subjected to the lowest stress develops negligible retardance (late rise in $I_\perp$ may be partly due to depolarization). If the sample is subjected to $\sigma_w = 0.049$ MPa, it has a central portion with no retardance and two outer layers (one near each wall) that build up retardance that reaches the first order ($\delta'/2 \sim \pi/2$) at $t \sim 250$ s. The highest two shear stresses show that layers of much greater crystallization rate and anisotropy are induced: the retardance goes over multiple orders (first peak indicates $\delta'/2 \sim \pi/2$, first minimum $\delta'/2 \sim \pi$, etc.).

Retardance measurements are limited to early times because the turbidity of the sample increases as crystallization progresses. Despite this limitation, depth sectioning of the rheo-optical measurements accurately identifies the most interesting conditions for study with synchrotron radiation. Once the sample has become significantly turbid, multiple scattering gives rise to depolarization of the beam. Burghardt and coworkers [13] determined in studies of spectrographic birefringence for liquid crystals that calculating birefringence from successive maxima and minima is adequate even when there is significant depolarization. Therefore, we include successive maxima and minima in our analysis until the transmitted intensity falls to 20% of the initial one; this limitation is reached at ~ 64 s for the highest stress, ~ 315 s for 0.058 MPa, and > 400 s for the two lowest $\sigma_W$. All of the birefringence values shown in the middle graph of Figure 3-3 fall within this range except the last data point for the outermost section (for which transmittance was ~ 12%).

### 3.4.2 Depth sectioning of WAXD measurements for $t_s = 12$ s

At each acquisition time, the WAXD pattern for each depth section is analyzed to extract some important quantities (Figure 3-4): amount of oriented crystallites that have formed (the azimuthal integral of the (110) reflections over a wedge about the equatorial direction, which corresponds to the intensity arising from the oriented parent crystallites $A_{P,110}$); a measure of the degree of orientation (the azimuthal FWHM of the equatorial peak, $FWHM_{P,110}$); and a measure of the relative populations of parent crystallites and their epitaxial daughers. The initial growth rate of the parent (110) area $A_{P,110}$ (Figure 3-4, top) is greatest for the highest shear stress, and becomes progressively smaller for the inner sections. The core section (> 102 μm) shows very little growth for the duration of the experiment (~ 1200 s). Additionally, for the two outermost sections, the rapid initial rise in $A_{P,110}$ is followed by an abrupt change its rate of development, which occurs at relatively early times.

The three outer sections are very highly oriented (Figure 3-4, middle), being the FWHM $A_{P,110}$ between the two slices corresponding to higher shear stresses the narrowest and indistinguishable. However, the core section presents very weak orientation (significantly higher FWHM with large uncertainty due to smaller, poorly oriented peaks).

The proportion of parent (P) lamellae to daughter (D) lamellae is observed to be considerably greatest for the outermost 35 μm, intermediate for the second slice, and reaches a similar smaller value for the two inner sections (Figure 3-4, bottom). Values cannot be obtained for early times until the daughter peaks rise above the noise.

### 3.4.3 Ex-situ optical microscopy for 7 s and 12 s

The ex-situ polarized optical micrographs for samples sheared for either 7 s or 12 s at 0.065MPa (Figure 3-5) show that, relative to the case of $t_s = 12$ s, the sample subjected to $t_s = 7$ s has a thinner highly oriented skin and larger structures in the core. The horizontal lines indicate the depth slices considered previously for the real-time WAXD measurements (0-35 μm, 35-74 μm, 74-102 μm, and > 102 μm). From the real-time WAXD results above for $t_s = 12$ s and below for $t_s = 7$ s, it is clear that most of the crystallites formed at depths > 102 μm did not form during the first 1200 s. The structures seen ex-situ in these samples (which were cooled from $T_x$ to 25˚C after 5400 s) may contain crystallites in the core that grew non-isothermally.

The sample sheared for 12 s (Figure 3-5, left) possesses a highly oriented skin layer from the wall up to ~ 60 μm, which covers the first depth section and most of the second one. In contrast, the highly oriented skin for $t_s = 7$ s (Figure 3-5, right micrograph) only spans the outer ~ 30 μm (nearly all the first slice). For both $t_s = 7$ s and 12 s, at inner depths (from the oriented skin up to ~ 175 μm, throughout the third section and half of the forth section) there is a wide area populated with sausage-like birefringent structures (explained in Chapter II). The density of these sausages is higher in the region closer to the wall (up to ~ 100 μm). At comparable depths, sausages are relatively more dilute for $t_s = 7$ s than for $t_s = 12$ s. Finally, the inner core (> 175-200 μm) is comprised of structures that do not appear to be oriented, and of size scales that vary from fine to coarse.

### 3.4.4 Effect of shearing time (7 s and 12 s) at different depths

For the outer section (up to 27 μm), both $t_s = 7$ s and 12 s behave very similarly during and right after flow (Figure 3-6). For $t_s = 7$ s, the retardance starts growing suddenly after ~ 4.5 s from the start of shear; the melt birefringence ($t < 4.5$ s) and the upturn quantitatively agree with the observations made for $t_s = 12$ s, indicating excellent reproducibility of the experiments and the depth sectioning analysis. Surprisingly, between 7 s and 12 s, the increase in birefringence following cessation of shear for $t_s = 7$ s also accords with that observed during continued shearing for the case $t_s = 12$ s. The additional

5 s of shear for $t_s = 12$ s appear to have had no consequence. At all longer times the increase in birefringence for $t_s = 7$ s continues to parallel that for the case of $t_s = 12$ s in the outermost 27 μm (Figure 3-7, top). Inner depths in the sample also show quantitative agreement between the transient birefringence during the $t_s = 7$ s pulse and the first 7 s of the $t_s = 12$ s shear pulse. However, at all greater depths the first 7 s only show melt birefringence (there is no upturn). Over longer times, after cessation of flow, the second section (27-62 μm) develops significant birefringence (Figure 3-7, top). The deeper sections do not.

From the 2D WAXD patterns, consider first $A_{P,110}$, a measure of the population of oriented parent crystallites. To compare the behavior following 7 s of shear to that after 12 s, the earlier result for $t_s = 12$ s in Figure 3-4 (top) is shown as open symbols together with the results for $t_s = 7$ s as filled symbols (Figure 3-7, middle). In accord with the birefringence results for $t_s = 7$ s and 12 s, for the outermost layer (here up to 35 μm) $A_{P,110}$ rises and rolls off in much the same way for $t_s = 7$ s as it does for $t_s = 12$ s. The second section (35-74 μm in the WAXD experiments) shows much weaker growth of $A_{P,110}$ following 7 s of shear than for 12 s of shear. Again, this accords with the birefringence results. At greater depths negligible oriented growth occurs for $t_s = 7$ s, also in accord with the birefringence results.

The birefringence increase after cessation of flow and increase in the population of oriented parent crystallites both arise from the same underlying oriented precursors created during flow. Most closely related to the precursor population created during flow is the earliest measurable growth of oriented crystallites from them. Therefore, the initial rates of increase of birefringence and $A_{P,110}$ are compared (Figure 3-7, bottom). The initial slope after shear cessation was determined by a linear fit. Then, all slopes were normalized by the slope corresponding to the outermost layer for $t_s = 12$ s (corresponding to $\sigma = 0.064$ MPa for WAXD and 0.065 MPa for $\Delta n$). In addition to showing very good agreement between $\Delta n$ and WAXD results, this presentation shows that shearing time between 7 s and

12 s has little effect at the highest stresses and at the lowest ones—but produces pronounced differences at intermediate stresses.

The effect of shearing time on the degree of orientation (Figure 3-8, middle) follows the same trend as the initial rate of growth above. The first 35 μm reveal a high degree of orientation which is indistinguishable between $t_s$ = 7 s and 12 s. The next two sections show marked differences: The FWHM is much smaller (greater orientation) for 12 s than for 7 s of shearing. The core section shows very low and similar degrees of orientation for both shearing times.

Finally, it is significant that for the outermost 35 μm, the P:D ratio (Figure 3-8, bottom) is considerably larger for 12 s of shearing time (P/D ~ 6) than for 7 s (P/D ~ 3). This is in contrast to the observations made on all the other quantities: The initial growth rate of retardance and of $A_{P,110}$, the time at which the abrupt change in rate occurs, and the degree of orientation did not significantly change between $t_s$ = 7 s and 12 s for this outer slice. For the second depth section, the P:D ratio is again greater for $t_s$ = 12 s (P/D ~ 4) than for 7 s (P/D < 2), although the magnitude of the change is somewhat smaller. Lastly, all shearing times for the third and fourth present a similar lower parent to daughter ratio (P/D < 2).

### 3.4.5 Comparison between in-situ depth-sectioned WAXD and ex-situ spatially-resolved micro-WAXD for $t_s$ = 7 s and 12 s

We now compare the structure revealed by the depth-sectioned real-time WAXD patterns taken at the end of the 137˚C isothermal experiment (at 1145 s, beam configuration as shown in Figure 3-9, left) and the ex-situ spatially resolved WAXD patterns obtained after the sample was quenched to room temperature and stored for about six months (Figure 3-9, right).

The comparison of the final depth-sectioned real-time WAXD 110 azimuthal scans (Figure 3-10) with the ex-situ spatially resolved results Figure 3-11) clearly indicates that some parts of the sample only crystallized under non-isothermal conditions after they were quenched to ambient temperature. The real-time WAXD results shown here have not had the isotropic contribution subtracted yet, and neither has the geometrical correction to estimate areas of parent and daughter crystallites been applied; only the amorphous contribution has been subtracted. The real-time scans show very little isotropic crystallization during the time of the isothermal experiment. In contrast, the ex-situ azimuthal scans of the (110) reflection for each slice (which include both the oriented and unoriented contribution to scattering, as well as the remaining amorphous halo) do show additional isotropic contributions that must therefore have arisen mostly during cooling.

For the sample sheared for $t_s$ = 7 s, the ex-situ WAXD patterns show that the high orientation of crystallites observed in the outermost slice (up to 35 μm from the wall, corresponding to the highly oriented skin seen in OPM) significantly decays when we scan inner sections of the sample, at the same time that isotropic crystallization intensifies (perceptible in the rise of the observed baseline). The innermost section of the sample presents mainly isotropic scattering, with very slight orientation. In contrast, the outermost two slices of the sample sheared for 12 s (up to 75 μm, thus comprising most of the oriented skin) show very high orientation, and essentially almost no isotropic contribution. The next depth section (up to 105 μm, which encompasses a region densely populated with sausages as seen in OPM) reveals a lower degree of orientation and some isotropic contribution to scattering. Finally, the central section has much more isotropic contribution but still shows a mild level of orientation (which is more pronounced than that for the equivalent section in the sample for $t_s$ = 7 s). Thus, the comparison of these ex-situ scans with the final real-time patterns indicates that for both $t_s$ = 7 s and 12 s, most of the central section of the sample (> 102 μm) crystallized after cooling. Additionally, a significant contribution to the final crystallization morphology occurred after quenching for the second and third slices corresponding to $t_s$ = 7 s.

## 3.5 Discussion

Shear-induced structure is relevant to diverse materials: block copolymers [14, 15], wormlike micelles [16-18], and liquid crystalline polymers [19], to name a few. Measurements of transient optical anisotropy [13, 20], SALS [21], SAXS [22] and WAXD [23, 24] are important tools for understanding microstructure evolution during flow. Therefore, the present method, which allows pressure-driven flow to provide local information corresponding to nearly uniform conditions that is usually associated with rheometric flows (Couette [25], sliding plate [26, 27], and parallel disk [28]). Pressure-driven flow offers the advantage of controlled-stress conditions and ease of sudden inception and cessation of shear. The robust relationship between shear stress and distance from the wall in a pressure driven flow that arises directly from a force balance makes this approach suitable for a range of different problems. Therefore, this method may prove widely useful in the field of complex fluids.

Here we have used the real-time depth sectioning method to analyze the real-time flow-induced development of crystallites as a function of level of shear stress (which, for a given maximum wall shear stress can be visualized as distances from the mold wall, i.e., depths within the sample). This is in contrast to "post-mortem" methods that directly probe the depth dependence of the structure after the sample has completely crystallized. The kinetics of flow-induced crystallization and morphology development in-situ provide insight into the process of creation of the highly oriented precursors by flow (whose formation is known to be strongly dependent on the stress imposed), and their impact on the ensuing crystallization kinetics.

In the following, we first discuss the depth sectioning method applied to an experiment with 12 s of shearing times. This condition presents a representative variation of morphology: the two outer sections correspond to a highly oriented skin, the third section comprises a region with abundant sausages, and the innermost section corresponds to the core. The upturn contribution during shear arising from each of the two sections of the skin can be isolated, and it becomes noticeable that at 137°C, the oriented structures created during shear do not relax. We are also able to isolate sharp signatures of impingement for the highly oriented skin. Afterwards, we discuss the comparison of depth sectioning results for two different shearing times (7 s and 12 s). On one hand, this comparison enables us to distinguish that the outer section of the skin has actually saturated by the time that 7 s of shearing have occurred. On the other hand, the signatures of proliferation of threads between these two shearing times can be deduced for intermediate depths.

### 3.5.1 Stress dependence of morphology development for $t_s = 12$ s

#### 3.5.1.1 Formation of threads during shear

Previous research observed the generation of long-lived oriented structures as an unusual upturn evident in the transient birefringence during flow [29]. The upturn was correlated with the subsequent growth of highly oriented crystallites and ex-situ observation of a highly oriented skin near the walls of the sample. Prior results indicated that a threshold stress $\sigma_{th}$ is required to trigger proliferation of shish, and that the stress must be sustained for a minimum duration, t*. In this context we set out to observe in real time the events that occur leading to the formation of the highly oriented skin. Indeed the present results indicate that $\sigma_{th} \sim 0.049$ MPa (corresponding to the two outer sections) for this bimodal material (at least for $t_s \leq 12$ s).

At stresses above $\sigma_{th}$, the threshold shearing time t* required for the shish to start proliferating decreases with increasing applied shear stress (Figure 3-3, top). In this case, above 0.058 MPa, the shish become dominant after 4.5 s of flow, while for stresses between 0.049 and 0.058 MPa, the shear needs to be sustained for 7 s in order for the oriented precursors to bloom and make the birefringence rise significantly above that corresponding to the melt flow. Thus, the generation of the long-lived oriented structures starts occurring earlier during flow for higher levels of stress imposed.

Furthermore, the birefringence increase immediately after the upturn begins shows distinct stress dependence. The initial slope of the birefringence right after t* (while flow is still imposed) is greater for the section situated at higher stress, which suggests that the rate of creation of total thread-length/volume during shear and past the critical time is greater when the shear stress imposed is higher. There can be at least three different contributions to the growth rate of the upturn that may be stress-dependent: 1) the number of threads present ($N_{th}$) that are growing in length (propagating) during flow, 2) the velocity of propagation of the threads ($v_p$) with flow, and 3) the rate of growth of lamellae (kebabs) already developing on the threads during flow (i.e., how "fat" the threads get during flow).

In the context of the model from Janeschitz-Kriegl [2], the threads that are propagating have started from point-like nuclei induced by shear in the melt. Thus, the population of point-nuclei builds up before the thread-like precursors start developing, and is known to depend on temperature and shearing conditions. The fairly sharp rise of the birefringence upturn suggests that a large number of threads start developing from their point-like nuclei at approximately the same time. For this reason, we hypothesize that the main contributions to the initial slope of the upturn are the propagation of an approximately constant number of threads and the growth of kebabs on those threads already during flow.

#### 3.5.1.2 Cessation of shear

When flow is stopped, the value of birefringence that has built up due to the upturn in the two outer sections does not relax, but instead it continues to grow (Figure 3-3, top). This indicates that the oriented precursors and associated oriented lamellae developed during shear do not noticeably decay at this temperature (137˚C) when flow is stopped. Then, the partial drop in $I_{\perp}/(I_{\perp}+I_{\parallel})$ observed in the experiments where an upturn develops but the depth sectioning method is not applied actually corresponds mainly to the relaxation of the melt in the central parts of the sample. To see this more easily we have re-plotted the average birefringence data from Figure 3-3 (top) into Figure 3-12, which illustrates the total retardance of each section (i.e., the average birefringence of a section multiplied by its thickness). The contribution to the melt flow birefringence of the outermost slices during flow is so small (see the early small step when shear starts) that it was the melt flow birefringence arising from the core section that dominated the overall signal.

The observation that, for the two outermost sections where threads are induced profusely, the rate of growth of birefringence hardly changes when flow is stopped (Figure 3-3, top) indicates that the growth of kebabs on the threads may already have a considerable contribution to the upturn during imposition of shear. That is, at 137˚C, significant growth of kebabs on the threads can occur while the precursors are being formed.

#### 3.5.1.3 Stress dependence of morphology development after cessation of flow

In accord with the model for flow-induced crystallization, the oriented structures formed during shear nucleate subsequent growth of oriented crystallites. Thus, they have a direct impact on the initial kinetics and orientation distribution of structure development. When the polymer is no longer being sheared, growth of crystallites is expected to occur as under quiescent conditions. With depth-sectioning, we have isolated the characteristics of growth corresponding to each slice (i.e., to different ranges of stress).

**Skin.** Previous studies in which the averaged signal through the flow channel and the ex-situ morphology were compared observed that an upturn in birefringence during shear and the subsequent rapid growth of retardance after cessation of flow correlated with the ex-situ observation of a highly oriented skin [29]. Thus, the upturn and highly oriented growth were attributed to arise from the outermost section of the sample where the skin developed. Here with the application of the depth sectioning method we confirm those results: We isolated the signal corresponding to the highly oriented skin observed ex-situ (two outer sections) and verified that only those two sections present an upturn and immediate oriented growth after shear.

Additionally, prior investigations of real-time WAXD in conjunction with ex-situ TEM examination of the final microstructure [3, 9] suggested that, for conditions where the highly oriented skin was formed, rapid highly oriented WAXD growth followed by saturation of the growth of crystalline peaks occurred and corresponded to the nucleation and growth of highly oriented crystallites on thread-like precursors until the lamellae growing off neighboring threads impinged with one another. In light of these findings, we ascribe the change of growth rate in $A_{P,110}$ of the two outermost depth slices to the impingement between kebabs propagating out from neighboring threads. The "knee" in growth rate occurs very early and at similar times for these two sections (indicating similar small interspacing between oriented threads), and it is very sharp (suggesting quite homogeneous spacing throughout each section). The high density of threads in the oriented skin also explains the very high orientation obtained for these depth sections: The threads template highly oriented growth but the lamellae do not have so much space to grow before they impinge to be able to diverge, so the FWHM remains very narrow. Although the interspacings appear to be quite similar for the two sections corresponding to the skin, the outermost section appears to have a bit more of thread-length to nucleate, since the initial growth rate is somewhat greater.

The P:D ratio is the only observable that shows a significant difference between the two outer sections of the oriented skin: the P:D ratio is noticeably higher for the outer 35 μm. The parent to daughter ratio is known to be a function of temperature, but as we are using isothermal conditions this will not contribute to any differences for the duration of the experiment. Another aspect to take into account is whether the geometry of growth on the shish will affect the P:D ratio. White and Bassett [30] compared lamellar growth from row-structures (after they had been created by shear, that is, lamellar growth occurred under quiescent conditions) to that arising from spherulites, and determined that the P:D ratio was independent on the geometry of nucleation (at least under their experimental conditions). However, our data does not support this, as the P:D ratio is observed to be significantly higher for the sections sheared at the higher shear stresses for 12 s.

A previous study also observed a greater P:D ratio arising from row nucleation when longer shearing times at high shear stresses were imposed on a iPP melt [23]. It was explained in terms of the parent lamellae (which have the chain axis along the flow direction) being preferentially formed during shear. Because a substantial amount of the crystallization had occurred during flow (about 50% of the crystallinity index at impingement was already present by the end of the shear pulse at high shear stress), the higher P:D ratio during flow conditions would skew the final value of P:D even if growth after cessation of shear occurred with the ratio typical of quiescent conditions. However, the data in our experiments demands a different explanation. We obtain significantly higher P:D ratio at the highest stresses but not enough growth has occurred by the end of the shear pulse as to significantly skew the P:D ratio. It seems, thus, as if the growth after cessation of flow also occurred with a P:D higher than under quiescent conditions.

**Sausage region.** At inner depths from the highly oriented skin in the sample for $t_s$ = 12 s, we encounter the third depth section which comprises an area densely populated with sausages, as seen in the ex-situ OPM. In contrast to the depth sections corresponding to the skin, the significantly smaller initial growth rates of retardance (which was not immediate after shear flow) and of $A_{P,110}$ indicate that the density of oriented precursors in the sausage region is significantly smaller. However, the rise in signals corresponding to oriented crystallites at relatively later times indicate that certain quantity of thread-like precursors has indeed formed (although they were so scarce that they did not cause an upturn in the birefringence during flow). These observations are in accord with what was inferred about the sausage region from average measurements in Chapter II. A change in the rate of the growth in $A_{P,110}$ is observed also for this depth slice, but it occurs at a significantly later time and in a much more gradual fashion than for the first 75 µm (indicating large and inhomogeneous inter-thread spacings, as confirmed by OPM).

The resulting lower crystallite orientation in the sausage area (particularly after impingement in the skin sections has already occurred) is also consistent with a lower density of threads: The oriented crystallites nucleated on them can grow up to much larger radius than those densely spaced in the skin, and at larger distances from the central thread there is a lot more space for lamellae divergence. The parent to daughter ratio is much smaller in this section (P/D < 2), which is in harmony with the observation that there was no significant growth of oriented crystallites during flow and probably corresponds to the P:D ratio characteristic of quiescent crystallization at 137˚C. This follows the trend observed for the skin sections: The growth of parent lamellae on threads after cessation of flow appears to be higher for the sections that were subjected to higher stresses.

**Core.** Finally, the central depth section (> 102 μm) mostly crystallized during cooling after the sample was quenched. The little growth of some oriented crystallites observed near the end of the experiment most possibly arise from the nucleation on very few thread-like precursors formed in the regions of higher stress. This is confirmed by the dilute sausage structures observed by OPM in the outermost regions of this central section, which very likely give rise to the contribution of mildly oriented crystallites to the dominant isotropic crystallization revealed by the ex-situ microfocus WAXD.

### 3.5.2 Depth dependence sequence of events between 7 s and 12 s of shearing

The application of our depth sectioning strategy to matched experiments that differ only in the shearing time aims at revealing the structure development that occurs at each depth slice when shearing between $t_s$ = 7 s and $t_s$ = 12 s.

#### 3.5.2.1 Saturation of precursor formation at high stress

At the highest stresses for the outermost depth section of each shearing time (both corresponding to highly oriented skin, from the wall to 35 μm), the development of the real-time observables is very similar. From the moment shear is started up to 7 s of shear, the rise of the retardance is the same for both experiments of $t_s$ = 7 s and 12 s, as expected (Figure 3-6). However, it is remarkable that for the next 5 s (that is, after cessation of flow for $t_s$ = 7 s but while the shear pulse is still imposed on the melt for $t_s$ = 12 s), the growth of birefringence is still very similar. In other words, the additional 5 s of shear in the case of $t_s$ = 12 s do not have an additional effect when compared with the case in which flow has stopped after 7 s. Thus, it appears that the structure formed during shear has already “saturated” by the time that flow has been imposed for 7 s.

After flow, both the initial rise in birefringence and the initial growth rate of the $A_{P,110}$ in the outer 35 μm are very similar for $t_s$ = 7 s and 12 s. The impingement time is very sharp and occurs at similarly early times, denoting similar and small inter-shish spacing for these two shearing times. Consistently, there is no significant difference in the degree of orientation of the parent 110 peaks. In contrast, the only manifest difference is the higher P:D ratio for $t_s$ = 12 s when compared to $t_s$ = 7 s. These results suggest that all the thread-length that could form at this level of stress has already developed by 7 s of shearing, and that the additional 5 s of shearing for $t_s$ = 12 s contribute in a way that mainly affects the subsequent P:D ratio, but that does not create more thread-length. Perhaps the additional shearing contributes by either fattening the shish (adding oriented crystallites with chain in flow direction), or creating kebabs preferentially of the parent type (because the chain axis is aligned in the flow direction).

Saturation of the density of threads has been previously observed by Kornfield et al. [9]: In that study, increasing the shearing time from 4 s to 8 s did not enhance the density of threads in the oriented skin as observed by TEM. A number of possible explanations that could cause saturation in the number density can be put forward. Perhaps when the thread-length/volume is very high, the threads themselves hinder each other from elongating even more. Or perhaps a depletion of long chains (which are known to be crucial for the development of threads) has occurred in a section past a critical thread density: if there are many threads very close together, most long chains may already be involved in them and further propagation cannot occur.

It is very significant that depth sectioning is crucial to detect the advent of saturation for the outermost 35 μm under the current experimental conditions. If only the raw measurement of the whole experiment was investigated, the contribution of inner sections to the overall measured signal (in this case, the signal corresponding to the second depth slice of $t_s$ = 12 s) would mask the saturation behavior observed in the outer section.

#### 3.5.2.2 Development of threads between 7 s and 12 s at intermediate stress

At intermediate stresses (second and third slices) there are large differences between $t_s$ = 7 s and $t_s$ = 12 s. The greater initial growth rates for the 12 s sections suggest that the amount of oriented nucleation surface created increases between 7 s and 12 s of shearing. The much more gradual character (or disappearance altogether) of the “knee” feature in $A_{P,110}$ for $t_s$ = 7 s indicates much lower densities of threads (larger and irregular spacings). Consequently, the sections for $t_s$ = 7 s are also less well oriented than those of $t_s$ = 12 s.

The comparison of thread-length formation between different shearing times at stresses such that threads are formed (so we are above the threshold stress), but saturation has not been reached, point to a range of conditions that must be carefully selected in order to study the velocity of propagation of threads. Clearly real-time depth sectioning can only provide relative values; in order to deduce absolute velocities of propagation, TEM should be performed on some samples to provide a “calibration” for the real-time measurements.

#### 3.5.2.3 No real-time changes at low stress

For the lower stresses that are too low (i.e., the innermost section of the sample), the real-time depth sectioning data does not display noteworthy differences between 7 s and 12 s. Minor dissimilarities for this region are found only in the ex-situ OPM (where slightly more sausages and smaller isotropic structures are observed for 12 s) and in the ex-situ microfocus WAXD (which reveals slightly more orientation on top of the isotropic contribution for the longer shearing times). These differences correspond to growth that occurred mostly after quenching the sample.

## 3.6 Conclusions

It is known that the creation of thread-like precursors is highly dependent on stress. Therefore, the depth-sectioning method sets the foundation for studying the effect of one of the most important variables that impact flow-induced crystallization. Then, the ability to isolate the events at different levels of stress opens up the way for studying how the creation of oriented thread-like precursors varies with other parameters as well, such as shearing time (as shown here), material properties (molecular weight, molecular weight distribution, isotacticity), and temperatures of shear and/or crystallization.

In this chapter we have applied the real-time depth sectioning method to flow-induced crystallization of isotactic polypropylene at 137˚C. Without this approach, the in-situ measurements provide an average over a profile of shear stress that varies linearly from the imposed wall shear stress to zero at the center of the channel. We have inferred that highly oriented precursors start forming first in the regions of higher shear stress (near the wall). For the highest stress used we observed that structure development during and after flow was saturated after a shearing time of 7 s, so that the kinetics of subsequent development were very similar for both $t_s$ = 7 s and 12 s. Also, we have deduced that there is significant kebab overgrowth on the threads already during flow as they are being created. For the lower stresses, lower densities of thread-like precursors were formed at later times, and their density did increase with the longer shearing time. The in-situ measurements are consistent with the depth dependence final morphology observed; however, the ex-situ observations do not allow for inferring the real-time structure development at different levels of stress, and in some instances they may reflect the morphology that appears when the sample is cooling (i.e., under non-isothermal conditions).

## 3.7 Figures

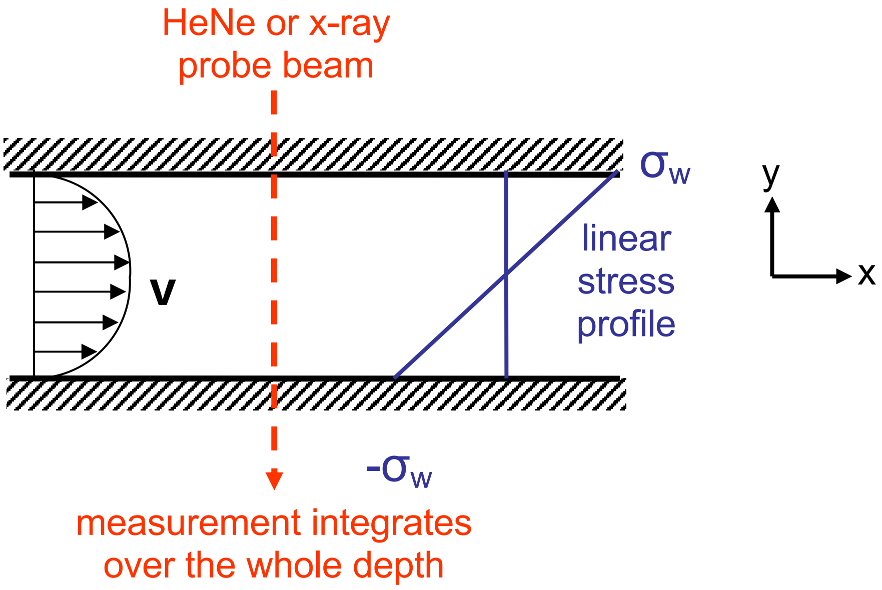

**Figure 3-1.** Diagram of rectangular slit channel for flow-induced crystallization showing the flow–velocity gradient plane xy and the path traveled by the real-time optical and X-ray beams

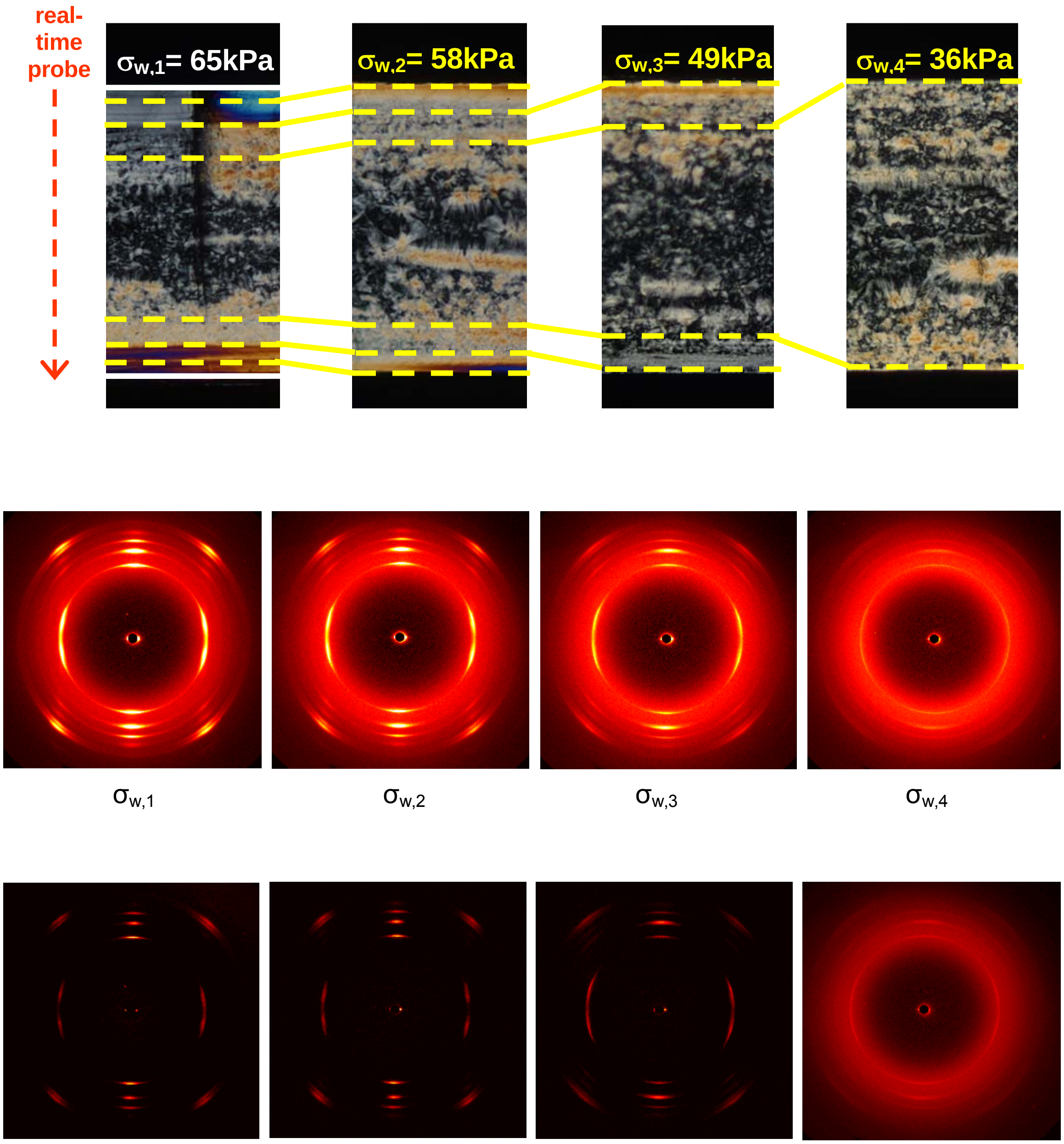

$\sigma_{w,1}$ $\sigma_{w,2}$ $\sigma_{w,3}$ $\sigma_{w,4}$

$\sigma_{w,1} < \sigma < \sigma_{w,2}$ $\sigma_{w,2} < \sigma < \sigma_{w,3}$ $\sigma_{w,3} < \sigma < \sigma_{w,4}$ $\sigma < \sigma_{w,4}$

Figure 3-2. Top: ex-situ polarized optical micrographs for samples sheared at 137°C, 12 s, and successively smaller $\sigma_{wall}$. Dashed lines show correspondence of shear stress. Middle: corresponding real-time WAXD patterns acquired after 1145 s for each experiment sheared at $\sigma_{wall}$. Bottom: resulting WAXD patterns after applying the depth sectioning method to the real-time WAXD at 1145 s shown on the middle row. Each pattern corresponds to the different depth sections indicated by dashed lines on the optical micrographs. Flow is in the horizontal direction.

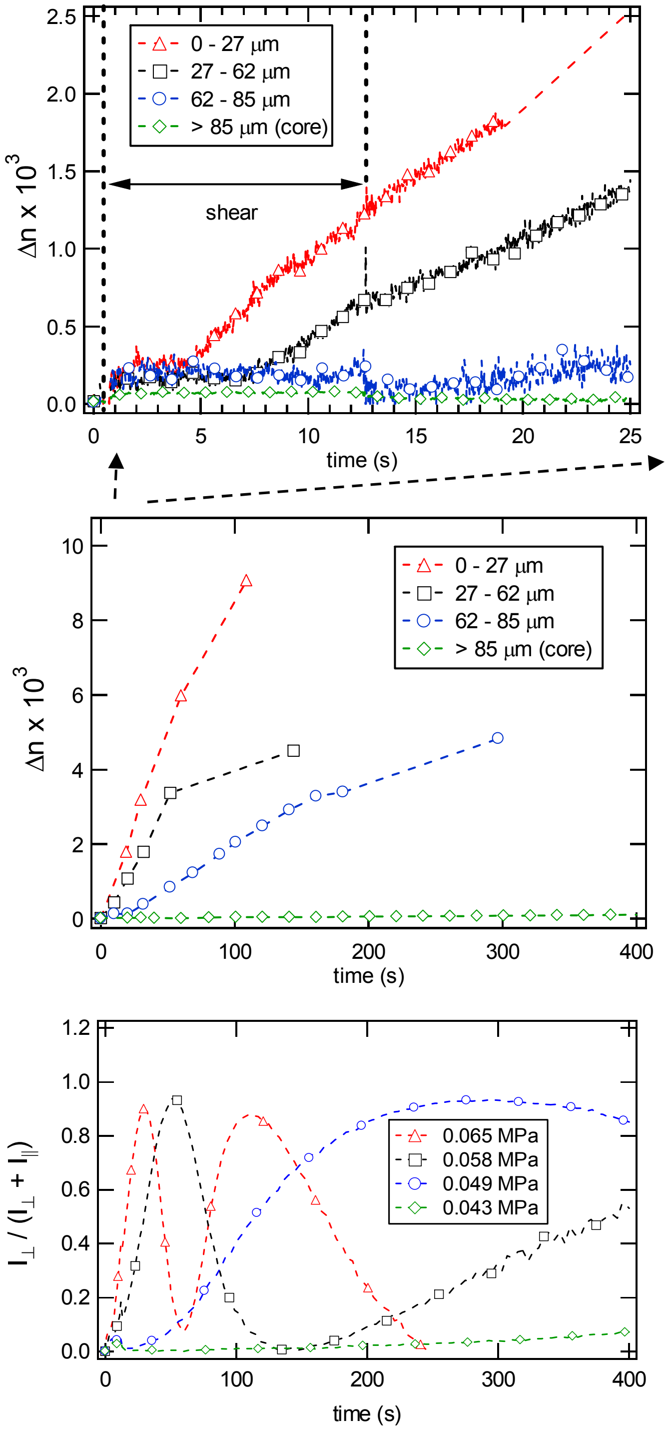

**Figure 3-3.** **Top: average birefringence for each section during and right after a 12 s shear pulse. Middle: development of the average birefringence for each depth section after shearing for 12 s at 137°C. Bottom: "raw" polarimetry results corresponding to each of the experiments (sheared for 12 s at progressively lower wall shear stresses) performed to calculate the top graph.**

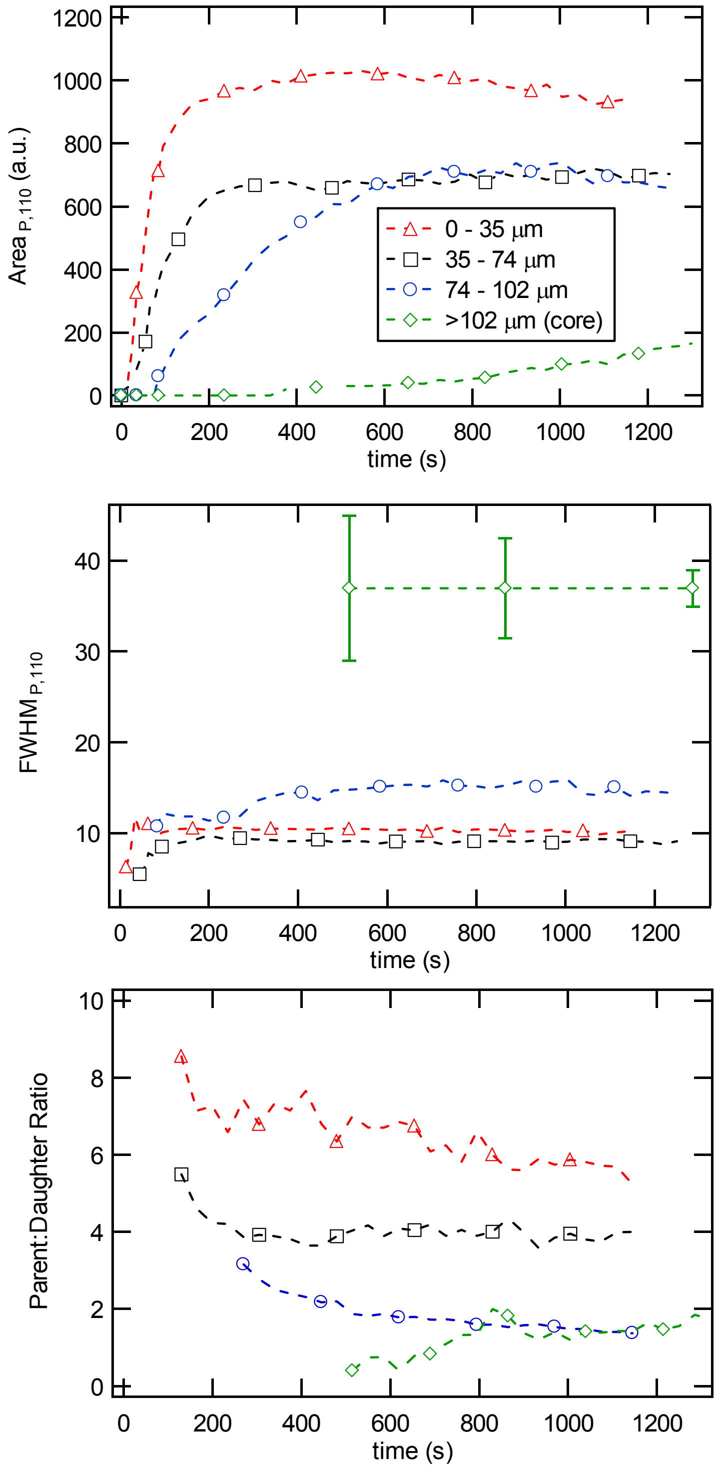

**Figure 3-4.** 12s depth sectioning applied to the WAXD patterns 137˚C. Top: area of the parent 110 peaks. Middle: FWHM calculated after fitting the peaks for the 110 azimuthal scan. Bottom: parent-to-daughter lamellae ratio after performing a geometrical correction of the observed intensity.

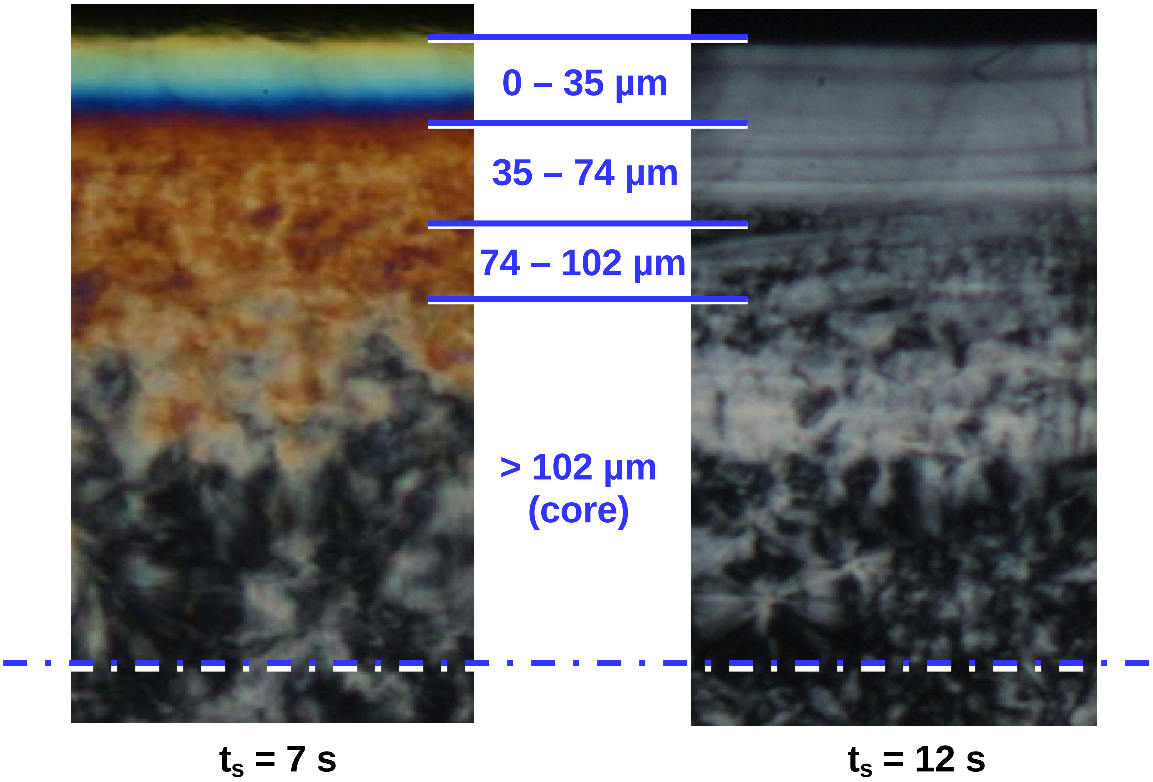

**Figure 3-5.** **OPM of 7s and 12s at 137˚C (highest shear stress = 0.065 MPa). The center of the sample is indicated by dash-dot line.**

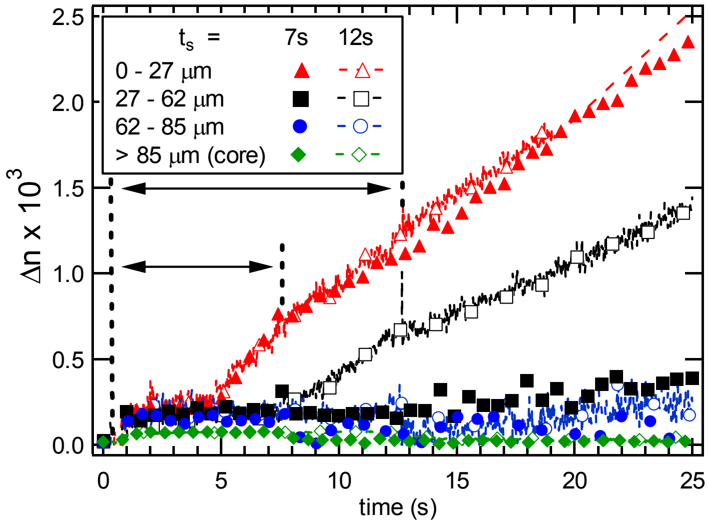

**Figure 3-6.** Average retardance for each depth section. Experiments performed at 137°C for both $t_s$ = 7 s and 12 s.

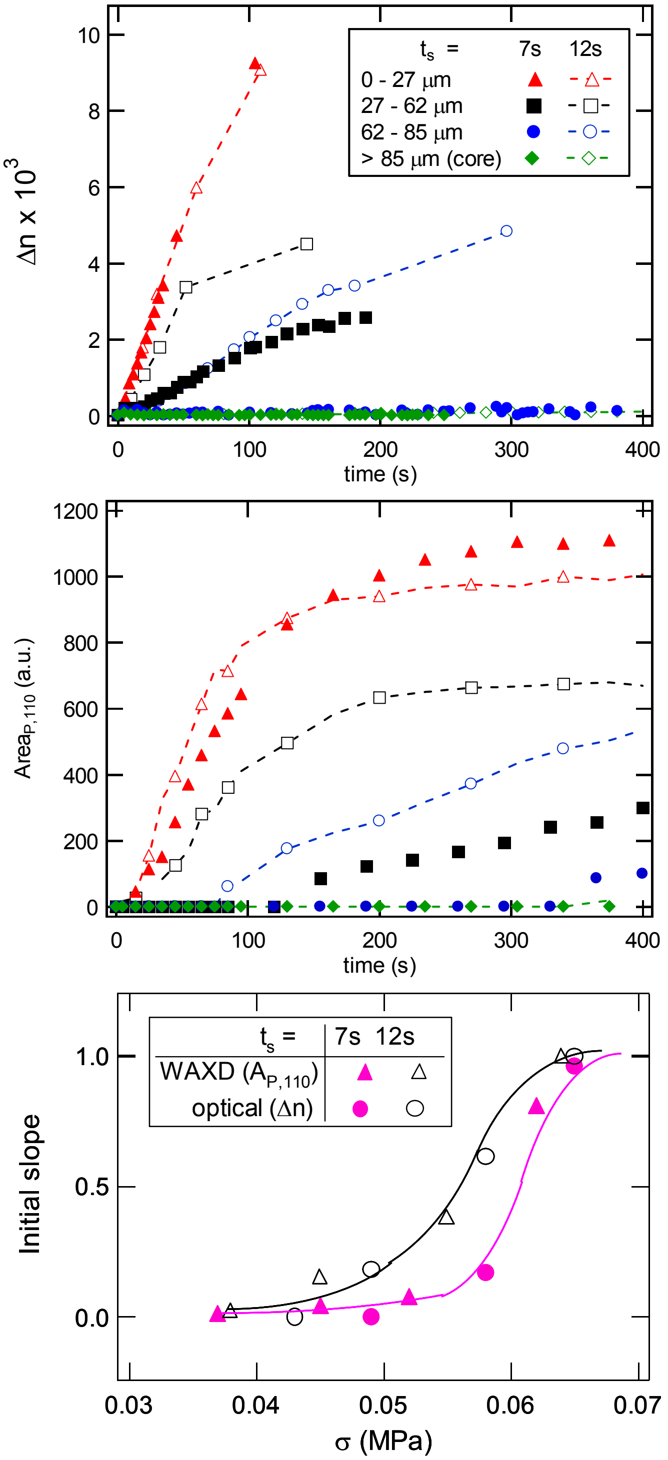

**Figure 3-7.** Depth sectioning of retardance (top) and WAXD (middle) for both shearing times of 7 s and 12 s at 137˚C. Bottom: dependence of initial rate of growth of normalized retardance and $A_{P,110}$ on shear stress.

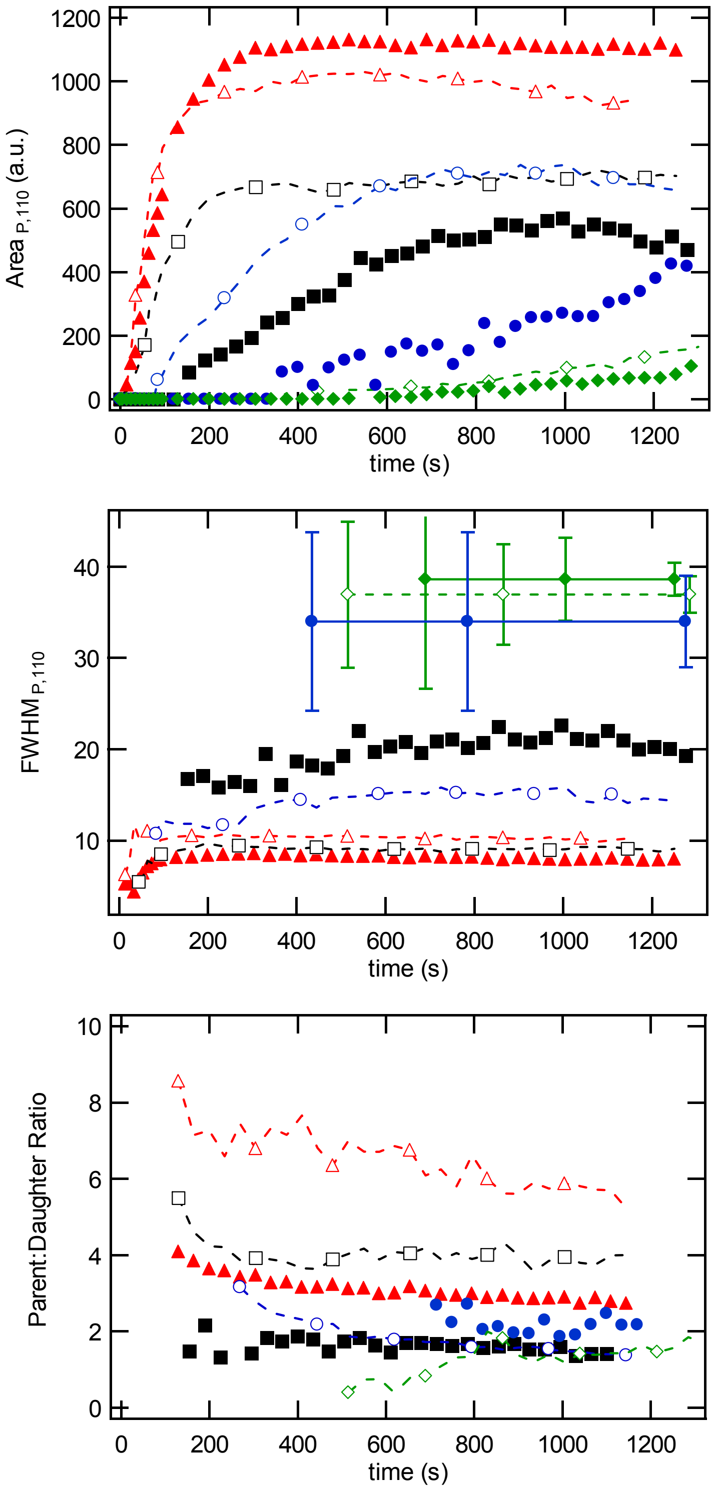

**Figure 3-8. Comparison of WAXD depth sectioning results for $t_s$ = 7 s and 12 s at 137°C. Top: area of parent 110 peak. Middle: FWHM of parent 110 peak. Bottom: parent-to-daughter ratio after geometric correction.**

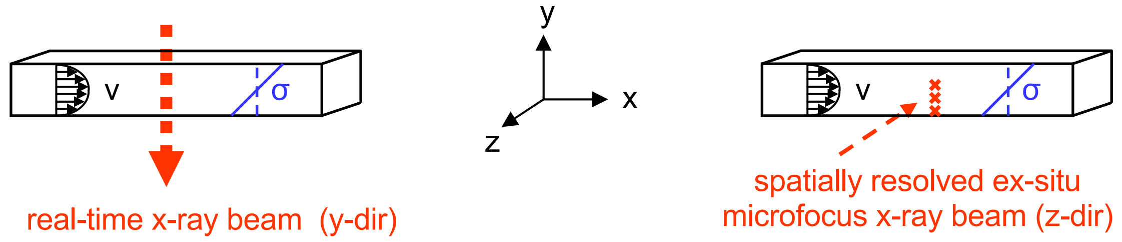

**Figure 3-9. Diagram comparing the sample-beam configuration in real time WAXD measurements (left) and ex-situ WAXD microfocus experiments (right)**

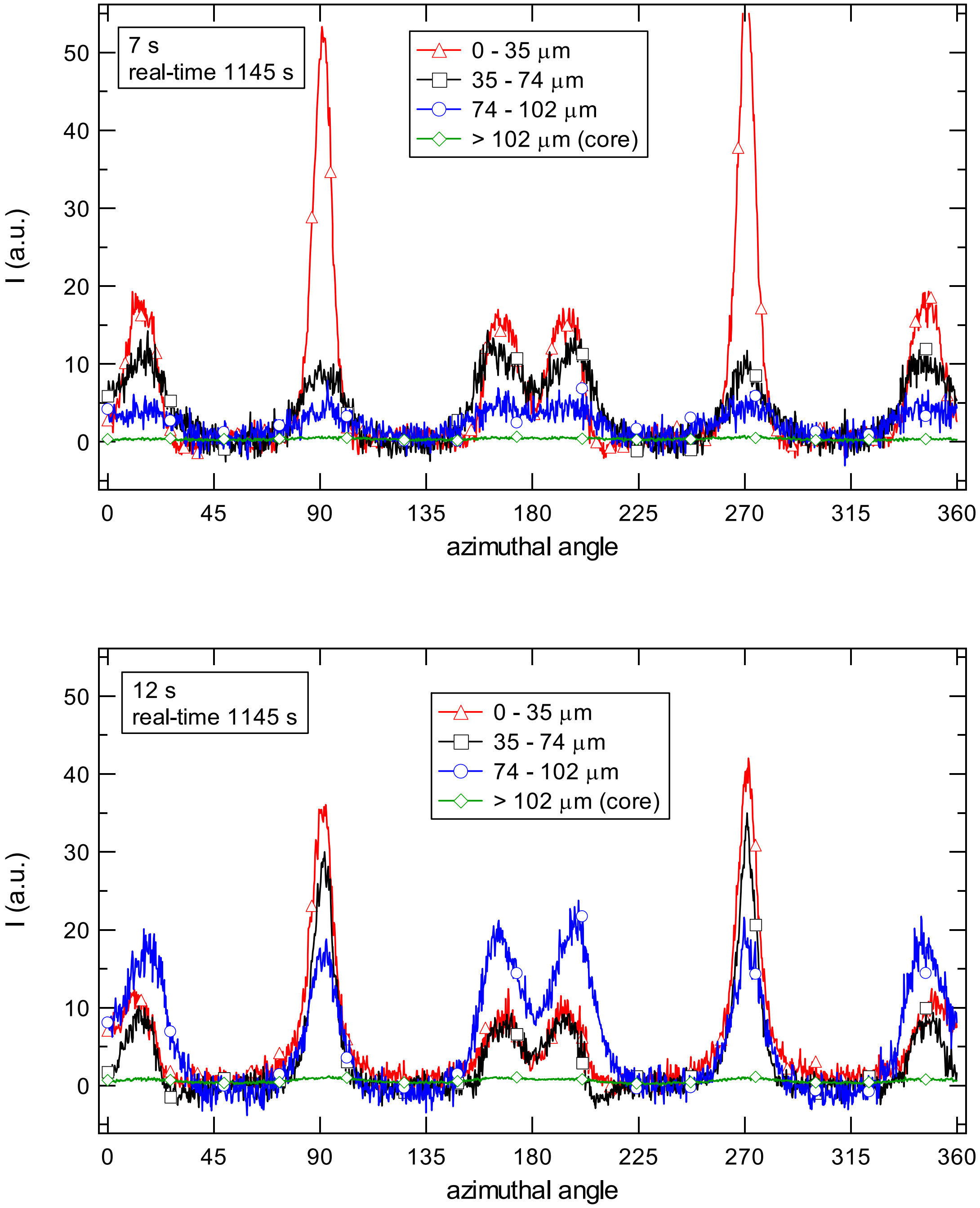

**Figure 3-10. Azimuthal scan of the (110) reflection of real-time patterns after applying depth sectioning. They correspond to 1145 s after shear has been imposed at 137˚C.**

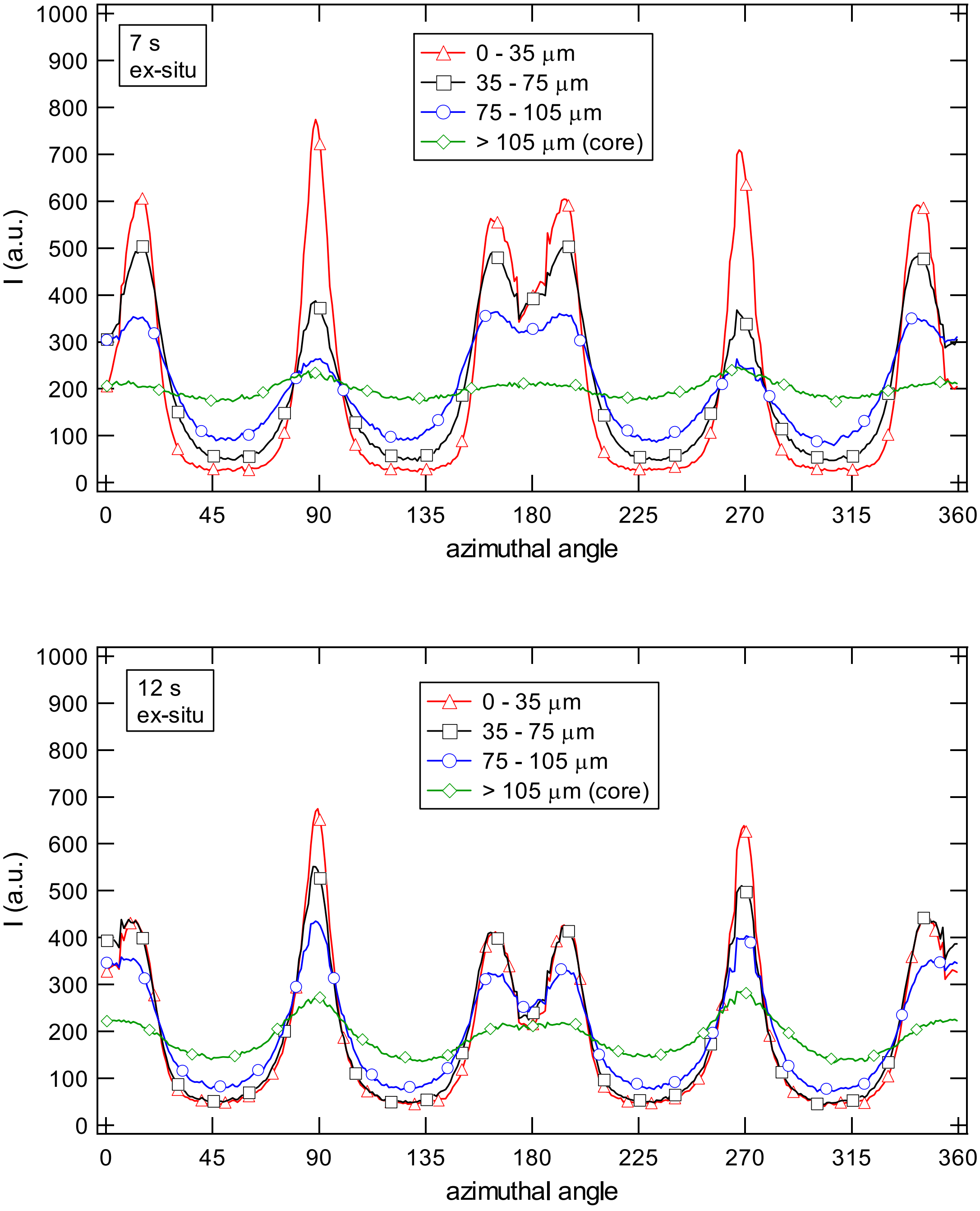

**Figure 3-11.** Ex-situ micro-diffraction patterns for $t_s$ = 12 s (top) and $t_s$ = 7 s (bottom) sheared at 137˚C

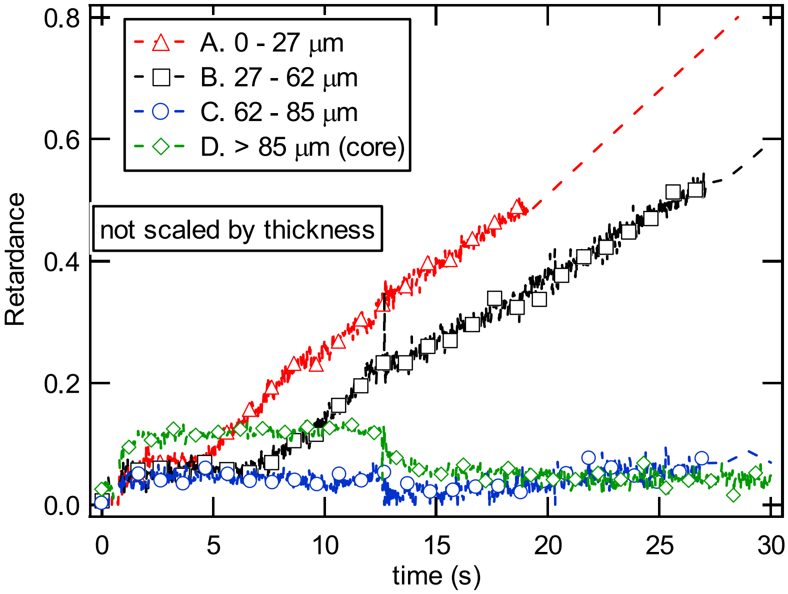

**Figure 3-12. Depth sectioning retardance for 12 s of shearing time at 137˚C. These data corresponds to the average birefringence depicted in Figure 3-3 top multiplied by the thickness of each depth slice.**

## 3.8 References

1. Liedauer, S., G. Eder, and H. Janeschitzkriegl. *On the Limitations of Shear-Induced Crystallization in Polypropylene Melts.* International Polymer Processing, 1995. **10**(3): 243-250.
2. Liedauer, S., G. Eder, H. Janeschitzkriegl, et al. *On the Kinetics of Shear-Induced Crystallization in Polypropylene.* International Polymer Processing, 1993. **8**(3): 236-244.
3. Kumaraswamy, G., R.K. Verma, A.M. Issaian, et al. *Shear-enhanced crystallization in isotactic polypropylene Part 2. Analysis of the formation of the oriented "skin".* Polymer, 2000. **41**(25): 8931-8940.
4. Kumaraswamy, G., R.K. Verma, and J.A. Kornfield. *Novel flow apparatus for investigating shear-enhanced crystallization and structure development in semicrystalline polymers.* Review of Scientific Instruments, 1999. **70**(4): 2097-2104.
5. Janeschitz-Kriegl, H., and G. Eder. *Basic Concepts of Structure Formation During Processing of Thermoplastic Materials.* Journal of Macromolecular Science-Chemistry, 1990. **A27**(13-14): 1733-1756.
6. Eder, G., H. Janeschitz-Kriegl, and S. Liedauer. *Crystallization Processes in Quiescent and Moving Polymer Melts under Heat-Transfer Conditions.* Progress in Polymer Science, 1990. **15**(4): 629-714.
7. Eder, G., and H. Janeschitz-Kriegl, *Crystallization*, In *Processing of Polymers*, H.E.H. Meijer, Ed. 1997, New York: Wiley-VCH.

8. Thurman, D.W., *Molecular Aspects of Flow-Induced Crystallization of Polypropylene*. 2005, California Institute of Technology.

9. Kornfield, J.A., G. Kumaraswamy, and A.M. Issaian. *Recent advances in understanding flow effects on polymer crystallization.* Industrial & Engineering Chemistry Research, 2002. **41**(25): 6383-6392.

10. Fuller, G.G., *Optical Rheometry of Complex Fluids*. 1995, New York: Oxford University Press.

11. Roe, R.J., *Methods of X-ray and Neutron Scattering in Polymer Science*. 2000, New York: Oxford University Press.

12. Dean, D.M., L. Rebenfeld, R.A. Register, et al. *Matrix molecular orientation in fiber-reinforced polypropylene composites.* Journal of Materials Science, 1998. **33**(19): 4797-4812.

13. Hongladarom, K., W.R. Burghardt, S.G. Baek, et al. *Molecular Alignment of Polymer Liquid-Crystals in Shear Flows .1. Spectrographic Birefringence Technique, Steady-State Orientation, and Normal Stress Behavior in Poly(Benzyl Glutamate) Solutions.* Macromolecules, 1993. **26**(4): 772-784.

14. Krishnan, K., F.S. Bates, and T.P. Lodge. *Shear alignment of a swollen lamellar phase in a ternary polymer blend.* Journal of Rheology, 2005. **49**(6): 1395-1408.

15. Chen, Z.R., J.A. Kornfield, S.D. Smith, et al. *Pathways to macroscale order in nanostructured block copolymers.* Science, 1997. **277**(5330): 1248-1253.

16. Becu, L., S. Manneville, and A. Colin. *Spatiotemporal dynamics of wormlike micelles under shear.* Physical Review Letters, 2004. **93**(1).

17. Berret, J.F., G. Porte, and J.P. Decruppe. *Inhomogeneous shear rows of wormlike micelles: A master dynamic phase diagram.* Physical Review E, 1997. **55**(2): 1668-1676.

18. Lee, J.Y., G.G. Fuller, N.E. Hudson, et al. *Investigation of shear-banding structure in wormlike micellar solution by point-wise flow-induced birefringence measurements.* Journal of Rheology, 2005. **49**(2): 537-550.

19. Hongladarom, K., and W.R. Burghardt. *Molecular Alignment of Polymer Liquid-Crystals in Shear Flows .2. Transient Flow Behavior in Poly(Benzyl Glutamate) Solutions.* Macromolecules, 1993. **26**(4): 785-794.

20. Fuller, G.G. *Optical rheometry of complex fluid interfaces.* Current Opinion in Colloid & Interface Science, 1997. **2**(2): 153-157.

21. Norman, A.I., W.H. Zhang, K.L. Beers, et al. *Microfluidic light scattering as a tool to study the structure of aqueous polymer solutions.* Journal of Colloid and Interface Science, 2006. **299**(2): 580-588.

22. Caputo, F.E., W.R. Burghardt, K. Krishnan, et al. *Time-resolved small-angle x-ray scattering measurements of a polymer bicontinuous microemulsion structure factor under shear.* Physical Review E, 2002. **66**(4).

23. Kumaraswamy, G., R.K. Verma, J.A. Kornfield, et al. *Shear-enhanced crystallization in isotactic polypropylene. In-situ synchrotron SAXS and WAXD.* Macromolecules, 2004. **37**(24): 9005-9017.

24. Somani, R.H., B.S. Hsiao, A. Nogales, et al. *Structure development during shear flow induced crystallization of i-PP: In situ wide-angle X-ray diffraction study.* Macromolecules, 2001. **34**(17): 5902-5909.

25. Somani, R.H., I. Sics, and B.S. Hsiao. *Thermal stability of shear-induced precursor structures in isotactic polypropylene by rheo-X-ray techniques with couette flow geometry.* Journal of Polymer Science Part B-Polymer Physics, 2006. **44**(24): 3553-3570.

26. Langouche, F. *Orientation development during shear flow-induced crystallization of i-PP.* Macromolecules, 2006. **39**(7): 2568-2573.

27. Lagasse, R.R., and B. Maxwell. *Experimental-Study of Kinetics of Polymer Crystallization During Shear-Flow.* Polymer Engineering and Science, 1976. **16**(3): 189-199.

28. Nogales, A., B.S. Hsiao, R.H. Somani, et al. *Shear-induced crystallization of isotactic polypropylene with different molecular weight distributions: in situ small- and wide-angle X-ray scattering studies.* Polymer, 2001. **42**(12): 5247-5256.

29. Kumaraswamy, G., A.M. Issaian, and J.A. Kornfield. *Shear-enhanced crystallization in isotactic polypropylene. 1. Correspondence between in situ rheo-optics and ex situ structure determination.* Macromolecules, 1999. **32**(22): 7537-7547.

30. White, H.M., and D.C. Bassett. *On variable nucleation geometry and segregation in isotactic polypropylene.* Polymer, 1997. **38**(22): 5515-5520.

## *Chapter IV*

# *Method of “Temperature-Jump”*

## 4.1 Introduction

Thread-like precursors are at the heart of flow-induced crystallization: They nucleate highly oriented crystallites and can increase the kinetics of crystallization by orders of magnitude. There is great interest in elucidating the process by which they form, and how their creation depends on parameters such as temperature, flow conditions, and material characteristics. Thus, measuring the amount of oriented precursors that form during flow, and how that quantity depends on molecular and processing parameters, is essential to developing a truly predictive model of flow-induced crystallization.

In order to obtain the experimental information to model the growth of shish, we must separate the effect of temperature on development of shish from the effect of temperature on lamellar overgrowth velocity. At the range of undercoolings usually employed in flow-induced crystallization experiments, kebab growth on the thread-like precursors is already observed during imposition of flow by WAXD [1]. In Chapter III of this thesis, we deduced that significant growth of kebabs on the oriented threads already occurred as they were being formed during shear at 137˚C. Therefore, it is important to create the precursors at a temperature high enough that negligible overgrowth occurs. However, the bare oriented precursors elude the sensitivity of quantitative techniques such as x-ray scattering. Here, we present a strategy that lays the groundwork for creating bare precursors separately from their overgrowth, and that will allow us to indirectly quantify the amount of precursors present. This work will constitute the basis for choosing the experimental conditions for the next chapter, where we combine the temperature jump method with the depth sectioning method (Chapter III) to gain insight on the process of development of thread during flow.

## 4.2 "T-jump" method

The "T-jump" approach (Figure 4-1) consists of first shearing the polymer at a relatively high temperature ($T_{shear}$) so that thread-like precursors are created by flow but lamellar overgrowth on them is negligible. To date, direct detection of the bare shish eludes the sensitivity limits of x-ray experiments. Therefore, to quantify these oriented threads we need to grow them to a detectable size using conditions such that the results are truly proportional to the length of precursors present. This is similar to quantitative nucleation studies in aerosol where conditions for nucleation were imposed for a certain time and then quickly removed, so that the nucleation process was terminated but growth on the already formed nuclei would proceed and could be detected [2, 3]. Prior polymer literature on melt memory provides a similar idea: Studies on the relaxation behavior of shish first create them at high temperatures and, after a certain annealing time, quickly cool the polymer melt down to conditions where oriented growth occurs off the shish that are present [4-6]. The development of oriented morphologies at lower temperatures was observed to be a very sensitive marker of whether there were oriented precursors present. These studies were used to deduce decay times of shish, but did not aim at quantifying them.

As discussed in Chapter II, we have a method to create thread-like precursors under controlled conditions (shear stress $\sigma_w$, shearing time $t_s$, shearing temperature $T_{shear}$) [7] and using model polymers with well-defined molecular structure (e.g., specific $M_L/M_S$ and $C_L$). Here we add to this method an approach to create those shish and grow kebabs in a way such that the measurable signal that arises is proportional to the shish length. After imposing a short shear pulse and a given holding time ($t_{hold}$) at a fairly high $T_{shear}$, the polymer melt is cooled down to $T_{growth}$ so that significant development of kebabs occurs with the corresponding lamellar quiescent velocity (Figure 4-1). For the signal due to the growing kebabs to be proportional to the total thread-length present, any kebab overgrowth during shear must be negligible. After cessation of shear, the thermal history must be reproduced for different experiments, particularly in the range of cooling where lamellar growth starts occurring at observable rates, so that the comparison is meaningful. Finally, the threads formed during flow must be sufficiently long; then, the growth occurring on the end-caps can be safely neglected. If these conditions hold, then before the lamellae growing off neighboring threads begin to impinge with one another, the rate of growth of kebabs on the threads can be used as an indirect measurement to deduce the amount of thread-length (Figure 4-2).

The choice of adequate $T_{shear}$ and $T_{growth}$ is important to obtain meaningful results. $T_{shear}$ must be high enough that no significant kebab growth occurs, but not so high that oriented precursor formation is inhibited, or that the created threads relax completely before we are able to cool down to the growth temperature. The choice of $T_{growth}$ is more practical in nature: Significant crystallization must occur at reasonable times, and the choice may be limited by the heat transfer capabilities of the shear apparatus.

In the following, we investigate the issues above: The temperature range where the signature for oriented precursor formation is observed, and the relaxation behavior of the threads when shearing above their melting point.

## 4.3 Experimental

### 4.3.1 Materials

A blend of 1% weight of long chains ($M_w$ = 3500 kg/mol) in a matrix of shorter chains ($M_w$ = 186 kg/mol) was used. Detailed characteristics of each component and the blending procedure are given in Chapter II.

### 4.3.2 Shear-induced crystallization apparatus and protocol

Flow-induced crystallization experiments were performed in an apparatus [7] capable of imposing a strong shear pulse onto a polymer melt for a brief duration of time and under well-known thermal conditions (same as in Chapter II). The experimental protocol is shown in Figure 4-1. First the melt is introduced into the flow cell with a low shear stress at 215˚C and is held there for 5 minutes to erase the previous thermal and flow histories. The polymer is then cooled down to the shearing temperature ($T_{shear}$) where a strong shear pulse corresponding to a given wall shear stress ($\sigma_w$) is applied for a specified shearing time ($t_s$). After cessation of flow, the polymer is held at $T_{shear}$ for a particular time ($t_{hold}$), and afterwards the flow cell is cooled down to the chosen growth temperature ($T_{growth}$) so that the process of crystallization can be monitored. Rheo-optical data is acquired in real time from the moment that the shear is imposed on the sample.

In the experiments described in this chapter, the imposed wall shear stress was $\sigma_w$ = 0.072 MPa at $T_{shear}$s ranging from 140˚C to 215˚C, with varying shearing times and the same total extruded amount (~ 100 mg). The holding time at $T_{shear}$ was 1 min, after which the cool down process was started until the final temperature of 140˚C was reached. In practice, the temperature stayed at $T_{shear}$ for about two minutes before decaying due to the high thermal mass of our apparatus. Note that the experiment where shear is performed at 140˚C is actually the only one performed under isothermal conditions. All experiments had a duration of 60 minutes from the moment shear was imposed, after which the sample cell was removed and cooled down to ambient temperature for sample extraction.

### 4.3.3 In-situ rheo-optical measurements (polarimetry and turbidity)

Real-time polarimetry and turbidity were obtained during and after shear; the instrumentation for these measurements is described in Chapter II and in reference [7].

### 4.3.4 Ex-situ polarized optical microscopy (POM)

Sections from the quenched samples in the flow-velocity gradient plane ($\mathbf{v}$-$\nabla\mathbf{v}$) were imaged with polarized optical microscopy (POM), as described in Chapter II.

### 4.3.5 Ex-situ WAXD

Wide angle x-ray diffraction (WAXD) patterns of selected extracted samples were obtained. Details of the experimental setup and data analysis are explained in Chapter II.

## 4.4 Results

The 1% blend clearly showed the development of an upturn in the birefringence during shear for all temperatures from 140˚C up to 215˚C for $\sigma_w$ = 0.072 MPa (Figure 4-3).

This material was chosen to study the occurrence of upturns during flow because our previous study (Chapter II) showed that a highly oriented skin can be induced when intermediate shear stresses are imposed, and because it did not present a large overshoot upon inception of shear. These two features assist in detecting the upturn when it happens, If a large overshoot was present it could mask the occurrence of a small upturn. At high shearing temperatures and high applied stresses, the limit for extruded polymer mass in our apparatus (~ 100 mg) is reached at very short shearing times, for which an upturn would be hard to distinguish.

The two lowest shearing temperatures (140˚C and 160˚C) present significantly different behavior from the rest after cessation of flow: The birefringence never relaxes completely back to its initial value before the shear pulse (Figure 4-4). For 140˚C, the growth of birefringence starts immediately after cessation of shear, while for 160˚C a large residual value remains during the 1 minute of holding time and begins increasing shortly after cooling is started.

The time for the upturn ($t_u$) to start during shear decreases with increasing temperature from 140˚C to 185˚C; at $T_{shear} \geq 185$˚C, it remains fairly constant (Figure 4-5). A comparison with the rheological shift factor, $a_T$, shows that $t_u$ follows the same temperature dependence up to 185˚C. At greater $T_{shear}$s, the deviation is positive: It takes longer to see the upturn than simply following the $a_T$ trend.

The results during and immediately after shear have two distinguished ranges of behavior: $T_{shear} \leq 160$˚C and $T_{shear} \geq 180$˚C. Next we consider the results at longer times when cooling has already been performed, as well as the final solid-state morphology. Three different ranges can be distinguished with these criteria.

- Region 1 (140˚C-185˚C): Upon cooling the crystalline growth shows significant amounts of oriented growth; the real time birefringence goes over orders (Figure 4-6, top left). The amount of orientation observed is smaller for the higher shearing temperatures; 180˚C and 185˚C go over the first maximum in birefringence much slower than 140˚C and 160˚C. The transmittance decays quite rapidly during the experimental time (Figure 4-6, top right). Ex-situ polarized optical microscopy reveals that highly oriented skin has formed near the wall, as well as some isolated oriented sausages at lower shear stresses (Figure 4-7, top). Consistently, the ex-situ WAXD patterns show that a large quantity of highly oriented α crystallites are present in the sample (Figure 4-7, top right).

- Region 2 (190˚C-200˚C): No significant orientation occurs during the experimental time; the real-time birefringence does not show any growth (Figure 4-6, middle left). However, kinetics are accelerated to some extent compared to the quiescent case because turbidity does decay before extracting the sample after an hour (Figure 4-6, middle right). Some isolated hairy sausages with oriented growth are visible in the optical micrographs at varying distances from the wall (Figure 4-7, middle left), but there is no highly oriented skin. The rest of the sample looks isotropic. Ex-situ WAXD confirms that there is some slight orientation, but most of the sample contributes with isotropic scattering (Figure 4-7, middle right).

- Region 3 (205˚C-215˚C): Similarly to Region 2, there is no growth of birefringence at all during the experiment (Figure 4-6, bottom left). However, the overall kinetics are much slower; turbidity does not decay at all during the extent of the experiment (Figure 4-6, bottom right). The OPM shows only spherulitic structures; there is no trace of any highly oriented skin or of isolated oriented sausages (Figure 4-7, bottom left). For the case of 215˚C, large spherulites covering the entire sample are clearly visible. Finally, ex-situ WAXD shows that only isotropic crystallites are present (Figure 4-7, bottom right).

In the case of Region 1 optical micrographs show that the density of the skin is lower for the 180˚C and 185˚C sections than for 140˚C and 160˚C (Figure 4-8). This is particularly evident in the bottom row where, for 140˚C and 160˚C, the skin region appears completely dark (while for the other two, some intensity is transmitted).

## 4.5 Discussion

One of the most important features of the results is that they show that $T_{shear}$ should be above 160˚C to avoid kebab growth at $T_{shear}$, and indicate that $T_{shear}$ up to at least 215˚C (the highest tested) permit shish to be induced by shear at a stress of 0.072 MPa. However, the shish completely decay away within minutes after cessation of flow for $T \geq 205$˚C. Thus, the results show that T-jump measurements may be used over a significant T-range (at least 170˚C to 200˚C) to probe the effects of temperature, stress, and molar mass distribution on the formation and decay of threadlike precursors in iPP. An apparatus capable of rapid cooling would give access to information from 190˚C-200˚C; the heat transfer limitations of the present apparatus restrict the feasible shearing temperatures to the 170˚C-185˚C range.

### 4.5.1 Creation of precursors

We interpret the upturn in birefringence during flow in light of previous investigations that revealed that the upturn was the signature of formation of long-lived oriented precursors of crystallization, even when observed above the nominal melting temperature [1]. Kumaraswamy et al. observed the upturn in the shear pulse up to temperatures of 175˚C for iPP (higher temperatures were not investigated). Our data indicates that oriented precursors can be formed at least up to 215˚C. This is in agreement with studies on melt memory after shear of isotactic polypropylene: Janeschitz-Kriegl and coworkers observed that shearing at temperatures as high as 210˚C could produce highly oriented structures upon rapid cooling, thus revealing that oriented nuclei had been formed during flow [4].

The time at which we observe the upturn follows the same temperature dependence as the rheological shift factor for iPP up to 185˚C, in accordance to the results from reference [1], in which the highest temperature tested was 175˚C. Our study further extends the range of investigated temperatures, revealing a positive deviation of the temperature dependence at $T_{shear}$ > 170˚C. This suggests that the decay timescale for the precursors may be fast enough at those temperatures to occur to certain extent during shear, depleting the population of shish as they are being formed. The inclusion of the decay of oriented precursors at high temperatures can have implications on the accurate prediction of the kinetics of crystallization and morphology development. Often times, the conditions used in experiments employ large undercoolings such that they render the decay time effectively very large. However, in industrial processes (such as injection molding, fiber spinning, and film blowing), deformation of a polymer fluid element while it is at large temperatures (up to ~ 240˚C) and thereafter, as it is cooling, all contribute to the final precursor population, which only becomes manifest when the fluid element cools to ~ 160˚C and below. Therefore, a truly predictive model must account for effects of deformation even at high temperatures of shear which were previously regarded as irrelevant to flow-induced crystallization. The models for flow-induced crystallization of Janeschitz-Kriegl [8], and of the Eindhoven group [9], are prepared to account for the decay of both point-nuclei and thread-nuclei already formed with a decay rate which depends on a characteristic time.

### 4.5.2 Decay of threads after cessation of flow

The observation of a range of $T_{shear}$ (205˚C-215˚C) for which we see the signature for creation of oriented precursors, yet we do not observe any oriented growth upon cooling and ex-situ, indicates that the formed threads must have relaxed completely by the time the polymer was cooled down. It is well known that oriented precursors can survive at temperatures above the nominal melting point (~ 170˚C for iPP) for some time. At temperatures lower than that, shish do not decay. Above that temperature, the decay time quickly becomes faster at higher temperatures, reaching very small values near the equilibrium melting point (which for iPP is ~ 212˚C [10]). For $T_{shear} \geq$ 205˚C, the decay time of threads can be inferred to be < 180 s (which is the minimum amount of time that elapses from the imposition of shear to the moment at which the polymer melt has actually cooled down to temperatures at which the decay time diverges).

In contrast to the highest temperatures, the precursors formed between 190˚C-200˚C are annihilated significantly within 100 s, but a few threads are able to survive. We note that these few threads are not located near the wall where the shearing stress was highest, but at varying distances from the mold wall. This suggests that most of the highly oriented precursor population, which will be created in the regions of higher stress, decays within the annealing time at $T_{shear}$, but that a handful of shish have, by chance, greater stability. At temperatures 205˚C or above, even if particularly stable threads were formed, they relaxed completely. The existence of exceptional shish provides a cautionary note: In order to understand the formation of highly oriented structures and the concomitant change in material properties, methods are needed to discriminate between the prolifically formed shish (which correlate with the birefringence upturn) and the scant oriented structures that can be observed ex-situ.

It is a delicate matter to compare the decay times of the threadlike precursors observed here with those reported previously by Alfonso and Scardigli [5] and Eder et al. [4]. In Alfonso's "fiber pull" experiments, the criterion for decay was the absence of any transcrystalline growth—meaning that not even one of the most stable shish survived. With this criterion remarkably long times were observed in iPP: ~ 1200 s at 190˚C and 60 s at 210˚C. In contrast, Janeschitz-Kriegl's criterion for survival was the thickness of a highly oriented skin. His group reported a decay time of approximately 58 s at 190˚C, ~ 7 s at 200˚C, and < 1 s at 210˚C. The stark difference in decay timescales between the two studies is unlikely to be due to difference in iPP materials: Both groups used Ziegler-Natta iPP; Alfonso with $M_w$ from 400 to 520 kg/mol and $M_w/M_n$ from 6 to 25 and [mmmm] of 96% or 98%, while Janeschitz-Kriegl used a highly isotactic PP of $M_w$ = 330kg/mol and $M_w/M_n = 6$. Our results are consistent with both studies: The high concentration of shish decays away in less than 300 s at $T \geq 190$˚C and the most stable shish can survive for minutes at temperatures up to 200˚C. This similarity is interesting given that the present material is a bimodal blend of iPPs prepared using single-site catalysts.

At $T_{shear} \geq 205$˚C, no threads and no significant population of point-like nuclei survive: The turbidity does not decay while cooling and holding at 140˚C, and the final morphology consists of relatively large spherulites that form after extracting the sample and cooling to ambient temperature. Their size and homogeneity suggests that they have started growing at temperatures not too far below 140˚C, where only small numbers of nuclei appear but where linear lamellar growth rates can rapidly approach large values, so that spherulites from those few nuclei fill all the space. We infer that no significant quantities of point-like nuclei survive between 190˚C-200˚C, given that the few threads that remain are able to grow "sausages" of large diameter (~ 50-60 μm) without encountering spherulites growing from point-nuclei in the neighborhood. We attribute the decay of turbidity while holding isothermally at 140˚C to the growth of these sausage-structures.

At 180˚C and 185˚C, negligible growth of kebabs occurs. The relaxation rates of precursors formed are slow enough that many of them survive the temperature jump, and a highly oriented skin forms upon cooling. These two temperatures would therefore be within the range adequate for the purpose of the T-jump experiments. Finally, for the two lowest temperatures (140˚C and 160˚C), the thread-like precursors do not decay at all: at these temperatures kebab growth can already occur.

## 4.6 Conclusion

In summary, the results presented in this chapter lay the ground for choosing the T-jump conditions under the heat transfer limitations inherent to our experimental apparatus. Shearing temperatures at and above 190˚C will not be suitable for our purpose of performing temperature jumps to determine the thread-length/volume formed during flow, since they will decay too rapidly and we will not have any oriented threads left to study, while temperatures of 160˚C and below do not allow dissection of the effect of growth of threads from the growth of kebabs. For the next chapter, we have thus chosen an intermediate temperature (170˚C), at which we apply a variety of shearing stresses for different durations of shearing times. In this way, we effectively interrupt flow at selected times after the onset of shish formation and then obtain quantitative measurements of the total thread-length present by cooling to temperatures where growth of kebabs occurs and can be experimentally measured.

## 4.7 Figures

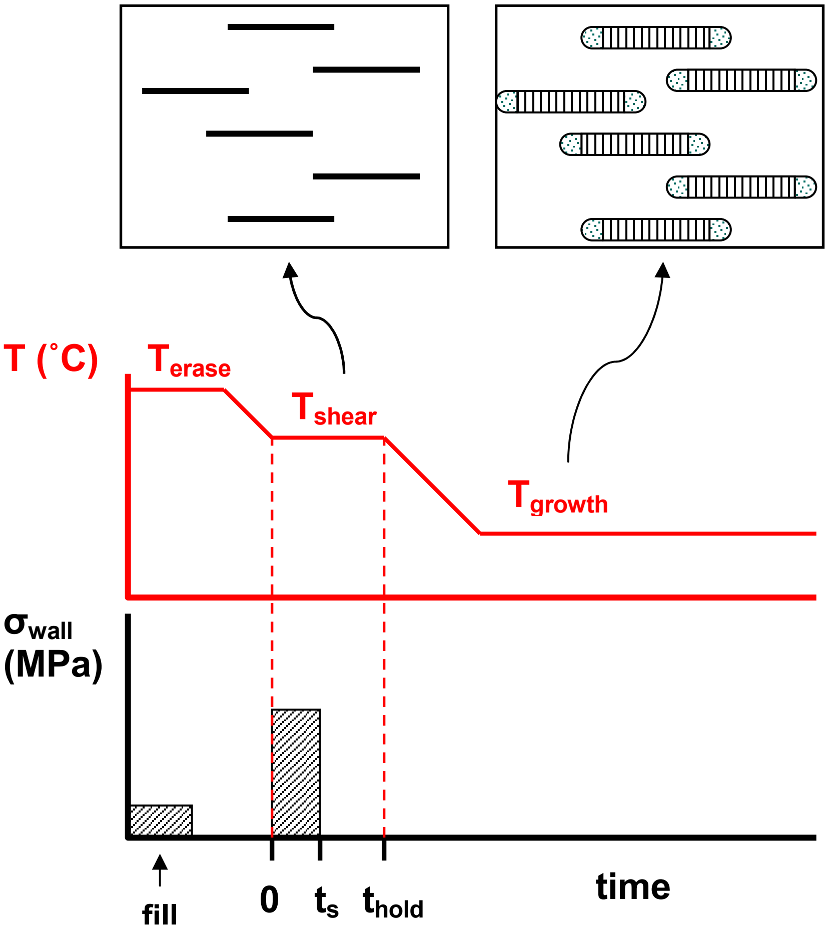

Figure 4-1. Experimental temperature and shear protocol for the "T-jump" method. The polymer melt is sheared at a temperature where negligible lamellar overgrowth occurs. Afterwards, it is cooled down to a temperature where the amount of kebab development is large enough to be detected. Before impingement has occurred, the signal arising from the kebab growth is proportional to the thread-length present.

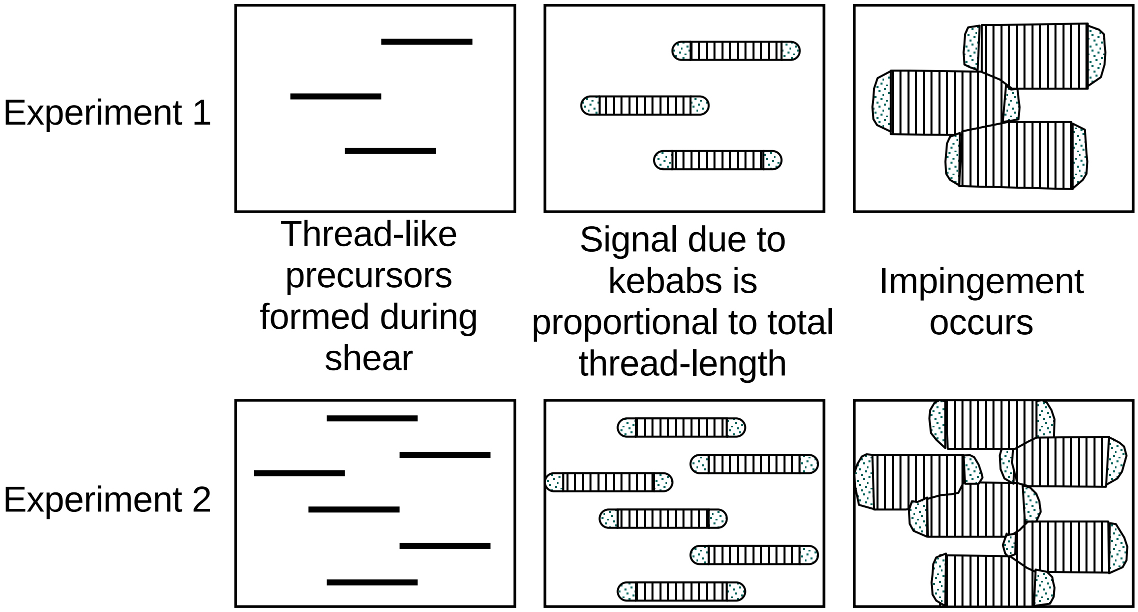

**Figure 4-2. Schematic showing the conditions under which the observable signal due to growth of kebabs on the threads is proportional to the total thread-length created during flow. Experiment 1 and 2 differ in the total thread-length present; before impingement, the kebab arising from the growth of kebabs serves to "read out" the relative amounts of shish present.**

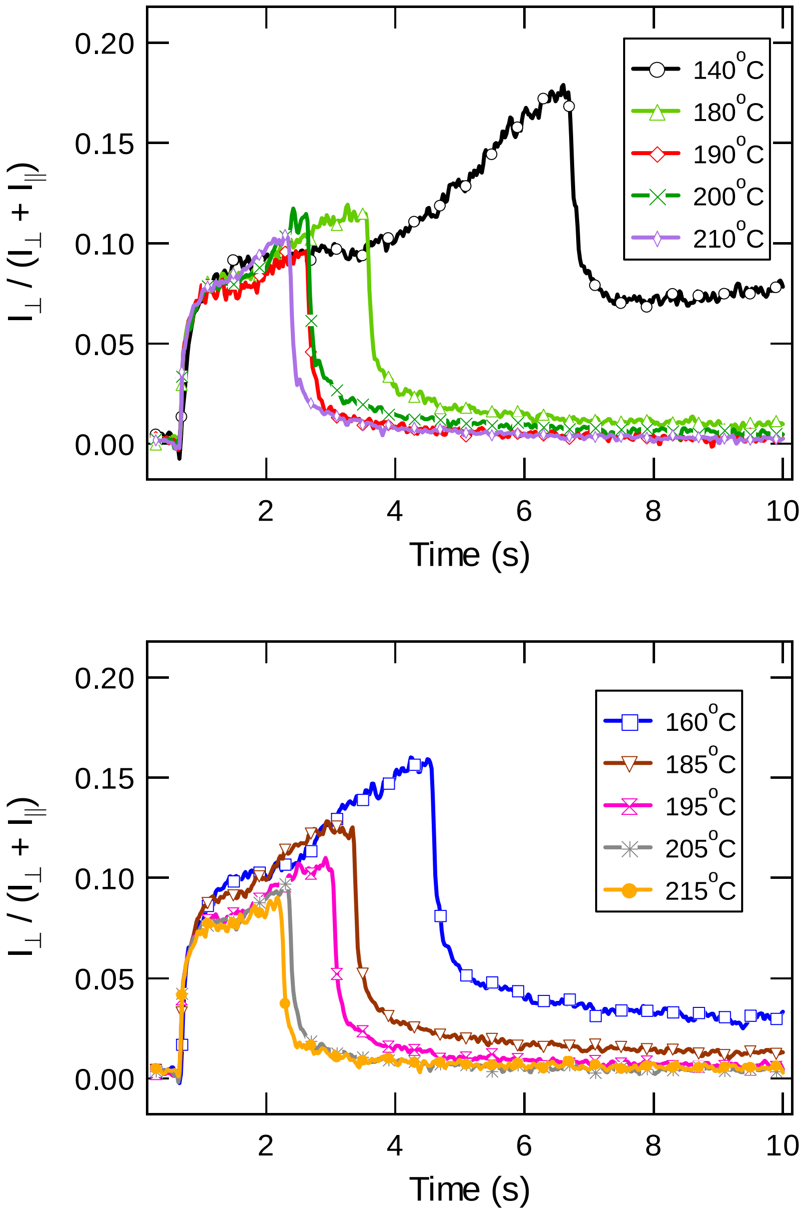

**Figure 4-3. Close-up of real-time birefringence measurements during and right after shear**

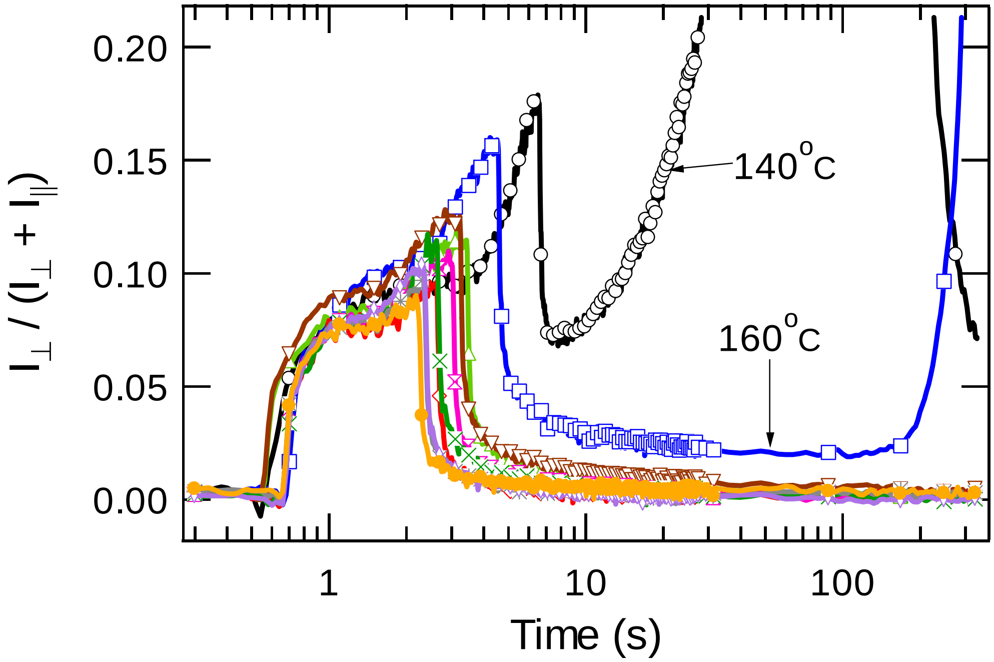

**Figure 4-4. Birefringence measurements at early times in the experiment showing that 140˚C and 160˚C birefringence never decays completely and starts growing right after shear for 140˚C and shortly after beginning of cooling for 160˚C**

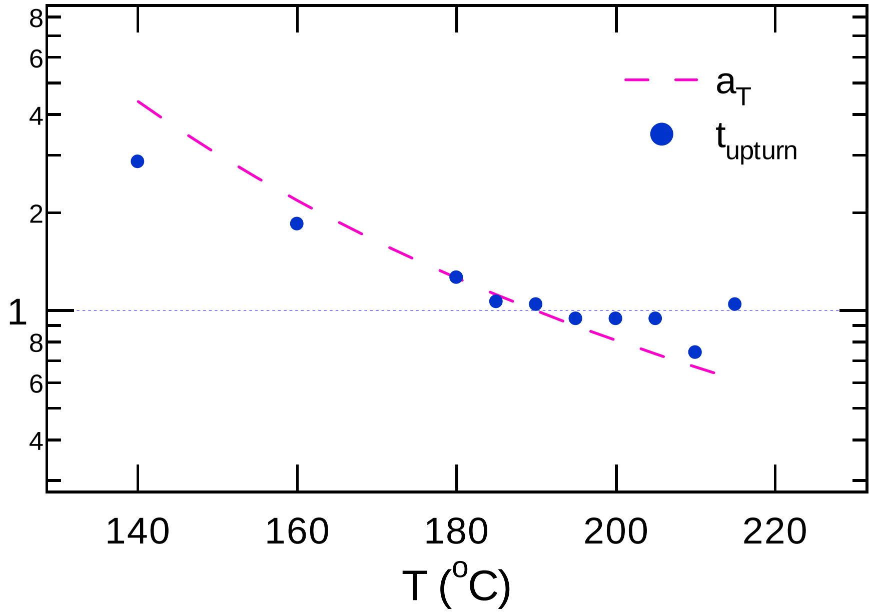

**Figure 4-5. Time for upturn ($t_u$) for different $T_{shear}$ and temperature dependence of the rheological shift factor for iPP, $a_T$**

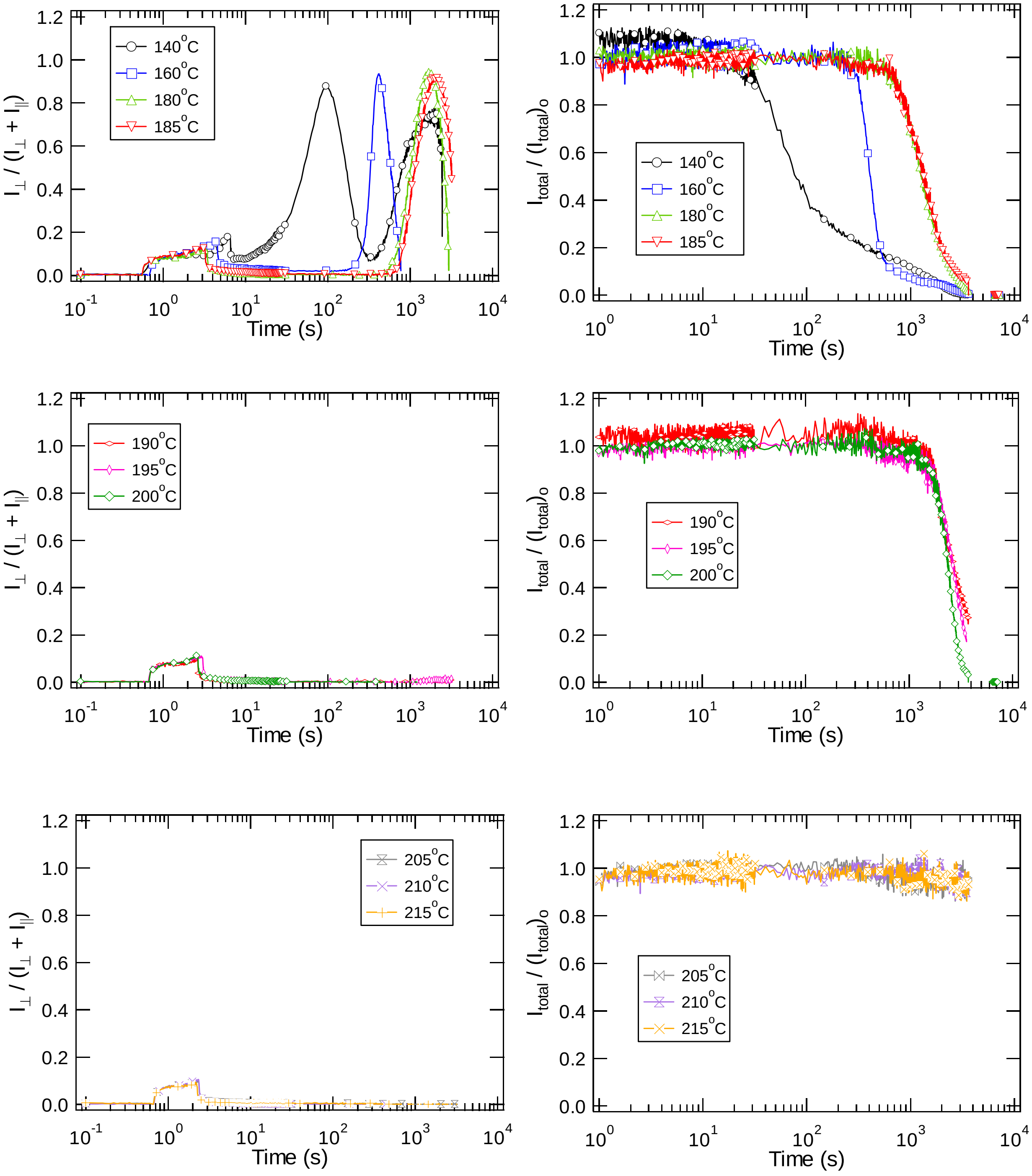

Figure 4-6. Real-time birefringence (left column) and turbidity (right column) for $T_{shear}$ between 140˚C-185˚C (top row), 190˚C-200˚C (middle), and 205˚C-215˚C (bottom)

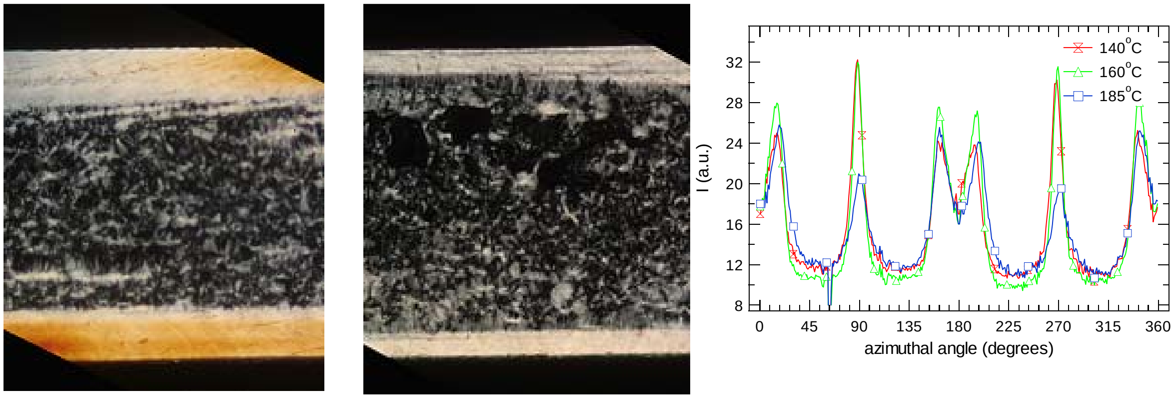

160˚C 185˚C

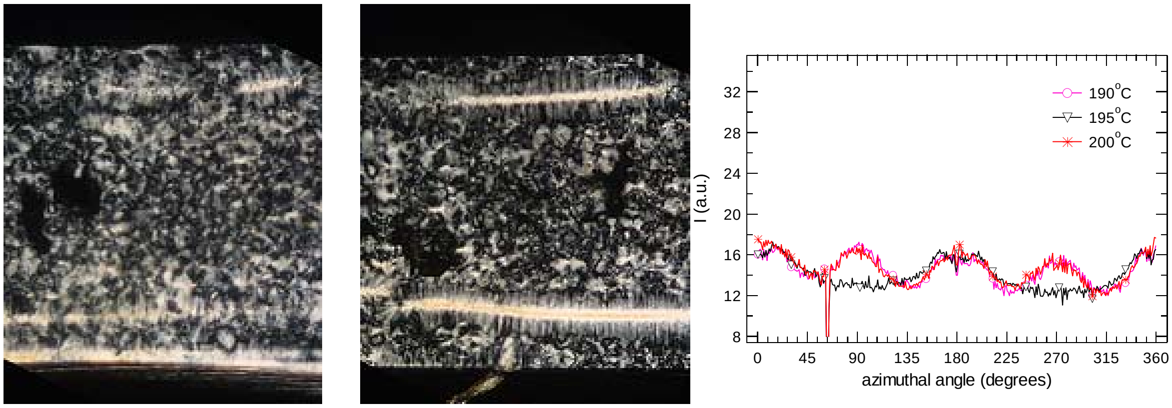

190˚C 200˚C

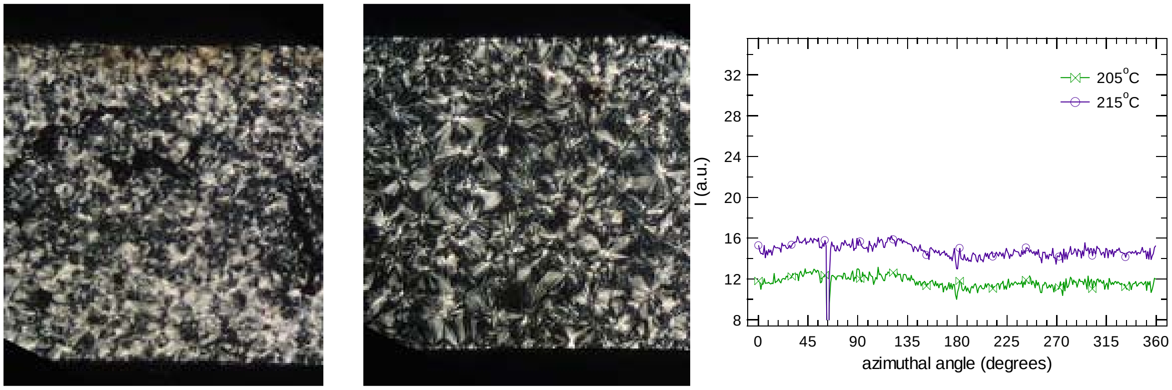

205˚C 215˚C

**Figure 4-7.** Optical polarized micrographs (left and middle columns) and ex-situ WAXD azimuthal (110) patterns (right column)

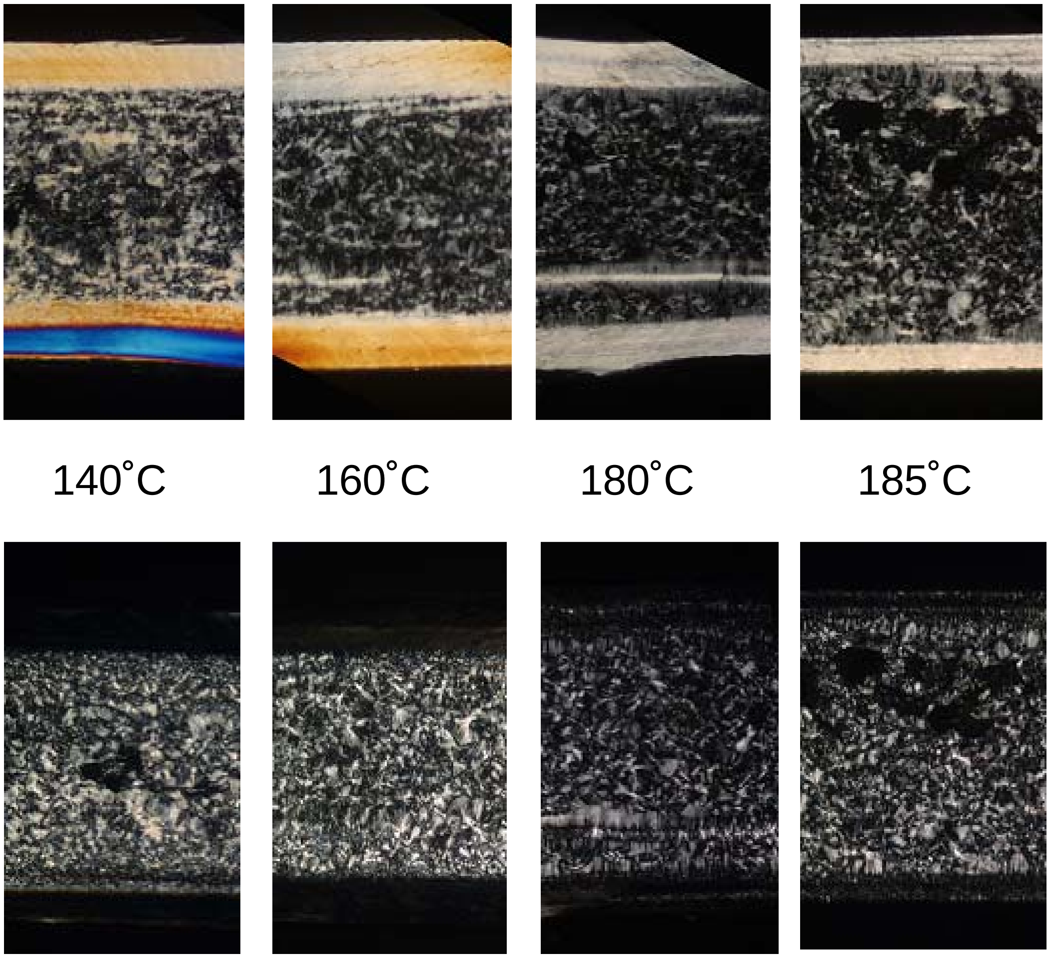

**Figure 4-8. Optical polarized micrographs with polarizer (P) and analyzer (A) at 45° and -45° to the flow direction (top row), and with P and A along and perpendicular to flow (bottom)**

## 4.8 References

1. Kumaraswamy, G., J.A. Kornfield, F.J. Yeh, et al. *Shear-enhanced crystallization in isotactic polypropylene. 3. Evidence for a kinetic pathway to nucleation.* Macromolecules, 2002. **35**(5): 1762-1769.
2. Wagner, P.E., and R. Strey. *Homogeneous Nucleation Rates of Water-Vapor Measured in a 2-Piston Expansion Chamber.* Journal of Physical Chemistry, 1981. **85**(18): 2694-2698.
3. Seinfeld, H.S., and S.N. Spiros, *Atmospheric Chemistry and Physics*. 1998, New York: John Wiley and Sons, Inc. .
4. Eder, G., H. Janeschitz-Kriegl, and S. Liedauer. *Crystallization Processes in Quiescent and Moving Polymer Melts under Heat-Transfer Conditions.* Progress in Polymer Science, 1990. **15**(4): 629-714.
5. Alfonso, G.C., and P. Scardigli. *Melt memory effects in polymer crystallization.* Macromolecular Symposia, 1997. **118**: 323-328.
6. Azzurri, F., and G.C. Alfonso. *Lifetime of shear-induced crystal nucleation precursors.* Macromolecules, 2005. **38**(5): 1723-1728.
7. Kumaraswamy, G., R.K. Verma, and J.A. Kornfield. *Novel flow apparatus for investigating shear-enhanced crystallization and structure development in semicrystalline polymers.* Review of Scientific Instruments, 1999. **70**(4): 2097-2104.

8. Liedauer, S., G. Eder, H. Janeschitz-Kriegl, et al. *On the Kinetics of Shear-Induced Crystallization in Polypropylene.* International Polymer Processing, 1993. **8**(3): 236-244.

9. Zuidema, H., G.W.M. Peters, and H.E.H. Meijer. *Development and validation of a recoverable strain-based model for flow-induced crystallization of polymers.* Macromolecular Theory and Simulations, 2001. **10**(5): 447-460.

10. Xu, J.N., S. Srinivas, H. Marand, et al. *Equilibrium melting temperature and undercooling dependence of the spherulitic growth rate of isotactic polypropylene.* Macromolecules, 1998. **31**(23): 8230-8242.

*Chapter V*

# *Development of the Oriented Precursors During Flow*

## 5.1 Introduction

The fundamental goal underlying flow-induced crystallization studies is to obtain fundamental knowledge to develop models that can predict, based on the polymer material characteristics and the imposed processing conditions, the ensuing crystallization kinetics and the final morphology and ultimate material properties obtained. Many of the empirical models developed until now rely on a number of adjustable parameters that are specific to a particular type of processing or experimental data [1-3]. In addition, they do not capture morphology formation nor take into account its impact in the determination of crystallization kinetics. In contrast, a model developed by Eder and coworkers [4] does try to capture the effect of nucleation morphology (point-like nuclei and thread-like nuclei) on the subsequent structure evolution after flow is imposed, but is based on flow kinematics (dependence on the shear rate) rather than on flow dynamics. Recently, pioneering work by the group of Meijer in Eindhoven [5] that is being extended currently has modified the model of Eder, incorporating the of molecular orientation under flow and attempting to incorporate the physics of oriented precursor formation. However, experimental data that provides an understanding of that mechanism and that can be tested against model predictions must be acquired. In this chapter, we present measurements aimed at fulfilling this necessity. We combine the temperature jump method (Chapter IV) and the depth sectioning method (Chapter III) to a series of thoughtfully selected conditions for a particular model polymer (containing 1% of 3.5M long chains) to gain insight into the development of the thread-like precursors and their dependence on the applied level of stress.

## 5.2 Experimental

### 5.2.1 Materials

A blend of 1% weight of long chains ($M_w$ = 3500 kg/mol) in a matrix of shorter chains ($M_w$ = 186 kg/mol) is studied. Detailed characteristics of each component and a description of the solution blending procedure are given in Chapter II.

### 5.2.2 Shear-induced crystallization apparatus and protocol

Flow-induced crystallization experiments were performed in an apparatus [6] capable of imposing a strong shear pulse onto a polymer melt for a brief duration of time and under well-known thermal conditions (same as in Chapter II). The experimental protocol consist of a T-jump, which is described in the previous chapter. In the experiments described in this chapter, several wall shear stresses $\sigma_w$ (between 0.069 MPa and 0.111 MPa) were imposed for different shearing times (ranging from 0.3 s to 3.5 s). The temperature chosen to impose the shear pulse was 170˚C, because it belongs to the range of $T_{shear}$ where no significant kebab growth occurs during flow, but the oriented structures, if formed, do not decay rapidly. The melt was at $T_{shear}$ for 1 min after shear, after which it was cooled down to 140˚C and held isothermally at that temperature for 40 minutes.

### 5.2.3 In-situ rheo-optical measurements

Real-time polarimetry and turbidity were obtained during and after shear; the instrumentation for these measurements is described in Chapter II and in reference [6].

### 5.2.4 In-situ small angle X-ray scattering (SAXS)

Real-time 2D SAXS patterns were acquired at BM26b (DUBBLE) of the ESRF (Grenoble, France). A 2D gas-filled multi-wired detector was placed 6.7 m from the sample to collect the SAXS patterns. Rat tail was used to calibrate the camera length. An evacuated tube was placed between the sample and the detector to minimize air scattering.

## 5.3 Results

### 5.3.1 Real-time polarimetry measurements

During shear, much of the observed birefringence is due to the stress-optical contribution of the polymer melt, making it difficult to infer how much of the signal is due to the oriented precursors. Upon cessation of flow, the melt birefringence decays rapidly, exposing the oriented structures generated during flow. At the lowest stress 0.069 MPa (Figure 5-1, bottom left) and the shorter shearing times ($t_s \leq 2.5$ s), there is little, if any, long-lived birefringence after cessation of flow. The longest two shearing times show a distinct residual birefringence (~ 0.10) after shear is stopped. The strength of the oriented precursor contribution to the birefringence just after flow correlates very well with the growth of oriented crystallites upon subsequent cooling (Figure 5-1, bottom right). The two long shearing times template sufficient oriented growth that the retardance reaches the first order (peak) at approximately 550 s (when the temperature has fallen to ~ 140˚C) and proceeds to pass through the second order. In contrast, the shorter shearing times produce much lower amounts of oriented precursors—only the $t_s = 2.5$ s reaches even the first order. Moving to greater $\sigma_w$, we observe that for each shearing stress, the longest shearing times show the development of many highly oriented structures upon cooling (the birefringence goes over orders). The shearing time required to produce such highly oriented growth is larger for smaller wall shearing stresses: At the highest stress $\sigma_w = 0.110$ MPa, the birefringence goes over orders for $t_s = 1.0$ s, while for the lowest stress 0.069 MPa it is necessary to shear for at least 3.0 s (Figure 5-1). Note that at 0.110 MPa, the transition between no oriented growth and the birefringence going over orders is very abrupt: Compare the behavior at $t_s = 0.5$ s and 1.0 s. The rest of wall shear stresses also show this transition, but it becomes more gradual with decreasing $\sigma_w$. For instance, note the slow change in birefringence development for 0.069 MPa between $t_s = 1.5$ s and 3.0 s.

For each wall shear stress, we note that the growth of birefringence over the experiment becomes very similar for the longest shearing times used (the signal reaches the first order peaks at similar times), suggesting that some saturation effect takes place: Beyond a certain duration of $t_s$, a further increase in shearing time has little effect.

Under our conditions, we can qualitatively predict the amount of oriented growth that will occur upon cooling by noting the residual birefringence after the shear pulse. Note that at 0.110 MPa (Figure 5-1, top left), both $t_s$ = 1.0 s and 1.5 s have approximately the same long lived birefringence after cessation of flow (~ 0.103); later the birefringence growth upon cooling is very similar. Likewise, $\sigma_w$ = 0.098 MPa (Figure 5-1, second row left) has similar residual birefringence for 1.5 s and 2.0 s (~ 0.095) and similar subsequent growth. The comparison of experiments performed at different shearing stresses but with similar oriented growth a long time after flow also reveals that their respective residual birefringence after the shear pulse is similar; for instance, the residue for 0.084 MPa and $t_s$ = 1 s and for 0.069MPa and $t_s$ = 2.5 s is approximately the same (~ 0.07).

We examined closely all optical experiments to deduce the highest temperature during cool down at which the development of oriented structures could be detected. The earliest rise of birefringence above its residual value was observed at a temperature of ~ 162˚C.

### 5.3.2 Real-time SAXS

#### 5.3.2.1 Pattern development

The real-time SAXS measurements do not detect structure development during shear or right after when holding the polymer melt at 170˚C for 1 min. A representative progression of real-time 2D patterns under conditions that developed highly oriented growth upon cooling ($\sigma_w$ = 0.092 MPa applied for $t_s$ = 1.5 s, Figure 5-2) shows a faint equatorial streak (in the vertical direction). In the meridional region, a strong peak appears first at low q ($q_1 \sim 0.125$ nm$^{-1}$, near the beamstop), and at later times a second peak appears at higher q ($q_2 \sim 0.16$ nm$^{-1}$). The progression of intensity vs. scattering vector in a thin meridional sector (Figure 5-3) shows that the first peak at $q_1$ increases in intensity strongly while the sample is cooled to 140˚C. As the temperature approaches 140˚C, the intensity at higher q than $q_1$ increases steadily (Figure 5-3, 10-16 min). After isothermal growth conditions at 140˚C are reached, the intensity at high q ($q_2$) continues to increase slowly (Figure 5-3, 16-35 min). Over longer periods of time (Figure 5-3, 21-55), the peak at $q_1$ decreases slightly and shifts mildly towards greater values of q. The behavior shown above is representative of the progression of SAXS patterns in all cases of strongly oriented growth. The highest temperature at which the peak at $q_1$ could be clearly detected during cooling was ~ 146˚C.

To compare the suite of different $\sigma_w$ and $t_s$, we examine the meridional peaks in two ways (Figure 5-4, top): First, the intensity of the peaks at $q_1$ and $q_2$ are individually quantified; and second, the overall population of oriented lamellae is monitored using the total intensity enclosed within a rectangular group of pixels that includes the peaks at $q_1$ and $q_2$ ($I_{mer}$). To compute the intensity of the peaks at $q_1$ and $q_2$ individually, azimuthal scans at each wavevector are analyzed (Figure 5-4, bottom). The azimuthal scans revealed that the isotropic contribution to scattering is negligible (even at long times the minima are very nearly zero) for our experimental conditions. A small and broad increase in intensity was observed in the equatorial region (0˚ and 180˚, Figure 5-4 bottom) as the sample crystallized, attributed to crosshatched daughter lamellae. Given the very small populations of isotropic lamellae and daughter lamellae, the most important features are the strength and angular distribution of the scattering from the parent lamellar stacks, which grow perpendicular to the direction of flow (observed at 90˚ and 270˚ in the azimuthal scans of Figure 5-4, bottom). These are characterized by fitting the parent peaks with Lorentzian functions to extract an amplitude and the full width half max for each meridional peak.

The inner peak ($q_1$) intensity is observed to consistently start growing at earlier times (Figure 5-5, left column) than the outside peak at $q_2$ (Figure 5-5, middle column). The inner peak grows rapidly to high intensities and then either plateaus (for the weaker flow conditions) or decreases slightly (for the strongest conditions). Approximately 5-10% of the maximum intensity develops by the time the temperature reaches 146˚C. The corresponding outside peak develops later and slightly more gradually. By the time the temperature is within 1˚C of the isothermal set point (t = 840 s), the $q_1$ peak has reached over ~ 80% of its maximum value. In contrast, the $q_2$ peak at this time has only ~ 10 % of the value it reaches at the end of the experiment. After certain time there is a change in the growth rate of the $q_2$ peak: It levels off but nevertheless it continues to increase slowly with time. This change in growth rate of the $q_2$ peak coincides with an abrupt transition in the $q_1$ peak to either a plateau or to a decline. It is interesting to note that the relative initial slope of peak $q_1$ and peak $q_2$ for a given condition, as well as the magnitude of final intensity, are consistent: If a given condition grows the peak at $q_1$ with a large initial slope and reaches a large intensity value, the corresponding peak at $q_2$ also will show a large initial growth rate and reach a similarly large intensity relative to other experiments.

In general, the time evolution of the amplitude of each SAXS meridional peak follows the same trends with shearing time for a given wall shear stress as those explained above for birefringence: The series of experiments at wall shear stress of 0.111 MPa show very large differences between shearing times of 0.3 s to 0.5 s, and 0.5 s to 0.75 s. Just 200-250 ms differences in $t_s$ at this highest shear stress kicked off the development of large amounts of highly oriented structures when cooling (Figure 5-5, right column). Consistent with the rheo-optical data, some saturation behavior is observed at the longer $t_s$. At the lowest stress utilized (0.073 MPa), the minimum shearing time that leads to significant crystallization within 3500 s is 2.0 s—considerably longer than that required at $\sigma_w \geq 0.092$ MPa. The window of $t_s$ prior to saturation at 0.073 MPa encompasses the entire range explored up to $t_s$ = 3.5 s, while for the three larger stresses, saturation was reached at $t_s$ = 2.0 s, 1.5 s, and 0.75 s.

### 5.3.2.2 Application of depth sectioning

Here we use the integrated intensity in the meridional region $I_{mer}$ (Figure 5-5, right column) comprising both oriented peaks to compare the effect of shearing conditions. To examine the effect of stress, it is necessary to apply depth sectioning (described in Chapter

III) to separate the contribution to the signal arising for each depth slice of the sample (i.e., for a specific range of shearing stresses) at a given shearing time. As explained in Chapter III, experiments at successively lower $\sigma_w$ capture structure development in the interior portion of their counterparts at greater $\sigma_w$ (Figure 3-2 of Chapter III). To correct for the optical path length through the corresponding portions of the sample, each $I_{mer}$ measurement is scaled by $\sigma_w$ (Figure 5-6). When viewed in this way, the difference between successive curves reveals the magnitude of the contribution arising from the stress interval that they bracket. For example, consider the case of $t_s = 0.75$ s (Figure 5-6, second graph), for which negligible $I_{mer}$ develops when $\sigma \leq 0.073$ MPa. The contribution due to the sample slice corresponding to stresses from 0.073 to 0.092 MPa is seen by inspection to be all of the rescaled signal observed for $\sigma_w = 0.092$ MPa. Similarly, the difference between the $t_s = 0.75$ s curves in Figure 5-6 at 0.099 MPa and 0.092 MPa corresponds to the contribution to the signal from the depth slice between $\sigma \in (0.092, 0.099 \text{ MPa})$. It is interesting to note that there are some curves that overlay almost exactly: For example, for a shearing time of $t_s = 2.0$ s (Figure 5-6, bottom graph) shows indistinguishable $I_{mer}/\sigma_w$ for three different shearing stresses. This indicates that the structure formed at very high stress (corresponding to the two outermost sections) is not contributing additionally to the meridional intensity in SAXS arising from the usual parent stacks. It is possible that this layer may have qualitatively different structure, but we cannot deduce from our data what that structure is. However, this is reminiscent of some TEM images obtained by Kumaraswamy et al. [7] in which at high shear stresses, the sample was so dense that the etching procedure used could not resolve the morphological features.

After obtaining the intensity contribution corresponding to each depth slice, we normalize it by the thickness of the depth section to obtain $\delta I_{mer}$ (Figure 5-7); in this way, the results from sections of different thicknesses can be compared, as described in Chapter III. The normalized intensity $\delta I_{mer}$ arising from each depth section for different $t_s$ provides insight into the structure development that occurs in a given slice (Figure 5-7). This allows distinguishing the shearing time necessary to kick-off highly oriented growth within a range of shear stress. For example, shearing between 0.3 s and 0.5 s induced highly oriented growth for the range 0.111 MPa – 0.099 MPa (Figure 5-7, top graph), although shearing for 0.3 s did not show any crystallization at all. Further shearing up to 0.75 s continued to enhance both the initial rate growth of oriented structures and their final quantity. For the second section between 0.099 MPa and 0.092 MPa (Figure 5-7, second graph), the transition between no growth and highly oriented growth occurs at longer shearing times, between 0.5 s and 0.75 s, after which it appears to saturate. When shearing was sustained for long times, subsequent oriented growth was not enhanced. This behavior was consistent over the range of stresses explored, but for decreasing imposed stress the times to reach saturation were also greater. It is noteworthy that for all the sections that reach saturation, the maximum amount of oriented intensity per unit volume reaches a similar value (~ 150 a.u. here).

We extracted the intensity growth rate for each section in Figure 5-7 near the point of inflection, when impingement had not yet occurred. In accord with the method outlined in the T-jump chapter, under these conditions the rate of growth of the signal due to the growth of kebabs on the oriented precursors in each depth section ($\delta I_{mer}$) will be proportional to the thread-length per volume present in that slice. Thus, the slopes calculated from the depth sections shown in Figure 5-7, as well as some additional slopes corresponding to depth sections obtained with finer stress increments (Figure 5-8) represent a measure of the thread-length per volume existing in the corresponding depth slice. We observe that, in the range of shearing times after kick-off and before saturation has occurred, the increase in thread-length per volume varies in an approximately linear fashion with shearing time. The relative increase of thread-length per volume with $t_s$ is greater for the sections subjected to higher shear stress.

## 5.4 Discussion

We compare our results to a state-of-the-art flow-induced model that captures the morphology created (that is, the development of the shish-kebabs) accounting for the dynamics of the melt. The best model available currently is that developed by Zuidema and co-workers in Eindhoven [5]. They use the earlier model of Janeschitz-Kriegl et al. [4]

as a starting point, because it provides an appropriate system of rate equations for flow-induced formation of point-like and thread-like precursors, and the growth which proceeds from them, leading to the morphologies that form. However, the Janeschitz-Kriegl model is written in terms of the shear rate imposed on the melt without including information on the relaxation time(s) of the polymer. Instead, the Eindhoven group argues that the formulation should account for the distortion of chain conformation (sensitive to the $i^{th}$ relaxation time) as the driving force for flow-induced crystallization.

In the Zuidema model, the general framework from the Janeschitz-Kriegl model is kept. First, flow induces the formation of point-like nuclei per unit volume, $N_f$, with a frequency that is proportional to a certain corresponding driving force, $R_1$. Then, these flow-induced point-like nuclei start immediately growing out into shish while flow is sustained. The velocity at which threads propagate from the available point-like nuclei is considered to be proportional to a certain driving force, $R_2$. Finally, the threads that have been created nucleate the growth of oriented kebabs, which propagate out from them with a linear growth velocity, G. Thus, the experimentally observed morphologies arise from the precursors created during flow. The basic equations that model the total thread-length per volume, $L_{tot}$ (common to both Janeschitz-Kriegl and Zuidema models) describe the evolution of microstructure in average cylindrical volumes:

$$\frac{d\psi_3}{dt} = 8\pi R_1 - \frac{\psi_3}{\tau_N} \qquad \text{Eq. [1]}$$

$$\frac{d\psi_2}{dt} = \psi_3 R_2 - \frac{\psi_2}{\tau_L} \qquad \text{Eq. [2]}$$

where $\psi_3 = 8\pi N_f$, $\psi_2 = 4\pi L_{tot}$, and $\tau_N$ and $\tau_L$ are the temperature-dependent decay times of the point-like nuclei and the thread-length, respectively.

The difference, then, between the models resides in the form of the driving forces $R_1$ and $R_2$. In the Janeschitz-Kriegl model, these driving forces were expressed in terms of the shear rate. It was acknowledged that the orientation of molecules played a role in flow-induced crystallization, but only one polymer melt (thus one distribution of molecular weights) was modeled: For a fixed material, a given shear rate indeed corresponds to a set level of molecular orientation. However, if their model were applied to a polymer melt with very different distribution of molecular weights, the same level of shear rate would not capture the differences in molecular orientation of the second polymer melt, since it depends strongly on the distribution. The Zuidema model is superior for general applicability to different materials since the driving force is expressed in terms of the recoverable compliance, which is closely related to the molecular configuration in the molten phase. Specifically, they use the second invariant of the deviatoric elastic Finger tensor, $J_2$. Furthermore, in a computational model it is possible to track the contribution of individual species to the macroscopic $J_2$. Interestingly, Zuidema et al. found that linking the rate constants $R_i$ to the $J_2$ of the highest relaxation time chains best captured experimental observations.

In the following, we examine our results in light of the Zuidema model for shearing times that are between kick-off of highly oriented growth and its saturation. Afterwards, we discuss those extreme behaviors, which suggest that some modifications to the model would be required to capture those effects as well.

### 5.4.1 Propagation of threads

An increase in the total thread-length per volume with sustained shearing flow is observed only in the interval between kick-off and saturation (Figure 5-7), that is, for $t_s \in (t_{kick\text{-}off}, t_{sat})$. Specifically, an approximately linear relation between the total thread length and $t_s - t_{kick\text{-}off}$ is obtained within this region (Figure 5-8). In the context of the Zuidema model, the decay term in Equation 2 can be considered negligible, since we chose 170°C as the shearing temperature because the decay of shish in this range is slow (in contrast to shearing at higher temperatures). If the last term of Equation 2 vanishes, the rate of growth of thread-length is proportional to the number of threads that are propagating multiplied by twice their propagation velocity $v_p$ (as each thread propagates from both ends):

$$\frac{d\psi_2}{dt} = \psi_3 R_2 \quad . \qquad \text{Eq. [3]}$$

Under steady state [8], $J_2$ has reached its steady value by $t_{kick\text{-}off}$, so it does not vary with shearing time. In the Eindhoven model, $R_2$ ($2\times v_p$ of the threads) was found to be proportional to the recoverable compliance that corresponds to the longest molecules; in other words, the driving force for propagating the threads $R_2$ was proportional to the contribution to $J_2$ of the slowest relaxing chains. This proportionality implies that for a given level of molecular orientation (that is, for a given level of shear stress applied), the velocity at which the threads are propagating is constant.

In light of these Eindhoven findings, we interpret the linear relationship experimentally observed between the thread-length per volume and the shearing time for a given level of shear stress (Figure 5-8). For a given level of shear stress (with constant velocity of propagation), the linearity with $t_s$ suggests that the number of threads that are propagating remains fairly constant ($\psi_3$ = constant) for $t_{kick\text{-}off} < t_s < t_{sat}$. If the number of threads increased significantly during this interval, then we would notice an increase in the slopes of thread-length vs. shearing time.

In summary, the consideration that the velocity of propagation is constant at steady state for a given level of molecular orientation of the longest chains, as proposed in the Zuidema model, captures well our experimental results for the interval of shearing times between kick-off and saturation. The dependence of the velocity of propagation $v_p$ on a measure of the orientation of the longest molecules in the melt at a given stress fits well with our schematic model of formation of threads in Chapter II, in which long chains had a preferential role in formation of the shish which was highly dependent on stress (the Janeschitz-Kriegl model would be unable to account for this).

In order to extract an absolute velocity of propagation from our real-time measurements, we would need to know $\psi_3$ (proportional to the number of threads). The values of $\psi_3$ that are propagating at different levels of stress may be different from one another; the slopes of our total thread-length per volume provide a measure of $\psi_3 \times 2 v_p$ for a given level of stress. Future TEM measurements that establish the number of shish per unit volume would be needed to deduce the velocity of propagation from the present experimental results.

### 5.4.2 Kick-off time

The observation of a delay in time between onset of shearing and strong proliferation of threads is not captured by the Zuidema model. There is small start-up behavior in the recoverable compliance before steady state is reached, but this is too small to account for the time of kick-off that we observe experimentally. We suggest that a modification in which not all point-like precursors instantaneously become sites from which threads elongate may be able to account for this effect. This is inspired by the findings and model explained in Chapter II of this thesis, where two separate stages in the formation of thread-like precursors were described: the kick-off stage from the point-like nuclei, and the propagation stage. It was also proposed that the stress requirement for kick-off of a shish from a point-like nucleus is more astringent than that of propagation; in other words, after a flow-induced point-like nucleus had been created, it was difficult to start the thread but once this happened, it was easier for that thread to propagate. Thus, this conceptual picture suggests that a rather small fraction of the flow-induced point-nuclei are actually able to kick off threads.

Thus, we propose the following modification to the equations employed in Zuidema model:

$$\frac{d\phi_3}{dt} = 8\pi R_1 - \frac{\phi_3}{\tau_N} \qquad \text{Eq. [4]}$$

$$\frac{d\psi_3}{dt} = k_3 \phi_3 \qquad \text{Eq. [5]}$$

$$\frac{d\psi_2}{dt} = \psi_3 R_2 - \frac{\psi_2}{\tau_L} \qquad \text{Eq. [6]}$$

Equation 4 is analogous to Equation 1: It describes the rate of appearance of flow-induced point-like nuclei per volume N ($\phi_3 = 8\pi N$). Equation 5 captures that only a fraction $N_f$ ($\psi_3 = 8\pi N_f$) of the formed point-like nuclei N at a given time will actually evolve into threads. A first-order type equation (with a rate constant $k_3$) already makes the total number of $N_f$ rise slowly with short shearing times and increasingly faster at longer times, starting to capture a "build-up" of the active point-like nuclei between two different shearing times. Then, it is the number of active point-like nuclei $N_f$ (through $\psi_3$) that is fed into Equation 6 (which is the same as Equation 2), providing the number of point-like nuclei from which threads evolve. In light of the findings of Chapter II, we anticipate that the rate constant $k_3$ is probably quite small, capturing the relative difficulty of the kick-off stage.

### 5.4.3 Saturation of thread propagation

The saturation in the thread-length per volume for the longest shearing times reminds us of similar saturation behavior inferred in Chapter III (when we applied the depth sectioning method for shear experiments performed at 137°C). In these temperature-jump experiments, we have created the threads at a temperature high enough that kebab growth was negligible; thus, interferences caused by the growth of kebabs during flow cannot be invoked to explain the behavior observed. Saturation in the number density of threads with shearing time has also been observed with TEM by Kumaraswamy et al. [9]. A plausible hypothesis is that, above certain high value of thread-length per volume, the probability that a propagating thread encounters another thread (thus stopping both their elongations) may become large enough that a further increase in the total thread-length per volume is prevented.

The Zuidema model captured certain leveling off of the number of threads with long shearing times, but it did so by utilizing a finite value of $\tau_L$ (the third term in Equation 2).

This decay term is related to the "melting away" of precursors which can only be significant at very high temperatures of shearing, and should not be considered as a viable source of saturation with shearing time at our temperatures, and much less at the temperature at which the experimental data fitted by model was obtained (150˚C, where lamellae are already significantly growing during shear). Thus, a modification with different underlying physics for saturation must be introduced to correctly capture saturation observed experimentally (perhaps a decay term related to the probability of collision between propagating threads at a given thread-length per volume).

### 5.4.4 Development of kebabs after cessation of flow

The highest temperature at which we can detect the emergence of the first peak at $q_1 \sim 0.125$ nm$^{-1}$ during cooling is ~ 146˚C. Previous SAXS measurements on this same material performed isothermally at 145˚C (data not shown here) exhibited the growth of a meridional peak at $q \sim 0.16$ nm$^{-1}$. Thus, the value of $q_1$ is smaller than we would expect at 146˚C, and furthermore, it continues to grow in intensity to within 141˚C. These observations suggest that as the polymer melt is being cooled, some lamellae start growing off at high temperatures with a given long spacing $L_1$. From the earliest time that birefringence growth is detected during cooling we infer that this growth started at $T \sim$ 162˚C. As temperature continues to decrease, these lamellae continue to grow: They may do so with decreasing thickness due to the lower temperature, but still maintaining their characteristic spacing $L_1$.

These early lamellae are expected to have larger thickness near the shish, so the actual space between nucleated kebabs on the thread may be quite small. This may keep other lamellae from growing off those "free" interspacings on the shish: The thickness of lamellae that can grow at relatively high temperatures may be larger than the available interspacing. As the early lamellae continue to grow with larger gaps between them, and temperatures close to 140˚C are reached, some interspacings between the lamellae with long period $L_1$ may be filled with thinner lamellae which cause the appearance of a smaller periodicity $L_2$ (thus larger q). This may partially decrease the intensity at $q_1$ if it happens profusely; however, the sharp change of growth rate in the intentisity of $q_1$ suggests that it may mainly arise from impingement between the $L_1$ lamellae growing from neighboring threads, and not from a gradual filling in. There may be a significant quantity of interspacings near the thread that are still too small, so that the period there remains as $L_1$.

The initial long spacing $L_1$ on the shish may be related to the amount of sites along the shish that start nucleation at a relatively high temperature. In studies of shish-kebab structures in solution, Keller and coworkers [10] found that crystallization performed at very high temperatures (over extended periods of time) gave rise to large interspacings between the kebabs, while growth at lower temperatures increased greatly the density of nucleation of kebabs. In AFM experiments on shish grown in thin films, Hobbs et al. also observed that not all of the backbone nucleated lamellae [11]. Under cooling conditions, Hobbs reported that sometimes some sites on the shish only became active at lower temperatures than others. However, lack of nucleation of kebabs from the shish was observed in many sites; one of the plausible explanations suggested was that the inactive site in the shish was actually too small (due to adjacent kebabs) to accommodate a new lamella.

## 5.5 Conclusion

This study lays the groundwork to quantitatively follow the characteristic kick-off, propagation, and saturation of the threads during flow. The data obtained here for a single material and shearing temperature suggests some modifications that the state-of-the-art model for flow-induced crystallization should include to correctly capture kick-off and saturation of the formation of threads. For intermediate shearing times, our results are well described by the model and lay the groundwork for performing measurements to determine the velocity of propagation of threads at different shearing stresses. By extending these measurements to other model materials (for instance, bimodal blends with different concentrations of long chains from the one used here), a larger parameter space can be surveyed; this will provide additional feedback and experimental data to test predictive models that connect molecular characteristics of a resin to structure formation under processing conditions.  It is important to note that, in order to extract relevant kinetic parameters from experiments to be tested in a model, a series of thoughtfully selected conditions must be performed.

## 5.6 Figures

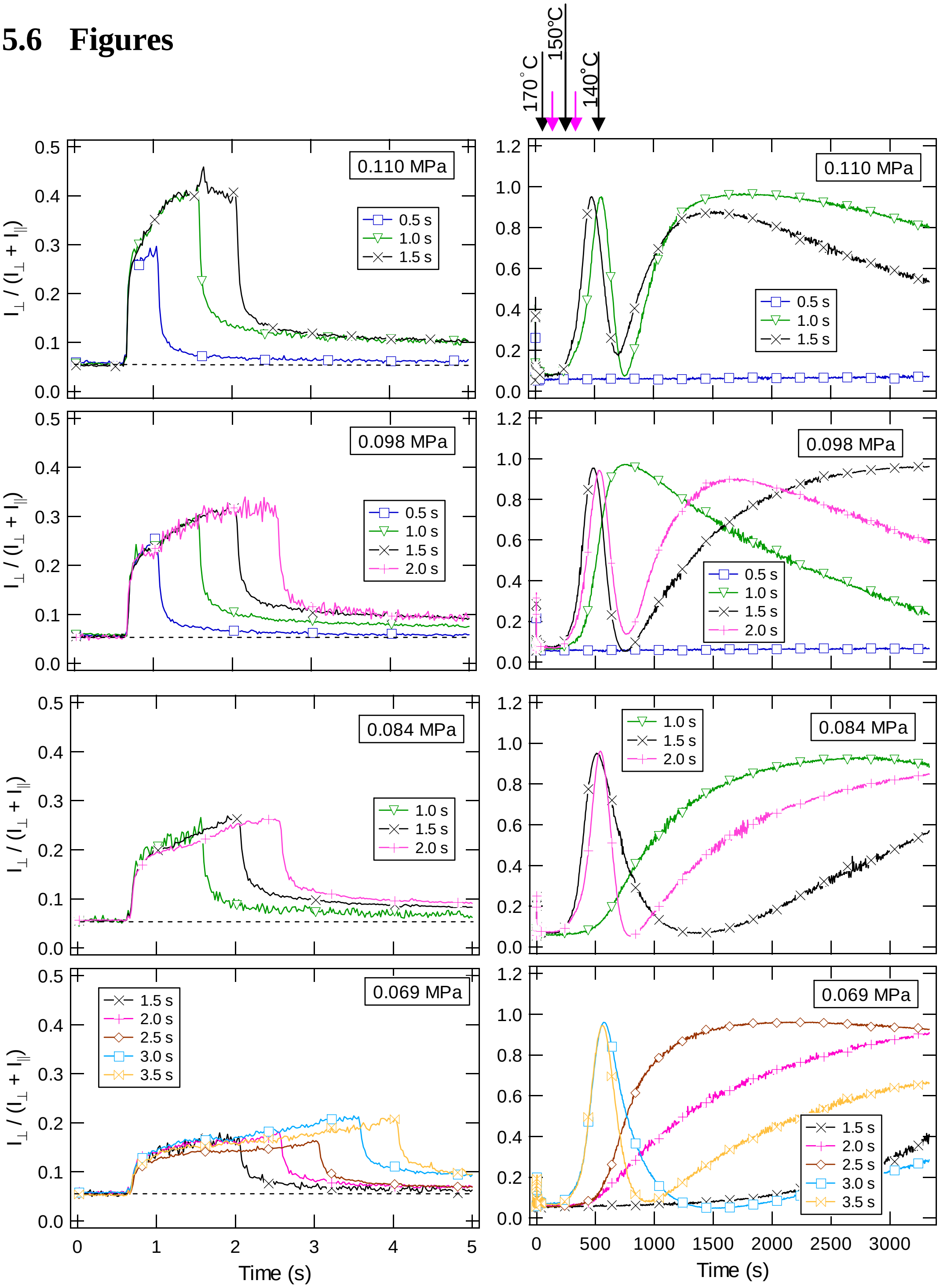

**Figure 5-1. Real-time birefringence measurements. The left row zooms in on the data acquired during and right after the shear pulse. Temperatures are indicated on top with arrows (intermediate arrows with no labeling correspond to 160˚C and 145˚C).**

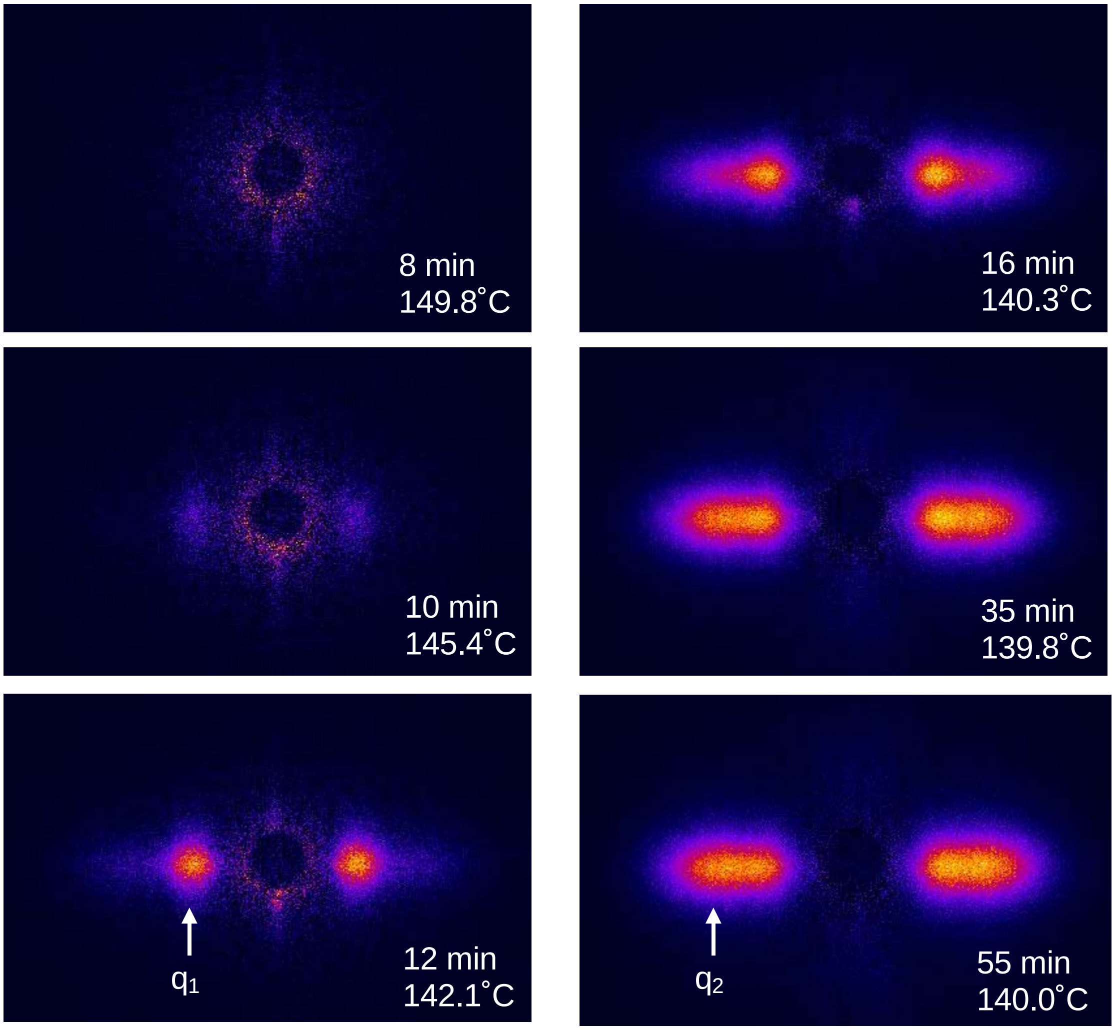

**Figure 5-2. Typical SAXS pattern development during an experiment ($\sigma_w$ = 0.092 MPa and $t_s$ = 2.5 s) where highly oriented crystallization was induced. In the meridional region, first a peak appears at low scattering angle ($q_1$) and at later times a second peak at higher scattering angle ($q_2$) grows. The direction of flow is horizontal.**

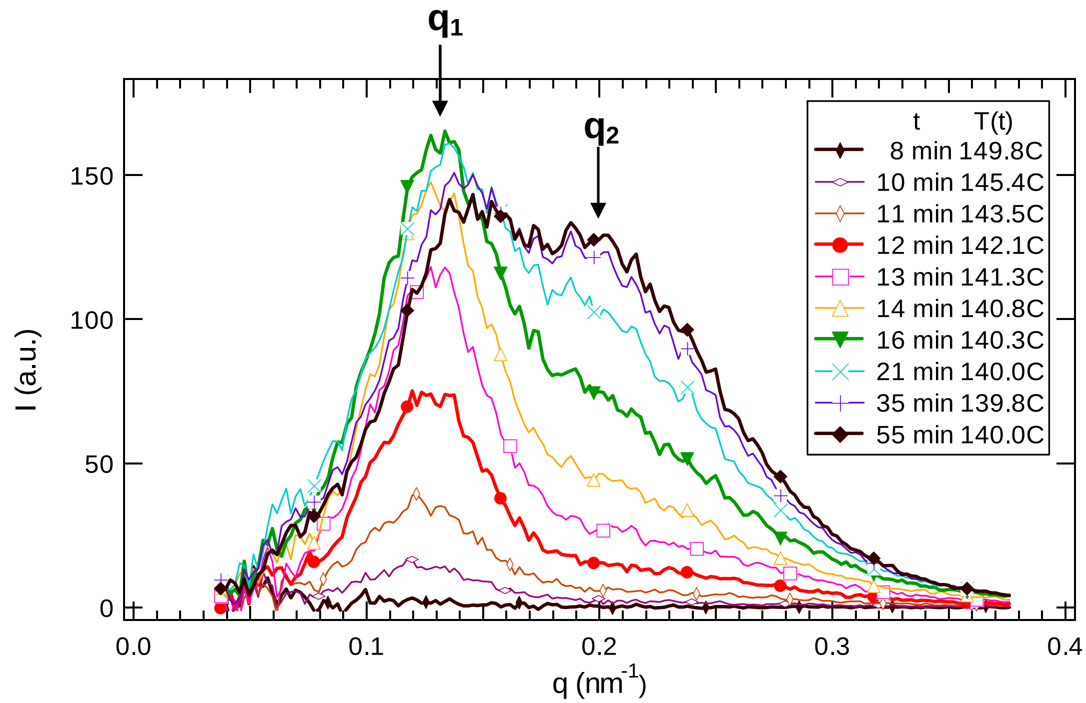

**Figure 5-3.** **Progression of SAXS meridional scattering vs. wavevector for the experiment illustrated in Figure 5-2 ($\sigma_w$ = 0.092 MPa for $t_s$ = 2.5 s)**

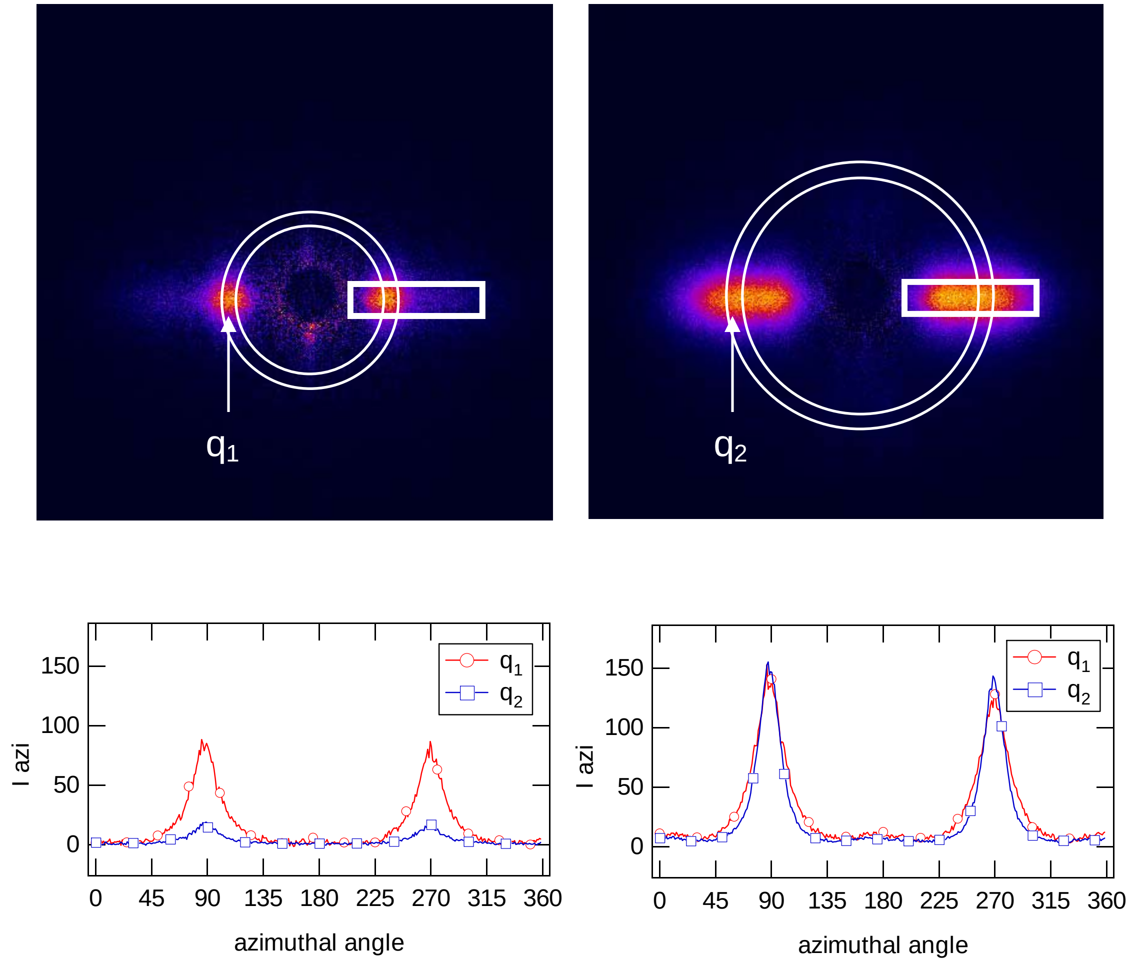

Figure 5-4. Top: Example SAXS patterns at early (left) and later (right) times indicating the range of q over which intensity was averaged (concentric circles) at each azimuthal direction to characterize the azimuthal profile at each peak ($q_1$ and $q_2$), and showing the rectangle area in which intensity was integrated to characterize the overall meridional intensity, $I_{mer}$. Bottom: corresponding azimuthal scans of intensity corresponding to the patterns above

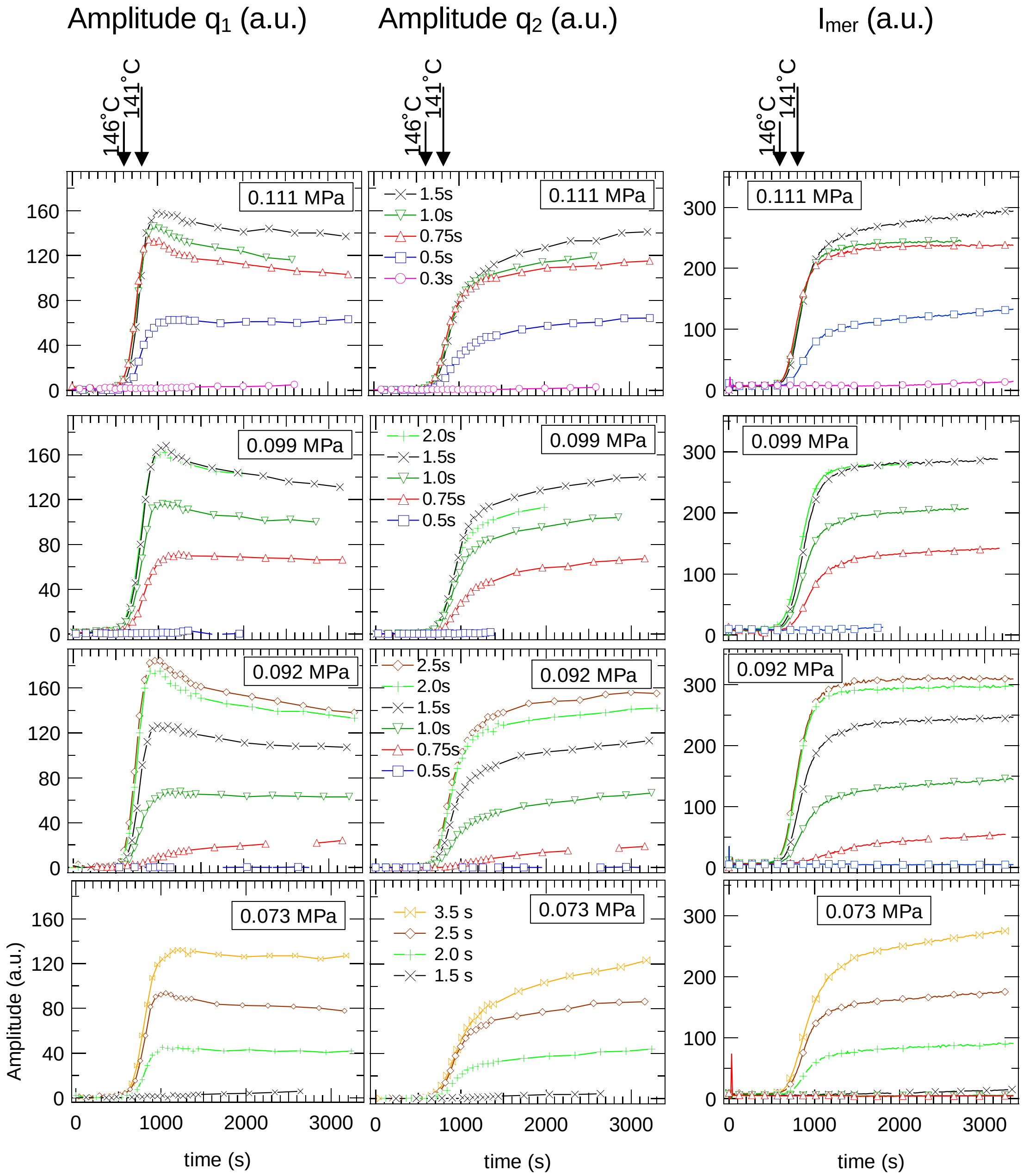

**Figure 5-5.** Real-time amplitude of inner peak at $q_1$ (left column) and of outside peak at $q_2$ (middle column) obtained from fits of their respective azimuthal scans. Right column corresponds to the meridional integrated intensity ($I_{mer}$) for each wall shearing stress used ($\sigma_w$) at different shearing times.

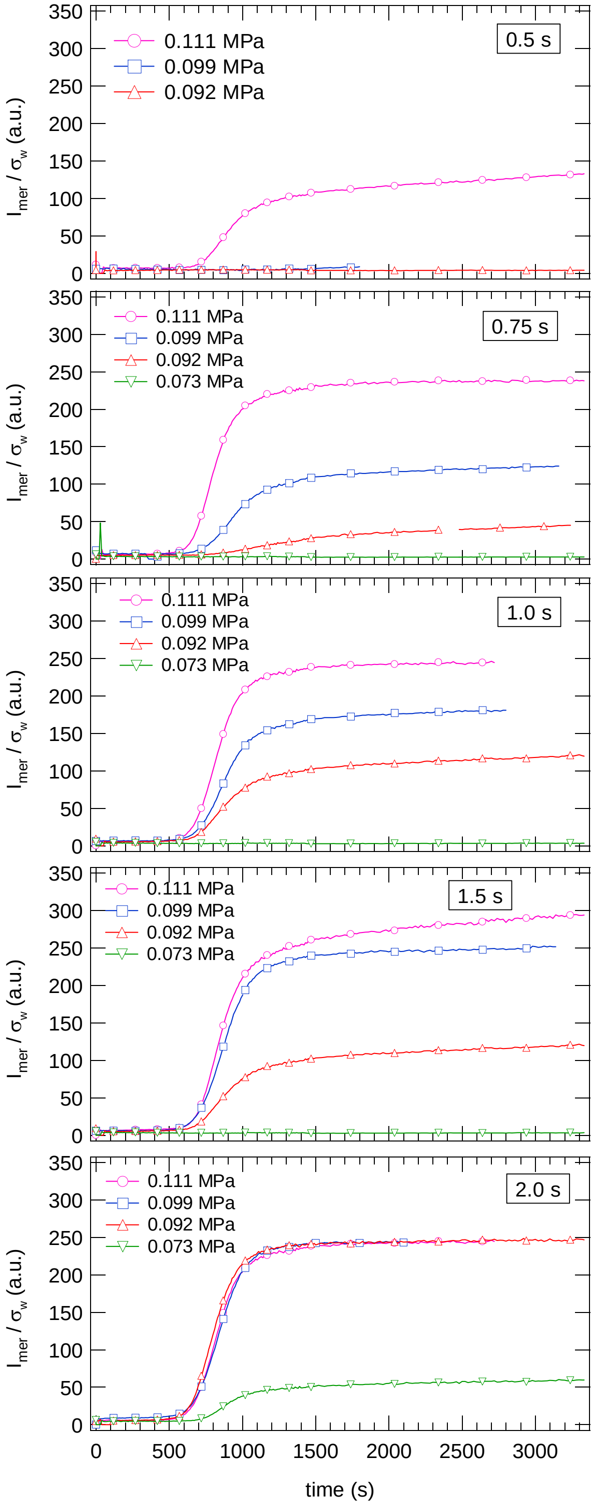

**Figure 5-6. Integrated meridional intensity rescaled by the wall shear stress (using 0.111 MPa as the reference), in preparation for depth sectioning. Each graph corresponds to a specific shearing time.**

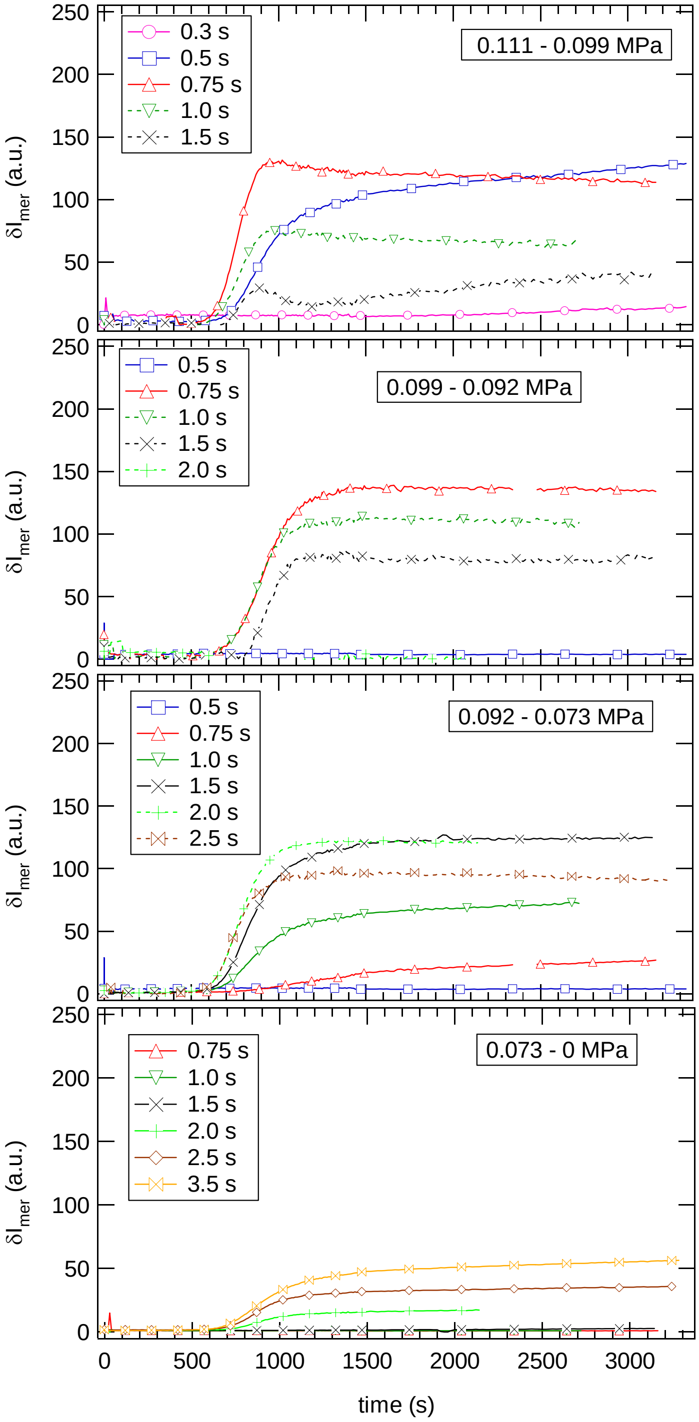

**Figure 5-7.** **Contribution to $I_{mer}$ arising from each depth slice. Each intensity has already been normalized by the thickness of the slice.**

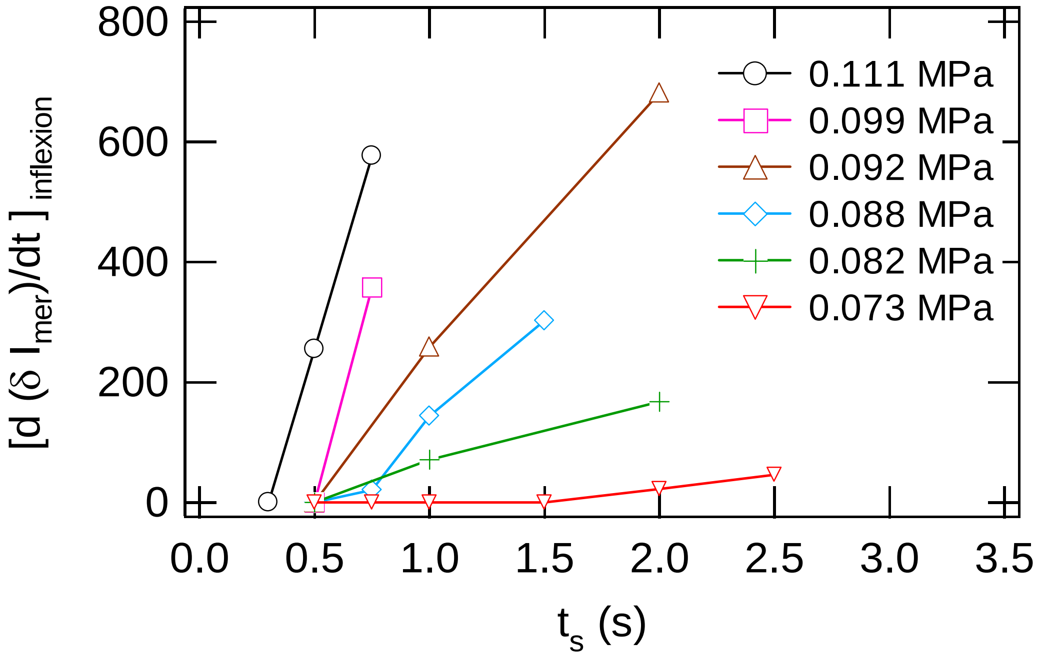

**Figure 5-8.** **Initial growth rate near the inflexion point of $\delta I_{mer}$ (Figure 5-7) for depth sections at different characteristic shear stresses. Only sections for shearing times before saturation was reached have been used. Additional measurements from sections corresponding to thinner stress increments are also presented.**

## 5.7 References

1. Isayev, A.I., and C.A. Hieber. *Toward a Viscoelastic Modeling of the Injection-Molding of Polymers.* Rheologica Acta, 1980. **19**(2): 168-182.
2. Guo, X., A.I. Isayev, and L. Guo. *Crystallinity and microstructure in injection moldings of isotactic polypropylenes. Part 1: A new approach to modeling and model parameters.* Polymer Engineering and Science, 1999. **39**(10): 2096-2114.
3. Doufas, A.K., I.S. Dairanieh, and A.J. McHugh. *A continuum model for flow-induced crystallization of polymer melts.* Journal of Rheology, 1999. **43**(1): 85-109.
4. Liedauer, S., G. Eder, H. Janeschitz-Kriegl, et al. *On the Kinetics of Shear-Induced Crystallization in Polypropylene.* International Polymer Processing, 1993. **8**(3): 236-244.
5. Zuidema, H., G.W.M. Peters, and H.E.H. Meijer. *Development and validation of a recoverable strain-based model for flow-induced crystallization of polymers.* Macromolecular Theory and Simulations, 2001. **10**(5): 447-460.
6. Kumaraswamy, G., R.K. Verma, and J.A. Kornfield. *Novel flow apparatus for investigating shear-enhanced crystallization and structure development in semicrystalline polymers.* Review of Scientific Instruments, 1999. **70**(4): 2097-2104.
7. Kumaraswamy, G., R.K. Verma, A.M. Issaian, et al. *Shear-enhanced crystallization in isotactic polypropylene Part 2. Analysis of the formation of the oriented "skin".* Polymer, 2000. **41**(25): 8931-8940.

8. Janeschitz-Kriegl, H., *Polymer Melt Rheology and Flow Birefringence*. Polymers: Properties and Applications. Vol. 6. 1983, New York: Springer-Verlag. 524.

9. Kornfield, J.A., G. Kumaraswamy, and A.M. Issaian. *Recent advances in understanding flow effects on polymer crystallization.* Industrial & Engineering Chemistry Research, 2002. **41**(25): 6383-6392.

10. Hill, M.J., P.J. Barham, and A. Keller. *On the Hairdressing of Shish-Kebabs.* Colloid and Polymer Science, 1980. **258**(9): 1023-1037.

11. Hobbs, J.K., A.D.L. Humphris, and M.J. Miles. *In-situ atomic force microscopy of polyethylene crystallization. 1. Crystallization from an oriented backbone.* Macromolecules, 2001. **34**(16): 5508-5519.